Title
Imbibition in Paper-Based Microfluidic Devices

Author
Castro, Carlos

Publication Date
2016

UNIVERSITY OF CALIFORNIA
RIVERSIDE

Imbibition in Paper-Based Microfluidic Devices

A Dissertation submitted in partial satisfaction
of the requirements for the degree of

Doctor of Philosophy

in

Mechanical Engineering

by

Carlos Castro

March 2017

Dissertation Committee:
- Dr. Hideaki Tsutsui, Chairperson
- Dr. Guillermo Aguilar
- Dr. Kambiz Vafai

The Dissertation of Carlos Castro is approved:

Committee Chairperson

University of California, Riverside

ACKNOWLEDGMENTS

First and foremost, I would like to acknowledge my advisor, Dr. Hideaki Tsutsui for his support, mentorship, and teaching throughout my graduate career. Thank you for the encouragement and patience during the numerous failures and successes experienced during my graduate school tenure.

I would like to thank my committee members Dr. Guillermo Aguilar and Dr. Kambiz Vafai for their time. I greatly appreciate their support, comments, and suggestions.

I would like to thank all my lab mates I worked with alongside in the Regenerative Microengineering Laboratory. I would like to especially thank Daniel Nampe, Brent Kalish, Jessica Wen, Chad Baudette, Ronak Joshi, Joshua Karam, and Cindy Rosillo for the enjoyable interactions and friendship developed over the years. Special thanks to my undergraduate student Cindy Rosillo for her hard work and persistence. Special thanks to Brent Kalish for his assistance with SEM images.

I would like to thank the following sources for their financial support during my tenure at UCR; Alliance for Graduate Education and the Professoriate Fellow, The Bourns College of Engineering Dean's Distinguished Fellowship Award, Lung-Wen Tsai Memorial Award for Mechanical Design, Cardenas Markets Scholarship, Graduate Research Mentorship Fellowships, California Space Grant Consortium (CaSGC) Fellowship, and the National Science Foundation under Grant No. CBET-1606181.

Finally, I would like to thank my family and friends for their love and support throughout my graduate school career. My parents for their sacrifices, hard work, and love. My mom, Joaquina for her love and support thought out my life, showing me the value of education, and finally her home cooked meals and use of her laundry machines. My brothers, Jose and Javier for being great brothers and just being there. Lastly, my nephew and future niece for their past, present, and future shenanigans.

DEDICATION

To my dogs, Guero (Rest in Peace 2016) and Canon.

ABSTRACT OF THE DISSERTATION

Imbibition in Paper-Based Microfluidic Devices

by

Carlos Castro

Doctor of Philosophy, Graduate Program in Mechanical Engineering
University of California, Riverside, December 2016
Dr. Hideaki Tsutsui, Chairperson

Point-of-care technologies provide innovative solutions that improve treatment. Healthcare systems including some low-resource settings have begun implementing these technologies providing the convenience and reduction of large laboratory set-ups. Low-cost is one of the main driving components when it comes to point-of-care diagnostics. Paper-based microfluidics has generated a great amount of interest for the development of low-cost diagnostic and self-contained analytical devices. Satisfying the World Health Organization's (WHO) recommended ASSURED criteria; Affordable, Sensitive, Specific, User-friendly, Rapid and robust, Equipment free, Deliverable, paper-based microfluidics have made point-of-care testing more accessible. Applications range from healthcare, food safety, and environmental monitoring, among others. What has in part attracted attention is the low-cost, ease-of-use, and adaptability of these paper devices. Compared to conventional microfluidic devices, the paper-based counterparts are able to

utilize paper's inherent wicking property to eliminate the external pumping needed to drive the fluid. Channels are easily formed by either selectively removing sections of the paper substrate or by pattering channel boundaries with a hydrophobic material.

In spite of the benefits and advantages described above, paper-based microfluidic technologies often lack the necessary sensitivity and sophistication available in conventional microfluidic devices. In order to be a competitive alternative, paper-based microfluidics require improvement and novel development of feasible detection methods. These methods will likely require increasingly complex chemistry and control of reagents. Thus, understanding imbibition as well as obtaining precise, accurate, and consistent fluid handling within the paper device will be crucial.

Although considerable knowledge exists on techniques to manipulate fluid within the paper channel, what is lacking are studies on how non-laboratory conditions (e.g. relative humidity) influence fluid flow. This presentation aims to address this gap with particular focus on the effects of relative humidity and channel width. A series of controlled imbibition experiments is reported using cellulose papers commonly used in the field of paper-based microfluidics. We show that both the imposed relative humidity and the channel width have critical design considerations in paper-based devices. Additionally, we compare three models, the Lucas-Washburn model, the Fries et al. (2008) model which incorporates evaporation, and a newly developed water saturation model that incorporates evaporation as well as residual water in the paper. We assess their accuracy in representing the experimental data and systematically evaluate the importance of evaporation and water saturation under a wide range of relative humidity

conditions. The current study has created a library of paper-specific, imbibition-related properties for commonly used filter and chromatography papers for the first time.

Lastly, the effort of fluid manipulation is continued. A qualitative investigation on two-dimensional wax-bound channels is covered. The channels encompass the most basic geometry that may be present in complex fluidic designs; sudden expansion, contraction, and a box along the channel. It is found that these simple channel cross-sections can accelerate and decelerate fluid flow, therefore altering the time of fluid delivery.

Collectively, the success of this research will improve the development of future diagnostic and analytical paper devices producing a user-friendly and cost effective point-of-care alternative.

TABLE OF CONTENTS

LIST OF FIGURES

LIST OF TABLES

LIST OF SYMBOLS

Symbol	**Description and unit**
a	Suction term coefficient, m^2/s
b	Evaporation term coefficient, $1/s$
c	Gravity term coefficient, m/s
d	Fiber diameter, m
d_T	Fractal dimension
C, C_1, C_2	Geometric factors
D	Pore diameter, m
D_e	Effective pore diameter, m
D_h	Hydraulic diameter, m
$D(\Theta)$	Water diffusivity as a function of saturation, m^2/s
F	Evaporation flux, $kg/m^2\text{-}s$
g	Gravitational acceleration, m/s^2
h	Height of meniscus, m
k	Permeability, m^2
K	Effective permeability, m^2
$\tilde{K}(\theta)$	Hydraulic conductivity as a function of water content, m/s
L_f	Actual length traveled, m
L_s	Straight-line length, m
$\dot{M}$	Mass flow rate, kg/s
m_{rw}	Residual mass of water, kg
p	Pressure, Pa
p_c	Capillary pressure, Pa
p_s	Suction pressure, Pa
p_{atm}	Atmospheric pressure, Pa
RH	Relative humidity
S_w	Water saturation
T	Thickness of paper, m
v	Imbibition speed, m/s
v_c	Interstitial velocity, m/s
V_T	Total volume, m^3
W	Width of channel, m
W_B	Basis weight, g/m^2
y_f	Imbibition front distance, m

Greek Symbol	Description and unit
β	Fitting constant, *m/s*
γ	Surface tension, *N/m*
ε	Scale of observation
θ	Contact angle, ° , water content
Θ	Saturation
μ	Dynamic viscosity, *Pa-s*
ρ	Liquid density, kg/m^3
ρ_c	Density of cellulose, kg/m^3
τ	Tortuosity
ϕ	Porosity
ϕ_c	Critical porosity
ψ	General function

1. PAPER-BASED MICROFLUIDICS: AN OVERVIEW

1.1. Introduction

Point-of-care technologies provide innovative solutions that improve treatment. Healthcare systems including ones in low-resource settings have begun implementing these technologies providing the convenience and reduction of large laboratory set-ups. Low-cost is one of the main parameters that drive the development of point-of-care diagnostics.

Paper-based microfluidics has become an emerging field that strives for low-cost, simple-to-use analytical and diagnostics devices. What has attracted many researchers into this emerging field is the low capital costs required for device fabrication. Fabrication of conventional microfluidic devices made of silicon, glass or polydimethylsiloxane (PDMS) requires bulk or surface micromachining, or replica molding with a micromachined master mold, all of which involve cleanroom equipment and facilities. On the other hand, paper-based microfluidics only requires paper and a tool that can define impermeable channel boundaries, significantly reducing the resources needed for newcomers to enter the field of microfluidics. Utilizing paper and paper-like materials as the main substrate, paper-based microfluidics devices utilize the inherent wicking property to drive the fluid. This serves a tremendous benefit over conventional microfluidics which require external machinery to drive the fluid. In this chapter, a brief overview of paper-based microfluidics is given with emphasis on fabrication, detection techniques, and device functionality and capabilities.

1.2. Fabrication Methods

Fabrication methods have largely been developed and adapted from other platforms. Channels are formed by either selectively removing sections of the paper substrate or by pattering the channel design with a hydrophobic material. The former ranges from high precision CO_2 laser-cutting to craft cutting. The latter methods range from those of traditional photolithography to techniques using commercially available printers including inkjet and solid ink. Ultimately, what all these fabrication methods have in common is the creation of defined impermeable boundaries for fluid transport. There exist a large amount of fabrication methods, and, a few are detailed here. See Fig. 1.1 for a schematic overview (Cate et al. 2015).

1.2.1. Wax pattering

Obtaining hydrophobic barriers in the paper is a simple and quick method to control and direct fluid flow. Wax printing utilizes a commercially available printer with wax-based ink (Carrilho et al. 2009; Lu et al. 2009). In this method the paper is fed into the printer, after printing the wax patterned paper is heated in a hot plate or oven for a short time, usually a couple seconds to a few minutes. Wax screen printing uses a solid wax with a screen to apply the wax onto the paper and later heated, allowing the wax to penetrate onto the paper (Dungchai et al. 2011). Alternatively, wax dipping uses a mold which acts as a mask where the pattern is transferred onto the paper by dipping into melted wax (Songjaroen et al. 2011). Although these wax patterning methods are low-cost and require inexpensive instrumentation, the key disadvantage is the inconsistency and low-resolution of the final patterned design.

1.2.2. Printing methods

Inkjet printing allows for both selective hydrophobization and dehydrophobization of the patterned channels. The former uses a sizing agent such as alkyl ketene dimer (AKD) (Li et al. 2010; Li et al. 2008). AKD is printed onto the paper followed by a curing step and finally a wash by a solvent. The latter methods uses a solvent such as toluene to remove the hydrophobic polystyrene that was applied to the paper (Abe et al. 2008). This results in hydrophilic channels.

Flexographic printing allows for fast and high-throughput production of paper devices. Flexible plates are used to deposit the hydrophobic polystyrene solution onto the paper (Olkkonen et al. 2010). The key limitation are the high cost, availability of such printers, and the requirement of individualized plates for each pattern.

1.2.3. Lithography

The influential work of Martinez et al. (2007) first used photolithography to develop the multi-analyte test on patterned paper. This photolithography technique uses a photoresist curable by a UV light exposed through a mask. The uncured photoresist is washed by a solvent, leaving the cured hydrophobic barriers. Martinez et al. (2008c) further improved this method for low-resource settings by using a combination of sunlight and a hot plate to cure the device.

1.2.4. Cutting Methods

Paper cutting fabrication removes material to create the desired design. Computer controlled plotters (Fenton et al. 2009) are quick and relatively inexpensive. Unfortunately, these can lead to tearing and warping of the paper, therefore, require precise optimization. The most popular cutting method is CO_2 laser cutting (Evans et al. 2014; Nie et al. 2013). This method is extremely precise, quick, and highly adaptable. Unfortunately laser cutters may require high initial cost. The advantages of paper cutting are the high precision and the lack of chemical treatments needed. Unfortunately, cut devices are fragile and suffer from a lack of mechanical rigidity. This results in the requirement of an additional rigid support or packaging.

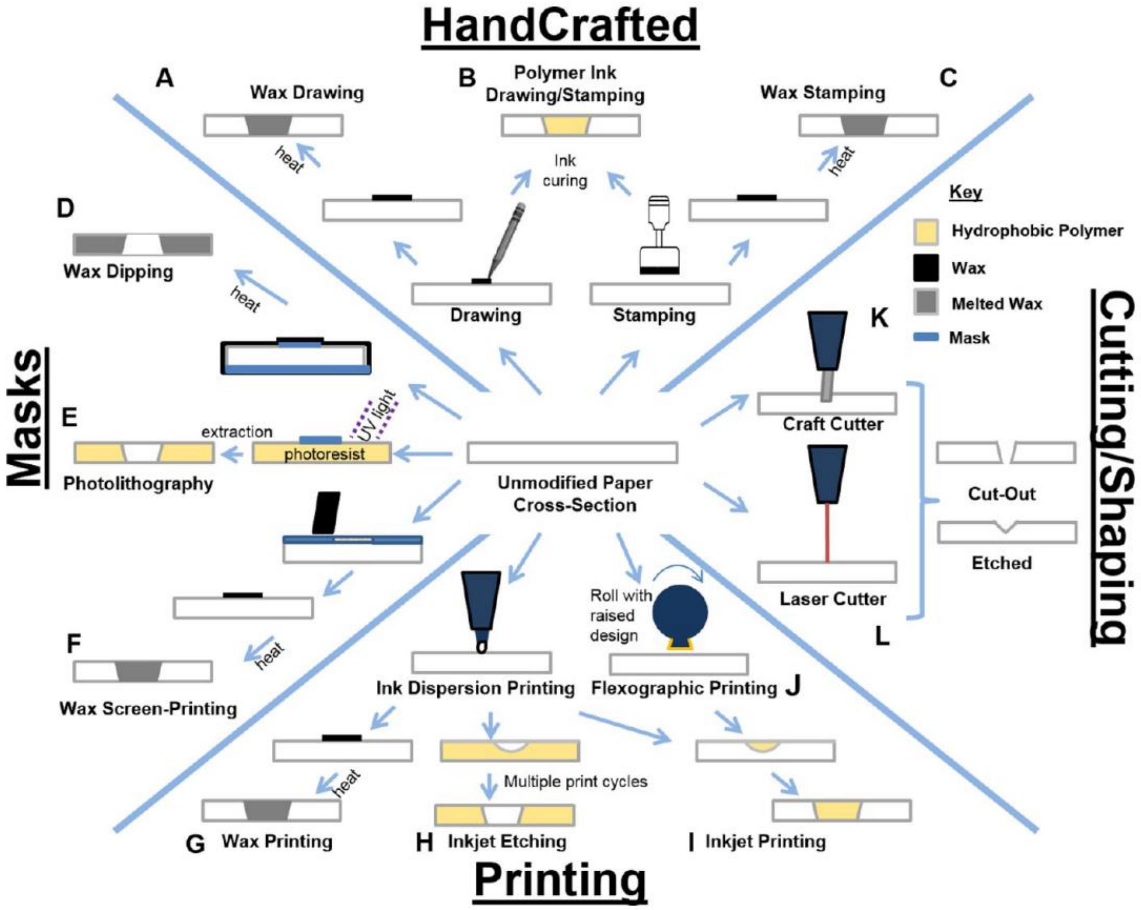

Fig. 1.1 Schematic overview of paper-based microfluidic fabrication methods. (Cate et al. 2015).

1.3. Detection techniques

Detection techniques for paper-based microfluidics are generally adapted from established chemical and biological sensors in different platforms. The aim of detection techniques in paper-based microfluidics is to replicate or to develop alternatives to the established analytical devices. The most common technique for detection is that of colorimetry (i.e. change of a visual signal which can be correlated to an analyte concentration). More sensitive and quantitative techniques such as electrochemical sensing and different forms of light emitting sensing have also been adapted and implemented. See Fig. 1.2 for selected detection techniques.

1.3.1. Colorimetry

Colorimetry is the most common technique used primarily because of the ease-of-use both in operation and in signal readout. The simplest signal readout is through merely indicating the presence of the analyte, such as those of glucose detection and pregnancy test strips (Abe et al. 2008; Martinez et al. 2007). Semi-quantitative techniques have also been developed. These require the use of a calibration chart, with intensity indicating the concentration strength. Similarly, applications range from simple enzymatic detection, to pH readout, and to protein presence (Abe et al. 2008; Martinez et al. 2007). These semi-quantitative readouts can become more objective by recording the intensity through a scanner or camera (Hossain et al. 2009; Khan et al. 2010) or through smartphones (Lopez-Ruiz et al. 2014; Martinez et al. 2008a; Shen et al. 2012).

1.3.2. Electrochemical sensing

Electrochemical sensing’s key advantage over colorimetric assays is the improvement in limit of detection. The target analyte concentration have been measured as low as a few nM (Yetisen et al. 2013). Initially demonstrated by Dungchai et al. (2009), electrochemical sensing has gained traction from the healthcare field to measure glucose (Noiphung et al. 2013; Santhiago and Kubota 2013), cancer biomarkers (Su et al. 2014), as well as for monitoring drinking water for heavy metals (Dungchai et al. 2009; Nie et al. 2010).

1.3.3. Light emitting sensing

Light emitting sensing includes electrochemiluminescence, chemiluminescence, and fluorescence. Its sensitivity is within the same levels of that of electrochemical detection but it often requires smaller reagent volumes, with the main disadvantage being that readouts must be taken in a dark environment. Applications range widely, from cancer biomarkers (Wang et al. 2012), to DNA sensing (Ali et al. 2009), to heavy metal motoring, and to explosive residue detection (Taudte et al. 2013), among others.

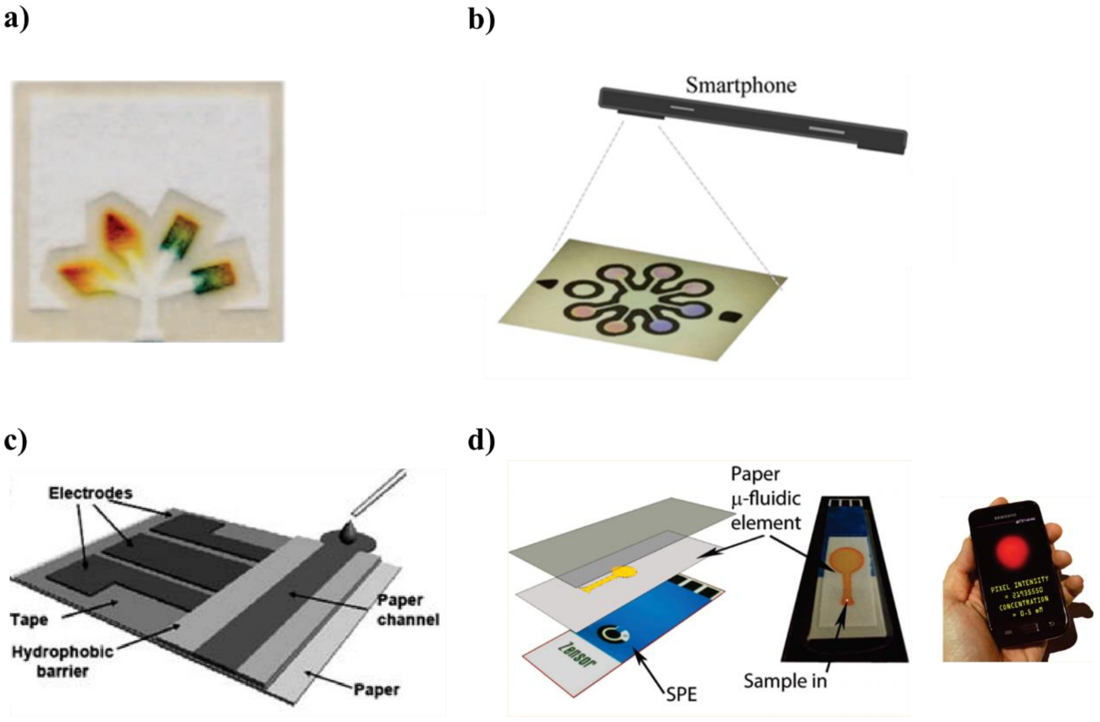

Fig. 1.2 Selected detection techniques. a) Colorimetric detection (Martinez et al. 2008c). b) Colorimetry with smartphone integration (Lopez-Ruiz et al. 2014). c) Electrochemical detection (Nie et al. 2010). d) Electrochemiluminescence with smartphone integration (Delaney et al. 2011).

1.4. Functionalities and capabilities

The numerous applications associated with paper-based microifluidics devices require the manipulation and control of the fluid. This applies to simple one-dimensional (1D) strips to three-dimensional (3D) devices capable of multiplexing and sophisticated sample processing. The ability to have a controlled stop of the fluid and redirect such fluid is key to the sophistication in detection techniques. Depending on the functionality desired, certain methods have been developed to deliver and control the fluid flow. Timed delivery of the fluid is arguably the most important aspect of designing paper-based microfluidics devices because it allows for sequential delivery of the reagents involved. Numerous detection techniques require specific incubation time, mixing, and washing steps. This fluid manipulation is expected to become increasingly important as the chemistry adopted to paper-based microfluidics becomes more sophisticated. See Fig. 1.3 for a selected functionalities and capabilities.

1.4.1. Varying geometric cross-section

Delaying the fluid is the most common method to control sequential delivery (Fu et al. 2010; Fu et al. 2012; Kauffman et al. 2010; Osborn et al. 2010). At its simplest form this is done by varying the length and/or the cross-section of the channel. Fenton et al. (2009) demonstrated two-dimensional (2D) geometry changes to delay flow by fabricating the device using a computer controlled plotter. This allowed multiple assays on the same device creating multiplex capabilities. Fu et al. (2010) demonstrated chemical amplification with washing steps though sequential delivery in 2D. Chemical amplification was demonstrated with washing steps. Fridley et al. (2014) demonstrated a similar device with high sensitivity. Lutz et al. (2011), using pre-defined fluid reservoir demonstrated a novel 2D sequential delivery method by varying the length of the channel. This created automated shut-off vales allowing for termination of the reaction.

1.4.2. Switches and valves

Another method in controlling fluid flow is by delaying the fluid through physical means, such as to some extent, stopping the flow by a specified time. This has been accomplished by sugar delays (Houghtaling et al. 2013; Lutz et al. 2013). Valve actuators and switches have been implemented, ranging from simple push down switches made of paper (Noh and Phillips 2010) to more complicated 3D devices created by a highly swelling material (Toley et al. 2013; Toley et al. 2015). Magnetic cantilevers acting as valves have been implemented (Li et al. 2013). Functional fluid circuits have been created using fluidic diodes that prevent or allow fluid flow in to a specific direction (Chen et al. 2012). Sequential delivery was shown to be possible by this method.

1.4.3. 3D architecture

Three-dimensional (3D) devices have gain increasing popularity due to the potential in reducing device footprint. The 3D architecture allows for both lateral and vertical fluid flow creating efficient multiplexing. First developed by Martinez et al. (2008b) the device was fabricated by multi-layering paper using double –sided tape with cellulose powder sandwiched for interlayer contact. This 3D method was further expanded by Noh and Phillips (2010) to created fluidics timers. Thom et al. (2012) used multi-stacked paper to create a fluidic battery.

Taking the 3D architecture further, origami-based devices have been proposed. This folding fabrication technique allows for the device to be patterned onto a single sheet of paper (Liu and Crooks 2011). Alternatively, to just folding, using adhesive spray, multiple groups have created more robust and sophisticated 3D devices (Kalish and Tsutsui 2014; Kalish and Tsutsui 2016; Lewis et al. 2012).

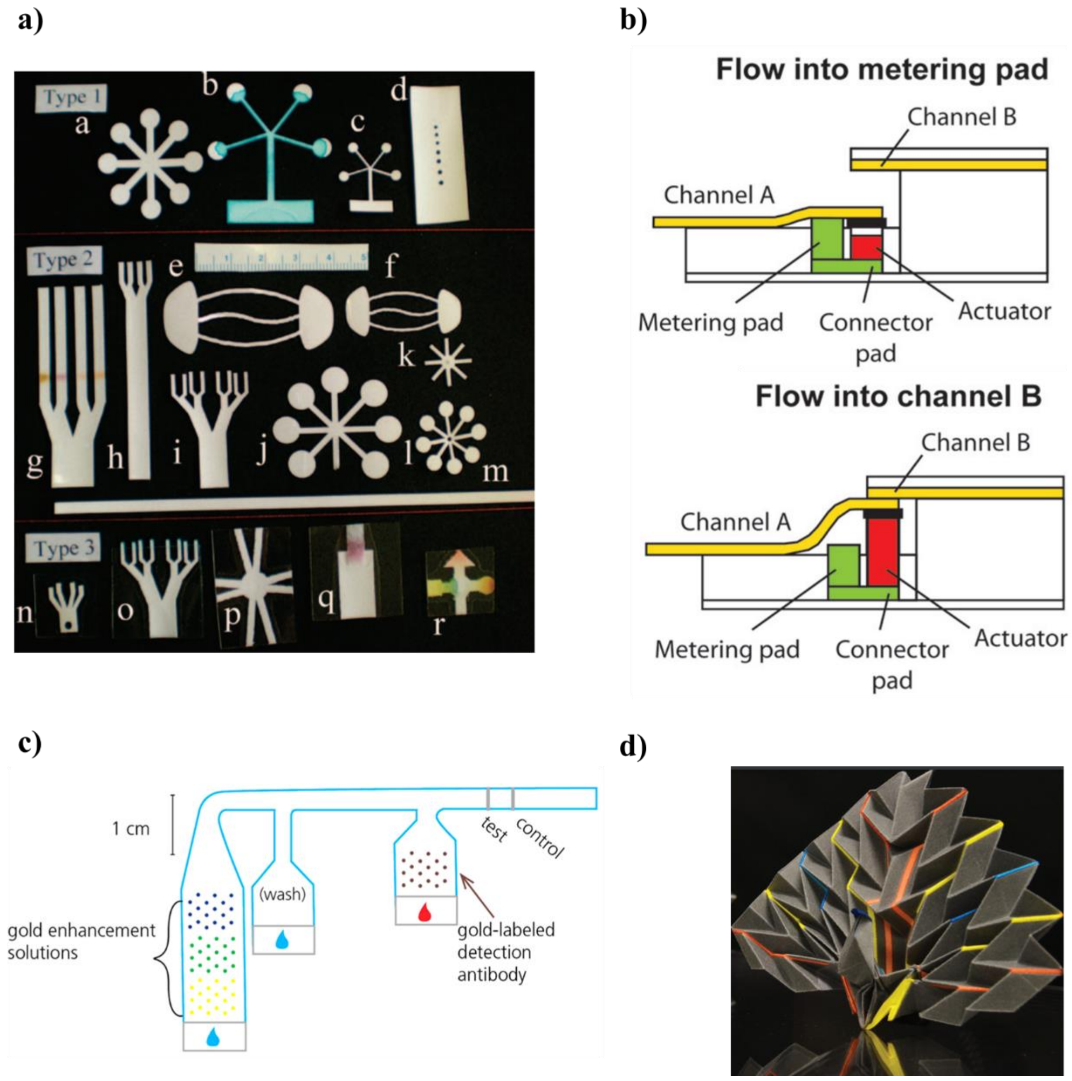

Fig. 1.3 Selected functionalities and capabilities. a) Array of different geometric shapes (Fenton et al. 2009). b) Switch created by an expandable actuator (Toley et al. 2015). c) Sequential delivery method (Fridley et al. 2014). d) Origami paper-based microfluidics (Kalish and Tsutsui 2014).

1.5. Conclusion

Since the first seminal work by Martinez et al. (2007), the rapid development of paper-based microfluidic devices have allowed for a wide range of medical and chemical diagnostic applications. The low-cost and ease-of-use of point-of-care technologies have allowed them to be more accessible to those in low-resource settings. A large variety of fabrication techniques have been adapted from other fields. Though still considered to be in the early stages of development, paper-based microfluidics' increasing sophistication has led to successful implementation of a variety of detection techniques, each with its advantages and disadvantages. These sophisticated detection techniques require increasingly complex chemistry, which has led to the creation of fluid controlled mechanisms. The understating of these mechanisms and thereby improved controllability of fluid imbibition will lead to more accurate and precise analytical devices.

References

Abe K, Suzuki K, Citterio D (2008) Inkjet-printed microfluidic multianalyte chemical sensing paper Anal Chem 80:6928-6934 doi:10.1021/ac800604v

Ali MM, Aguirre SD, Xu YQ, Filipe CDM, Pelton R, Li YF (2009) Detection of DNA using bioactive paper strips Chem Commun:6640-6642 doi:10.1039/b911559e

Carrilho E, Martinez AW, Whitesides GM (2009) Understanding Wax Printing: A Simple Micropatterning Process for Paper-Based Microfluidics Anal Chem 81:7091-7095 doi:10.1021/ac901071p

Cate DM, Adkins JA, Mettakoonpitak J, Henry CS (2015) Recent Developments in Paper-Based Microfluidic Devices Anal Chem 87:19-41 doi:Doi 10.1021/Ac503968p

Chen H, Cogswell J, Anagnostopoulos C, Faghri M (2012) A fluidic diode, valves, and a sequential-loading circuit fabricated on layered paper Lab Chip 12:2909-2913 doi:Doi 10.1039/C2lc20970e

Delaney JL, Hogan CF, Tian JF, Shen W (2011) Electrogenerated Chemiluminescence Detection in Paper-Based Microfluidic Sensors Anal Chem 83:1300-1306 doi:10.1021/ac102392t

Dungchai W, Chailapakul O, Henry CS (2009) Electrochemical Detection for Paper-Based Microfluidics Anal Chem 81:5821-5826 doi:Doi 10.1021/Ac9007573

Dungchai W, Chailapakul O, Henry CS (2011) A low-cost, simple, and rapid fabrication method for paper-based microfluidics using wax screen-printing Analyst 136:77-82 doi:10.1039/c0an00406e

Evans E, Gabriel EFM, Coltro WKT, Garcia CD (2014) Rational selection of substrates to improve color intensity and uniformity on microfluidic paper-based analytical devices Analyst 139:2127-2132 doi:10.1039/c4an00230j

Fenton EM, Mascarenas MR, Lopez GP, Sibbett SS (2009) Multiplex Lateral-Flow Test Strips Fabricated by Two-Dimensional Shaping Acs Appl Mater Inter 1:124-129 doi:Doi 10.1021/Am800043z

Fridley GE, Le H, Yager P (2014) Highly Sensitive Immunoassay Based on Controlled Rehydration of Patterned Reagents in a 2-Dimensional Paper Network Anal Chem 86:6447-6453 doi:10.1021/ac500872j

Fu E, Kauffman P, Lutz B, Yager P (2010) Chemical signal amplification in two-dimensional paper networks Sensor Actuat B-Chem 149:325-328 doi:Doi 10.1016/J.Snb.2010.06.024

Fu E, Liang T, Spicar-Mihalic P, Houghtaling J, Ramachandran S, Yager P (2012) Two-Dimensional Paper Network Format That Enables Simple Multistep Assays for Use in Low-Resource Settings in the Context of Malaria Antigen Detection Anal Chem 84:4574-4579 doi:Doi 10.1021/Ac300689s

Hossain SMZ, Luckham RE, McFadden MJ, Brennan JD (2009) Reagentless Bidirectional Lateral Flow Bioactive Paper Sensors for Detection of Pesticides in Beverage and Food Samples Anal Chem 81:9055-9064 doi:10.1021/ac901714h

Houghtaling J, Liang T, Thiessen G, Fu E (2013) Dissolvable Bridges for Manipulating Fluid Volumes in Paper Networks Anal Chem 85:11201-11204 doi:10.1021/ac4022677

Kalish B, Tsutsui H (2014) Patterned adhesive enables construction of nonplanar three-dimensional paper microfluidic circuits Lab Chip 14:4354-4361 doi:10.1039/c4lc00730a

Kalish B, Tsutsui H (2016) Using Adhesive Patterning to Construct 3D Paper Microfluidic Devices Journal of visualized experiments : JoVE doi:10.3791/53805

Kauffman P, Fu E, Lutz B, Yager P (2010) Visualization and measurement of flow in two-dimensional paper networks Lab Chip 10:2614-2617 doi:Doi 10.1039/C004766j

Khan MS, Li X, Shen W, Garnier G (2010) Thermal stability of bioactive enzymatic papers Colloid Surface B 75:239-246 doi:10.1016/j.colsurfb.2009.08.042

Lewis GG, DiTucci MJ, Baker MS, Phillips ST (2012) High throughput method for prototyping three-dimensional, paper-based microfluidic devices Lab Chip 12:2630-2633 doi:10.1039/c2lc40331e

Li X, Tian JF, Garnier G, Shen W (2010) Fabrication of paper-based microfluidic sensors by printing Colloid Surface B 76:564-570 doi:Doi 10.1016/J.Colsurfb.2009.12.023

Li X, Tian JF, Nguyen T, Shen W (2008) Paper-Based Microfluidic Devices by Plasma Treatment Anal Chem 80:9131-9134 doi:10.1021/ac801729t

Li X, Zwanenburg P, Liu XY (2013) Magnetic timing valves for fluid control in paper-based microfluidics Lab Chip 13:2609-2614 doi:10.1039/c3lc00006k

Liu H, Crooks RM (2011) Three-Dimensional Paper Microfluidic Devices Assembled Using the Principles of Origami J Am Chem Soc 133:17564-17566 doi:Doi 10.1021/Ja2071779

Lopez-Ruiz N, Curto VF, Erenas MM, Benito-Lopez F, Diamond D, Palma AJ, Capitan-Vallvey LF (2014) Smartphone-Based Simultaneous pH and Nitrite Colorimetric Determination for Paper Microfluidic Devices Anal Chem 86:9554-9562 doi:10.1021/ac5019205

Lu Y, Shi WW, Jiang L, Qin JH, Lin BC (2009) Rapid prototyping of paper-based microfluidics with wax for low-cost, portable bioassay Electrophoresis 30:1497-1500 doi:Doi 10.1002/Elps.200800563

Lutz B, Liang T, Fu E, Ramachandran S, Kauffman P, Yager P (2013) Dissolvable fluidic time delays for programming multi-step assays in instrument-free paper diagnostics Lab Chip 13:2840-2847 doi:10.1039/c3lc50178g

Lutz BR, Trinh P, Ball C, Fu E, Yager P (2011) Two-dimensional paper networks: programmable fluidic disconnects for multi-step processes in shaped paper Lab Chip 11:4274-4278 doi:10.1039/c1lc20758j

Martinez AW, Phillips ST, Butte MJ, Whitesides GM (2007) Patterned paper as a platform for inexpensive, low-volume, portable bioassays Angew Chem Int Edit 46:1318-1320 doi:Doi 10.1002/Anie.200603817

Martinez AW, Phillips ST, Carrilho E, Thomas SW, Sindi H, Whitesides GM (2008a) Simple telemedicine for developing regions: Camera phones and paper-based microfluidic devices for real-time, off-site diagnosis Anal Chem 80:3699-3707 doi:10.1021/ac800112r

Martinez AW, Phillips ST, Whitesides GM (2008b) Three-dimensional microfluidic devices fabricated in layered paper and tape P Natl Acad Sci USA 105:19606-19611 doi:DOI 10.1073/pnas.0810903105

Martinez AW, Phillips ST, Wiley BJ, Gupta M, Whitesides GM (2008c) FLASH: A rapid method for prototyping paper-based microfluidic devices Lab Chip 8:2146-2150 doi:10.1039/b811135a

Nie JF, Liang YZ, Zhang Y, Le SW, Li DN, Zhang SB (2013) One-step patterning of hollow microstructures in paper by laser cutting to create microfluidic analytical devices Analyst 138:671-676 doi:Doi 10.1039/C2an36219h

Nie ZH et al. (2010) Electrochemical sensing in paper-based microfluidic devices Lab Chip 10:477-483 doi:10.1039/b917150a

Noh H, Phillips ST (2010) Fluidic Timers for Time-Dependent, Point-of-Care Assays on Paper Anal Chem 82:8071-8078 doi:10.1021/ac1005537

Noiphung J, Songjaroen T, Dungchai W, Henry CS, Chailapakul O, Laiwattanapaisal W (2013) Electrochemical detection of glucose from whole blood using paper-based microfluidic devices Anal Chim Acta 788:39-45 doi:10.1016/j.aca.2013.06.021

Olkkonen J, Lehtinen K, Erho T (2010) Flexographically Printed Fluidic Structures in Paper Anal Chem 82:10246-10250 doi:Doi 10.1021/Ac1027066

Osborn JL, Lutz B, Fu E, Kauffman P, Stevens DY, Yager P (2010) Microfluidics without pumps: reinventing the T-sensor and H-filter in paper networks Lab Chip 10:2659-2665 doi:10.1039/c004821f

Renault C, Li X, Fosdick SE, Crooks RM (2013) Hollow-channel paper analytical devices Anal Chem 85:7976-7979 doi:10.1021/ac401786h

Santhiago M, Kubota LT (2013) A new approach for paper-based analytical devices with electrochemical detection based on graphite pencil electrodes Sensor Actuat B-Chem 177:224-230 doi:10.1016/j.snb.2012.11.002

Shen L, Hagen JA, Papautsky I (2012) Point-of-care colorimetric detection with a smartphone Lab Chip 12:4240-4243 doi:10.1039/c2lc40741h

Songjaroen T, Dungchai W, Chailapakul O, Laiwattanapaisal W (2011) Novel, simple and low-cost alternative method for fabrication of paper-based microfluidics by wax dipping Talanta 85:2587-2593 doi:10.1016/j.talanta.2011.08.024

Su M, Ge L, Ge SG, Li NQ, Yu JH, Yan M, Huang JD (2014) Paper-based electrochemical cyto-device for sensitive detection of cancer cells and in situ anticancer drug screening Anal Chim Acta 847:1-9 doi:10.1016/j.aca.2014.08.013

Taudte RV, Beavis A, Wilson-Wilde L, Roux C, Doble P, Blanes L (2013) A portable explosive detector based on fluorescence quenching of pyrene deposited on coloured wax-printed mu PADs Lab Chip 13:4164-4172 doi:10.1039/c3lc50609f

Thom NK, Yeung K, Pillion MB, Phillips ST (2012) "Fluidic batteries" as low-cost sources of power in paper-based microfluidic devices Lab Chip 12:1768-1770 doi:10.1039/c2lc40126f

Toley BJ, McKenzie B, Liang T, Buser JR, Yager P, Fu E (2013) Tunable-Delay Shunts for Paper Microfluidic Devices Anal Chem 85:11545-11552 doi:Doi 10.1021/Ac4030939

Toley BJ et al. (2015) A versatile valving toolkit for automating fluidic operations in paper microfluidic devices Lab Chip 15:1432-1444 doi:10.1039/c4lc01155d

Wang SM, Ge L, Song XR, Yu JH, Ge SG, Huang JD, Zeng F (2012) Paper-based chemiluminescence ELISA: Lab-on-paper based on chitosan modified paper device and wax-screen-printing Biosensors & bioelectronics 31:212-218 doi:Doi 10.1016/J.Bios.2011.10.019

Yetisen AK, Akram MS, Lowe CR (2013) Paper-based microfluidic point-of-care diagnostic devices Lab Chip 13:2210-2251 doi:10.1039/c3lc50169h

2. TOWARD UNDERSTANDING IMBIBITION IN PAPER-BASED MICROFLUIDICS

2.1. Introduction

Paper-based microfluidic devices have gained an increasing amount of interest over the last few years. Satisfying the World Health Organization's (WHO) recommended ASSURED criteria (Affordable, Sensitive, Specific, User-friendly, Rapid and robust, Equipment-free, Deliverable) (Kettler et al. 2004), paper-based microfluidics have made point-of-care (POC) testing more accessible. Current applications, range from healthcare (Hu et al. 2014; Martinez et al. 2007), to food safety (Hossain et al. 2009), and to environmental monitoring, among others. What has attracted attention is the speed and ease of manufacturing, the low-cost, and the adaptability of these paper devices.

Compared to conventional microfluidic devices, the paper-based counterparts are able to utilize paper's inherent wicking property to eliminate need for the external pumping to drive the fluid. Channels are easily formed by either selectively removing sections of the paper substrate or by patterning channel boundaries with a hydrophobic material. The former methods ranges from using high-precision CO_2 laser-cutting (Chitnis et al. 2011; Fu et al. 2010b) to craft cutting (Fenton et al. 2009), while the latter methods range from those of photolithography (Martinez et al. 2008c) to techniques using commercially available printers with inkjet (Abe et al. 2010) or solid ink (Carrilho et al. 2009). Ultimately, the shared result of these fabrication methods is the creation of defined impermeable boundaries for fluid transport. Thorough reviews on the variety of available fabrication methods have recently been published (Jiang and Fan 2016; Xia et al. 2016; Yetisen et al. 2013).

Paper, composed of cellulosic fibers, has similar properties to that of pure cellulose, such as a high affinity for water, swelling during liquid uptake, biocompatibility, and biodegradability. For detailed properties of cellulose, see the thorough reviews (Eichhorn et al. 2001; Klemm et al. 2005; Moon et al. 2011). Paper is a ubiquitous material that is often assumed to be a simple material. In actuality, paper is a intricate structure of intertwining fibers. During liquid imbibition, flow is described by complex transport theory. Paper’s non-uniformity arises from its manufacturing process, where the stochastic nature of fiber suspension, pressing, and drying leads to an anisotropic fiber network. Accurate calculation of imbibition parameters such as pore size distribution, porosity, interconnectivity, and internal permeability are especially difficult due to paper’s inherent disorder. The development of structural models from simple capillary tubes to random network models have allowed for the better understanding and characterization of liquid imbibition

As such, for devices to continue to advance toward more complex and sophisticated functions, obtaining accurate and consistent fluid imbibition will become increasingly important. The purpose of this chapter is to expose the reader to fundamental aspects of paper and its liquid imbibition. Understanding the essentials of imbibition in paper-based microfluidics will allow the further design of precise and reproducible paper-based microfluidic devices.

2.2. Characteristics of paper

Paper is an abundant and ubiquitous material. As a diagnostic platform, paper has been of interest since the 19th century, when urine test strips were first developed (Clarke and Foster 2012). What makes paper particularly attractive to the paper-based microfluidic community is its low-cost, the wide range of available paper grades, and its inherent wicking properties. What gives paper its desired characteristics are the cellulosic fibers and the pore properties. For a full description of the chemical and physical properties of cellulose, see comprehensive reviews (Credou and Berthelot 2014; Klemm et al. 2005; Moon et al. 2011).

2.2.1. Paper

Paper is produced from an aqueous suspension of cellulose fibers primarily derived from wood and cotton. The general manufacturing process entails drawing such aqueous suspensions through a sieve, pressing the remaining product, and finally drying which results in an interconnected network of cellulose fibers. The final composition and characteristics of the paper are highly dependent on the suspension's drawing process. This highly dynamic and random process is what gives paper its anisotropic nature and inhomogeneity. Careful optimization of this process is what gives paper its physical properties such as pore size distribution, porosity, and interconnectivity. Furthermore, to improve the surface quality of the paper or alter wicking properties, many additives and fillers can be added. These include sizing agents such as alkyl ketene dimer (AKD) and alkenyl succinic anhydride (ASA) (Bracher et al. 2010; Hubbe et al. 2007; Modaressi and

Garnier 2002) and super absorbent polymers (Hua and Qian 2001). The range of potential additives can also produce papers not suitable for imbibition such as regular printing paper where additives improve the paper surface while reducing porosity (smooth surface). Another unfavorable paper for applications are high absorbent substrates such as paper towels where uneven liquid uptake is seen (Zhong et al. 2012). In the paper-based microfluidic field high quality cellulose of at least 98% alpha-cellulose if often used, such as papers are associated with filter and chromatography applications.

2.2.2. Paper Structure

As mentioned earlier, the paper manufacturing process, especially during fiber suspension, gives paper the majority of its fiber network properties such as porosity and pore size distribution. Being a highly dynamic process, the aggregation, or so called flocculation of the fibers are dependent on a variety of forces including electrostatic, colloidal, and mechanical (Alava and Niskanen 2006). This process, albeit controlled, leads to local inhomogeneity that can influence paper's bulk properties. This non-uniformity can be seen when the paper is held to a light, as shown in Fig. 2.1 This shows a qualitative visual representation of the mass variation within the paper structure. Since the paper is pressed, the mass variation might give rise to a range of porosities and pore sizes along the thickness of the paper.

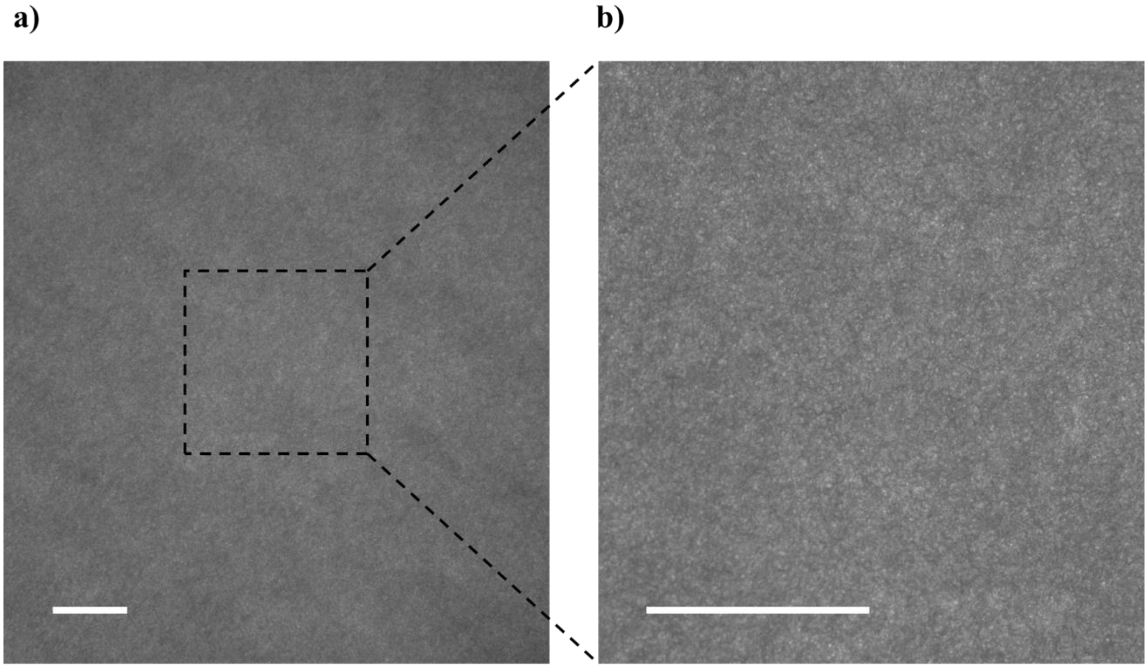

Fig. 2.1 Whatman #1 filter paper showing non-uniformity of fiber distribution. a) Bulk paper image (grey scale). b) Zoomed in image (grey scale). Scale bar: 10 mm.

The anisotropy of paper makes modeling the structure particularly difficult. The simplest and most widely used model is that of the Lucas-Washburn (L-W) equation, where paper is represented as a bundle of uniform capillary tubes. This is obviously physical inaccurate, but allows the characterization and prediction of flow from effective parameters extracted from experimental data. Alternatively, the paper can be modeled as an isotropic media where the liquid flow is taken as unsaturated. In this approach, the flow and paper substrate properties can be coupled into a permeability term.

More accurate models for paper structure are network pore and random fiber network models where the paper structure is modelled to be more realistically. In network pore models the paper structure is represented by a discrete set of connected pore channels. These can be as simple as one-dimensional connected capillary tubes of varying sizes (Fig. 2.2a) (Dullien 1991; Ruoff et al. 1960). More organized structures such as a network unit cell (Ridgway et al. 2002) or organized periodic cylinders (Blunt 2001; Hayes et al. 2000; Ruoff et al. 1960) have also been proposed. In these more organized structures, the pore size is controlled by varying the space and stacking orientation of the rigid cylinders (Fig. 2.2b). More realistic pore network models utilize pseudo-random pore channels, where the paper structure is represented by an array of pore throats and pore bodies (Fig. 2.2c) (Ghassemzadeh and Sahimi 2004; Wiklund and Uesaka 2012).

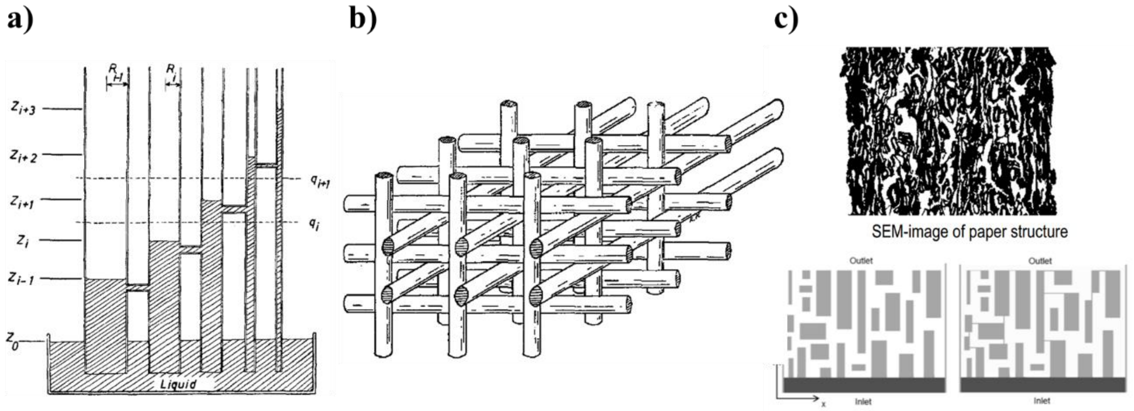

Fig. 2.2 Pore network structure model. a) Capillary tubes of varying sizes (Ruoff et al. 1960). b) Organized stacked solid fibers (Ruoff et al. 1960). c) SEM image of paper with represented pore throats and pore bodies (Wiklund and Uesaka 2012).

To truly capture the anisotropic structure of paper, random fiber networks can be utilized. Here, fibers are randomly oriented to produce a fibrous network that resembles that of paper (Jaganathan et al. 2009; Koponen et al. 1998) (Fig. 2.3a). These model structures are useful to study the dependence of fiber orientation on imbibition (Ashari et al. 2010) (Fig. 2.3b), the dependence of fiber distribution on permeability (Qi and Uesaka 1996) (Fig. 2.3c), study wetting dynamics of adjacent fibers (Sauret et al. 2015), study two-dimensional to three-dimensional fiber network scaling (Hatami-Marbini 2016) (Fig. 2.3d), and study the degree of randomness and fiber structure on liquid uptake (Thompson 2002).

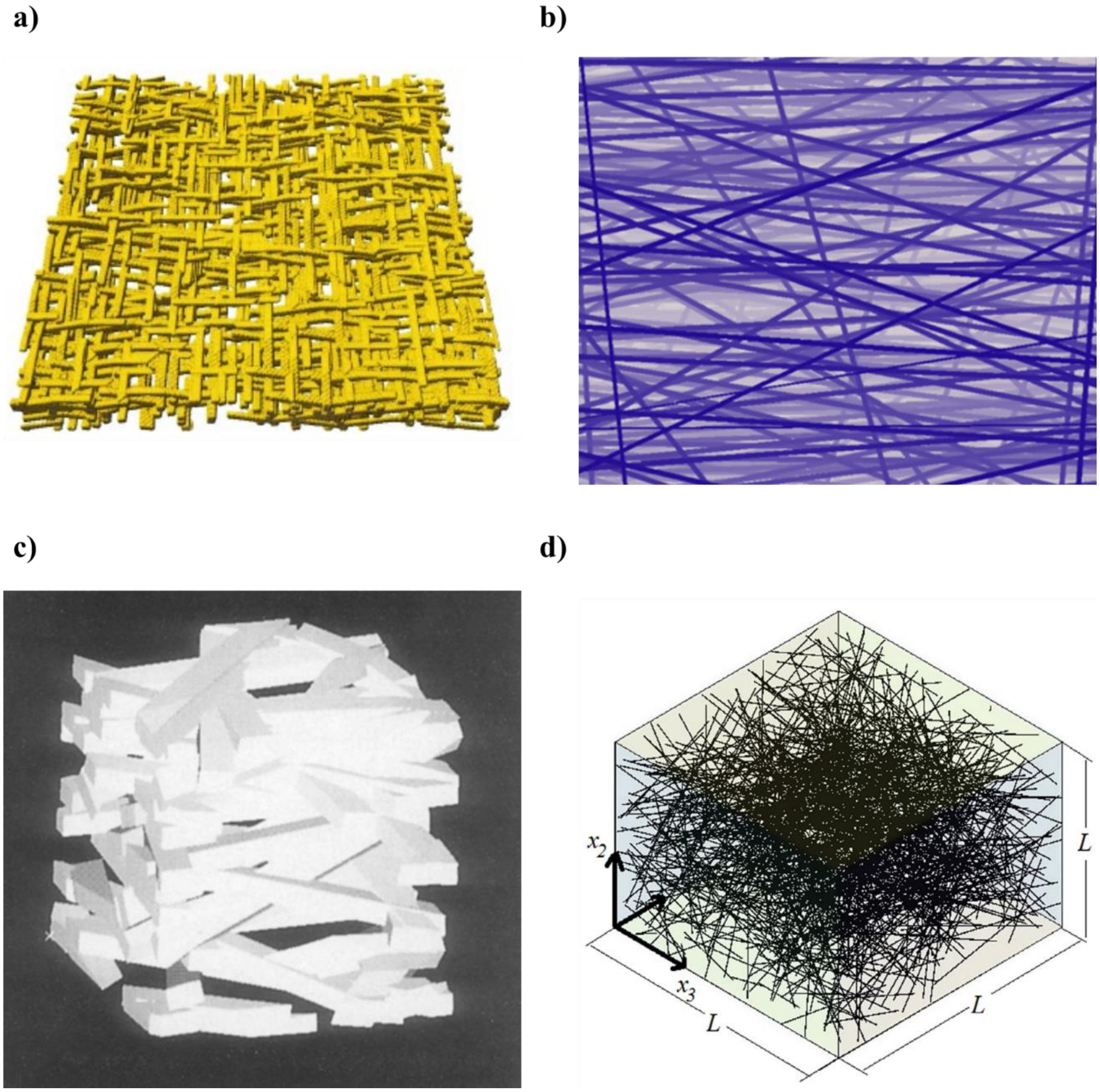

Fig. 2.3 Random fiber networks. a) Fibrous network (Koponen et al. 1998). b) Differently oriented fibers (Ashari et al. 2010). c) Varying fiber distribution (Qi and Uesaka 1996). d) 2-D to 3-D random scaling (Hatami-Marbini 2016).

As simple as paper might seem, the randomness and anisotropic structure of the fiber network make modeling approaches difficult, computationally intense, or, to some degree, physically inaccurate. The nature of paper’s structure and its liquid imbibition has created analogies to percolation theory and fractal geometry (Hunt 2005). For a detailed description, see (Isichenko 1992; Sahimi 1993; Wang et al. 2002). Along with percolation behavior, the dynamic interface at the liquid front is an area of interest, primarily due to direct applications ranging from film growth (Forgerini and Marchiori 2014) to fracture phenomena (Engoy et al. 1994). The dynamic interface at the liquid front is largely attributed to the kinetic roughening created by the random structure encountered during the imbibition process (Alava et al. 2004). An abundance of studies have used paper as a model substrate to investigate roughening (Balankin et al. 2013; Balankin et al. 2006; Horvath and Stanley 1995; Kwon et al. 1996). The pinning behavior and fingering phenomenon seen at the liquid front during imbibition (Fig. 2.4) is attributed to roughening dynamics, which can be augmented by adding inhibitory agents onto the paper (Lutz et al. 2013).

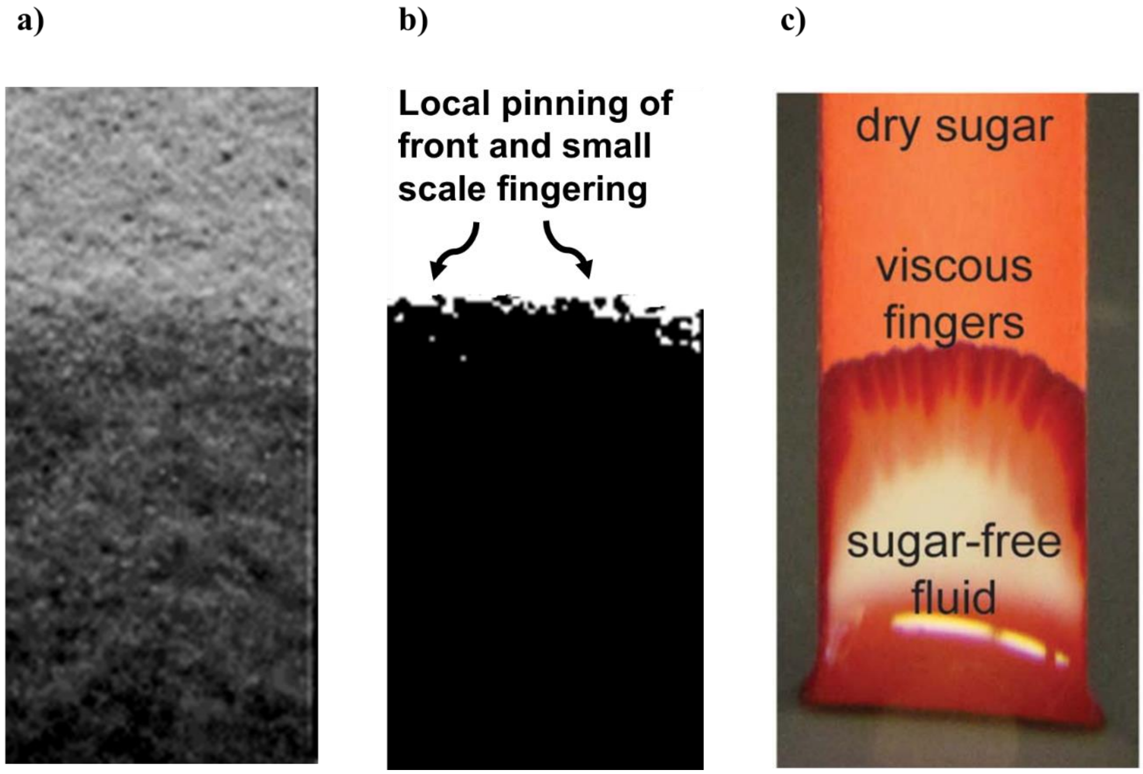

Fig. 2.4 Pinning behavior and fingering phenomena. a) Filter paper during imbibition (grey scale). b) Black and white image showing pinning behavior. c) Extreme fingering phenomena due to adding inhibitory agent (Lutz et al. 2013).

2.3. Imbibition in paper media

Fluid penetration into paper-like or porous media is a highly complex process. The detailed description is governed by many length and time-scaled parameters which are highly coupled. While the flow and detailed physics take place within the micro- and macro-structure of the porous media, the underlining interest lies in the macroscopic regime. Darcy, in the 19th century, found that flow is proportional to the pressure gradient applied across the porous substrate. This is analytically presented as,

$$v = -\frac{k}{\mu}\nabla p\,, \tag{2.1}$$

where v is the average liquid velocity, k is the permeability of the substrate, which describes the ease of fluid penetration, μ is the dynamic viscosity, and ∇p is the pressure gradient across the porous substrate. Since then, flow in porous materials have been modeled as simple capillary tubes to highly complex network models associated with percolation phenomena. Given the complexity of the structure in paper media, certain conditions and assumptions are placed within the developed models. Emphasis will be placed on two fundamental modeling approaches; capillary tube flow and diffusion-like flow.

2.3.1. Capillary tube flow

The simplest way to model imbibition is by treating the porous substrate as a bundle of parallel rigid capillary tubes of uniform size with an infinite liquid reservoir at the inlet. The liquid front movement is governed by a single representative capillary tube with generally four main forces influencing the flow: the suction force created by the interfacial pressure different at the meniscus, the viscous force, the gravitational force, and the force due to inertia. As shown schematically in Fig. 2.5, a capillary tube of diameter D contains two immiscible fluids (here liquid and air) immersed in an infinite reservoir at ambient pressure. A meniscus is formed at the interface and in combination with the surface tension γ creates a pressure difference (suction) denoted in the Young-Laplace equation as the capillary pressure,

$$P_c = \frac{4\gamma\cos\theta}{D}, \tag{2.2}$$

where θ is the static contact angle.

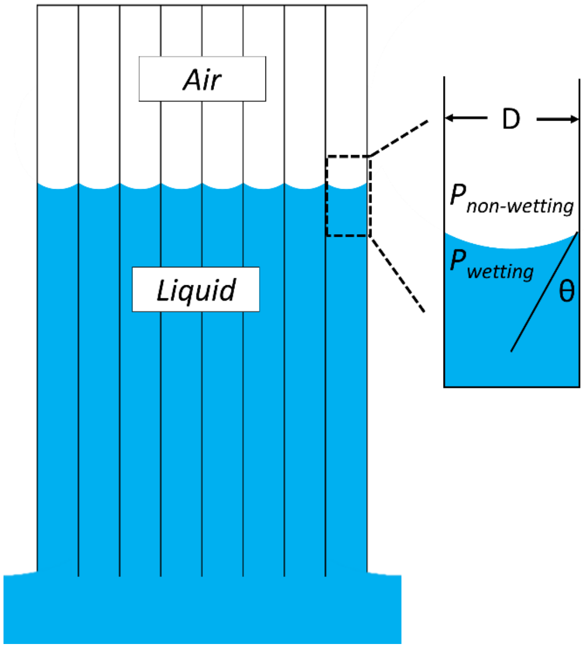

Fig. 2.5 Representative porous substrate using a bundle of capillary tubes.

The momentum balance of the capillary front yields (Fries and Dreyer 2008; Zhmud et al. 2000),

$$\rho\frac{d}{dt}\left(h\frac{dh}{dt}\right) = \frac{4\gamma\cos\theta}{D} - \frac{32\mu}{D^2}h\frac{dh}{dt} - \rho gh, \tag{2.3}$$

where ρ is the liquid density, and h is the height of the meniscus. The left hand side represents the force due to inertia while the right hand side represents the capillary pressure (suction), viscous force represented by Hagen-Poiseuille flow, and the gravitational force, respectively. An analytical solution to Eq. 2.3 is not possible, though numerical methods such as the Runge-Kutta method have previously been used (Szekely et al. 1971). The gravitational effect generally plays a negligible role for short distance imbibition, around 10% of the final equilibrium height (Fries and Dreyer 2008). Inspecting the Bond number which quantifies the ratio between body forces to surface tension forces, adds support to this claim. The influence of the inertial term has been investigated by Rideal (1922) and Bosquanet (1923) which determined that inertia is only important in the very early stages of imbibition when the imbibition distance was found to be linearly proportional to time or when the capillary is large. Hence, the inertia term is often ignored. Therefore, for paper imbibition, gravity and inertia are ignored and Eq. 2.3 becomes,

$$\frac{4\gamma\cos\theta}{D} = \frac{32\mu}{D^2} h \frac{dh}{dt} \tag{2.4}$$

where the capillary pressure is balanced by the viscous force. Solving Eq. 2.4 with initial conditions $h(t=0)=0$ results in the widely used Lucas-Washburn (L-W) equation,

$$h = \sqrt{\frac{D\gamma\cos\theta}{4\mu} t}\ , \tag{2.5}$$

where the distance is proportional to the square root of time.

2.3.2. Modification and application of Lucas-Washburn equation to paper media

The Lucas-Washburn equation gives a simple model of imbibition by representing the porous substrate as a bundle of capillary tubes. Paper, to some extent, is not an ideal substrate for modeling purposes. The nature and structure of the media produces inherent complexities, such as random fibrous networks and paper's hygroscopic properties. From the need to model imbibition data more accurately, several modifications to the L-W equation have been proposed. In coming sections we look at some of these parameters.

2.3.3. Effective diameter

The governing Eq. 2.3 represents a perfect capillary tube. In porous materials, this is obviously not the case. Therefore, a slight modification is needed. Often the flow is modified by represented diameters. As follows,

$$\frac{4\gamma\cos\theta}{D} = \frac{32\mu}{{D_h}^2} h \frac{dh}{dt} \tag{2.6}$$

Where D is the static diameter of the pore and D_h is the hydrodynamic diameter of the represented capillary tube (Fries et al. 2008; Masoodi and Pillai 2010). Solving Eq. 2.6 produces,

$$h = \sqrt{\frac{D_e \gamma \cos\theta}{4\mu} t} \ , \tag{2.7}$$

where D_e is the effective diameter given by $D_e = {D_h}^2 \big/ D$. The use of this substitution has been proposed to improve the accuracy in modeling polymer wicks (Masoodi et al. 2007) and metal weaves (Fries et al. 2008). For paper-like media, the static and hydrodynamic diameters are difficult to obtain due to the complex structure, therefore the effective diameter is taken as the represented diameter of the substrate having no physical significance other than as a measure of the ease of liquid penetration.

The effective diameter generally gives values two orders of magnitude less than the actual physical pore size of the substrate (Dullien et al. 1977; Ruoff et al. 1960). The effective diameter has been proposed as a way of incorporating tortuosity (Lundblad and Bergman 1997) as well as other complex structures of the substrate (Schuchardt and Berg 1991).

The form of the L-W equation shown in Eq. 2.7 is the most widely recognized model for characterizing imbibition in the field of paper-based microfluidics. This is primarily because of its straight forward approach and ease-of-use. It has been used to characterize one-dimensional imbibition numerous times (Bohm et al. 2014; Jafry et al. 2016; Lutz et al. 2013). It has also served to compare and be the basis to model two-dimensional flows within paper-like media (Benner and Petsev 2013; Elizalde et al. 2015; Fu et al. 2011; Shou et al. 2014).

2.3.4. Permeability

Permeability is an alternative to the effective diameter, and a represented value in describing the ease of fluid penetration which is generally a material specific property. In relating the interstitial velocity (Hagen-Poiseuille flow) of the capillary to the superficial velocity (Darcy), the relationship,

$$\frac{8}{{D_e}^2} = \frac{\phi}{K}, \tag{2.8}$$

gives the capillary model permeability (Masoodi and Pillai 2010), where ϕ is the porosity and K is the effective permeability. This can be substituted into Eq. 2.7 to produce an alternative form of the Lucas-Washburn equation,

$$h = \sqrt{\left(\frac{2K}{\phi}\right)^2 \frac{\gamma\cos\theta}{\mu} t} \ . \tag{2.9}$$

Aside from the permeability relation of Eq. 2.8, other permeability relationships have been proposed, generally in the form,

$$K = \psi {D_e}^2 \tag{2.10}$$

where ψ is a function of the substrate geometry (Kao and Hunt 1996).

Once of these permeability relationships, the Kozeny-Carman equation has frequently been used (Wyllie and Gregory 1955; Xu and Yu 2008). It was developed for a pack bed of solids. For paper, more appropriate permeability relations are those developed for fiber beds using analytical, numerical, and experimental methods, such as those from Gebart (1992), Van der Westhuizen et al. (1996), and Nabovati et al. (2009). Numerous others have been developed. The aforementioned are briefly summarized in Table 2.1. Using these types of relationships would be difficult for paper-like media due to the dependence of porosity and fiber properties. Fibers, being hygroscopic and absorbent, the porosity and fiber properties are humidity and fluid dependent. Nevertheless, studies investigating permeability relationships would undoubtedly be beneficial to the paper-based microfluidic community.

Current studies in modifying and adjusting the permeability of the paper have been shown to be effective in controlling the liquid flow. These methods, among others, include using hydrophobic polymers (Bohm et al. 2014; Noh and Phillips 2010; Weng et al. 2014) that are deposited onto the paper substrate to delay liquid flow, using dissolvable and erodible barriers (Jahanshahi-Anbuhi et al. 2014; Lutz et al. 2013) to create time delay barriers, as well as physical methods such as compressing paper (Park et al. 2016) and selectively cutting the paper (Giokas et al. 2014; Renault et al. 2013).

Table 2.1 Selected permeability relations.

Permeability relations		**Developed for**
Kozeny-Carman equations	$K = D^2 \dfrac{\phi^3}{180(1-\phi)^2}$	Pack bed of solids
Gebart	$K = \dfrac{d^2}{4} C \left(\sqrt{\dfrac{1-\phi_c}{1-\phi}} - 1 \right)^{5/2}$	Close-packed fibers
Van der Westhuizen et al.	$K = \dfrac{d^2}{4} \pi\phi \left(\dfrac{\left(1-\sqrt{1-\phi}\right)^2}{24(1-\phi)^{3/2}} \right)$	Random unidirectional fiber beds
Nabovati et al.	$K = \dfrac{d^2}{4} C_1 \left(\sqrt{\dfrac{1-\phi_c}{1-\phi}} - 1 \right)^{C_2}$	3-D random fiber network
D, pore diameter ; d, fiber diameter;; C, C_1, C_2 geometric factors ϕ_c , critical value of porosity below which there is no permeating flow		

2.3.5. Tortuosity

Tortuosity τ is a quantitative value describing how tortuous the system is. It is dependent on the topology of the media, which includes the porosity and the interconnectivity of the microstructure. It also has a direct contribution to the permeability of the substrate (Cai and Yu 2011; Hodgson and Berg 1988; Liu et al. 2016). To obtain a better representation of the complex structure of the media, attempts have been made to isolate the tortuosity from the effective diameter and its corresponding effective permeability. It is quantitatively defined as the ratio between the actual length traveled, L_f to the straight-line length, L_s. Analytically this is represented as, $\tau = \left(\frac{L_f}{L_s}\right)^2$ (Benavente et al. 2002) or $\tau = \frac{L_f}{L_s}$ (Cai et al. 2010).

In paper-like media, tortuosity is difficult to obtain and arguably impossible to accurately measure due to its complex structure. Nevertheless, a simple modification to the Lucas-Washburn equation is often used,

$$h = \sqrt{\frac{D_e \gamma \cos\theta}{4\mu\tau^2} t} \tag{2.11}$$

As seen in Eq. 2.11, the tortuosity modified the L-W equation (Cai et al. 2010; Hodgson and Berg 1988) serves as a direct modification to the effective diameters by decoupling the effect of the tortuous internal structure. Though Eq. 2.11 is not directly derived from capillary theory, the tortuosity factor serves as a great relative comparison between similar substrates.

Largely driven by observations of cotton fabrics not following the L-W behavior, (Laughlin and Davies 1961), attempts to better relate the tortuosity to the topology of the substrate have been proposed. Random porous media have been characterized by fractal theory, such as, paper (Kopelman et al. 1986), soil (Perfect and Kay 1991), and porous fabrics (Yu and Lee 2002), among others. Wheatcraft and Tyler (1988) proposed that the fractal path traveled by a particle through heterogeneous porous media is,

$$L_f = \varepsilon^{1-d_T} L_s^{\,d_T} \qquad (2.12)$$

where ε is the scale of observation and d_T is the fractal dimension. Simply put, the fractal dimension serves as a way to describe the complexity of a pattern within a designated space. Yu and Cheng (2002) proposed that the pore diameter D can be implemented as the scale of observation. Therefore,

$$L_f = D^{1-d_T} L_s^{\,d_T} \ . \qquad (2.13)$$

Derived from capillary theory and the fractal dimension relation, the imbibition distance can be described by (Cai et al. 2010),

$$L_s = \left(\frac{\gamma \cos\theta}{4\mu D^{1-2d_T}} t \right)^{1/2d_T} \qquad (2.14)$$

when the fractal dimension d_T is a single capillary, $d_T = 1$, and Eq. 2.14 reduces to the L-W equation (Eq. 2.7).

2.3.6. Contact angle

The contact angle in the L-W equation is that from the contact angle formed under static conditions in a single capillary. This was done for simplification purposes. It is known that the contact angle is associated with the speed of the moving front (Degennes 1985; Dussan 1979) as well as to the internal structure of the substrate. There have been many investigations as to the importance of this dynamic contact angle (Hamraoui and Nylander 2002; Marmur 1992; Martic et al. 2002).

Bracke et al. (1989) proposed that the dynamic contact angle θ_d and the static contact angle θ_s are related by,

$$\frac{\cos\theta_d - \cos\theta_s}{\cos\theta_s + 1} = -2Ca^{1/2} \tag{2.15}$$

where Ca is the capillary number, $Ca = \frac{\mu v}{\gamma}$. However, the front speed does not change significantly, except briefly during the initial imbibition and upon reaching its final position. Therefore, the contact angle can be taken as a static value, which is frequently done.

For cellulose, the static contact angle has been shown to be approximately 26° (Joubert et al. 1959; Liukkonen 1997); however, due to the high water affinity of cellulose, the contact angle quickly reduces to 0° (Liukkonen 1997). Therefore, for paper-based microfluidics, specifically for cellulose based substrates, a contact angle of 0° is appropriate.

2.3.7. Swelling

Swelling of the substrate up to this point has largely been neglected, primarily due to imbibition models assuming a rigid structure, which makes the final solutions relatively simple. One can argue that because the effective diameter and effective permeability are represented parameters, the effects of swelling can be incorporated into these values. This is what has generally been done in the paper-based microfluidics community, however cellulose has a high affinity to water. It’s been shown that a single fiber can expand up to 85% (Mantanis et al. 1995). Therefore, for paper-based microfluidics, swelling is a major influence during imbibition dynamics. This has a noteworthy affect in topology parameters such as permeability and porosity.

Accurately incorporating swelling in the initial stages of model derivation is simple in concept since porosity and liquid uptake of the substrate can be made to be time dependent. Unfortunately, practical implementation produces immensely complicated relationships due to the system becoming a deformable porous media (Ambrosi 2002; Diersch et al. 2010; Spiegelman 1993).

Attempts have been made to produce straightforward models (i.e. less accurate) while still implementing the overall swelling effects. Schuchardt and Berg (1991) incorporated swelling through a linear function,

$$D = D_0 - \beta t \tag{2.16}$$

where D is the pore diameter, D_0 is the pore diameter “seen” by the meniscus, and β is a fitting constant representing the rate of constriction. Incorporating Eq. 2.16 in the capillary model results in,

$$h = \sqrt{\frac{D_0 \gamma \cos\theta}{4\mu}\left(t - \frac{2\beta}{D_0}t^2 + \frac{4\beta^2}{3{D_0}^2}t^3\right)} \tag{2.17}$$

Note, when $\beta = 0$, Eq. 2.17 reduces to the traditional L-W equation (Eq. 2.7). Eq. 2.17 has been shown to agree favorably with experimental data. Based on the Schuchardt and Berg's swelling relation (Eq. 2.16), constrictions will become more apparent as time increases. Therefore, caution should be taken as to not allow imbibition time to surpass the maximum swelling time (porosity dependent).

Masoodi et al. (2010) proposed a more complex model derived by using Darcy's equation and by incorporating sink terms in the mass conservations,

$$h = \sqrt{\frac{2P_c}{\phi\mu} e^{(b-1)\frac{\phi}{\phi 0}} \int_0^t e^{(b-1)\frac{\phi}{\phi 0}} K(t')dt'} \tag{2.18}$$

where ϕ_0 is the porosity in front of the meniscus, *b* is a fitted absorbent coefficient, and *K(t')* is a time dependent permeability utilizing the same linear relationship (Eq. 2.16) as Schuchardt and Berg.

2.3.8. Humidity effects

Non-ideal environmental conditions such as changing humidity, can play a significant role in imbibition. Most significantly is evaporation and, when dealing with a hygroscopic material, residual saturation as well. Studying imbibition alongside evaporation can be difficult to model and characterize primarily due to influences from factors such as fluctuations in air flow and variations of evaporation across the substrate.

In the paper-based microfluidics community, humidity effects can typically be eliminated by confining the device (Schilling et al. 2012; Toley et al. 2013), but in general humidity effects are largely ignored. The significant influence of evaporation has sparked some researchers to incorporate such inhibitory effects within the modeling process (Camplisson et al. 2015; Jahanshahi-Anbuhi et al. 2014; Mendez et al. 2010). The majority of these studies have adopted the capillary model with evaporation by Fries et al. (2008). This model incorporates a uniform constant evaporation flux from the surface in the mass conservation. The derived model, neglecting gravity, results in,

$$h = \sqrt{\frac{a}{b} - \frac{a}{b} e^{-2bt}} \quad \text{with } a = \frac{4\gamma \cos\theta}{\phi\mu} \frac{K}{D}; \; b = \frac{\dot{m}_e (W + T)}{\rho W T \phi} \tag{2.19}$$

where $\dot{m}_e$ is the evaporation rate, W is the width of the substrate, and T is the thickness of the substrate. A large portion of the mentioned studies utilize the correlation found in the ASHRAE handbook to estimate the evaporation rate.

$$\dot{m}_e = (P_w - P_v) \frac{0.089 + 0.0782 V_{air}}{Y} \tag{2.20}$$

where P_w is the saturated pressure, P_v is the partial pressure of vapor, V_{air} is the air flow speed, and Y is the heat of vaporization of water. Though Eq. 2.20 is a good estimate, caution should be taken depending in the type of substrate being used, as the ASHRAE correlation is for evaporation of static pool surfaces. Nevertheless, with no convection effects, evaporation from a porous surface behaves as a fully wetted surface, provided the pore size is small relative to the size of the surface (Beyhaghi et al. 2014).

The constant evaporation flux assumption was questioned (Barry et al. 2009) in Fries et al. (2008). Veran-Tissoires et al. (2012) computationally determined that the evaporation flux in Fries et al. would result in a non-uniform evaporation flux distribution, with a much higher flux within the imbibition front surface.

Evaporation is not the only result from humidity, residual saturation can also occur, especially for paper substrates, due to cellulose's hygroscopic property. Depending on the degree of humidity the paper can become moist by developing some degree of saturation. This such parameter has been implemented into Fries et al. (2008) by a multiplicative adjustment (Jahanshahi-Anbuhi et al. 2014) due to the paper's water content. A more analytical approach was done to model initially moist soils (Kao and Hunt 1996). By modeling the soil as a capillary tube, the capillary diameter was adjusted by an initial saturation to account for the reduction in volume due to the liquid coated internal wall.

Aside from evaporation and saturation, humidity will influence other crucial paper-based microfluidic qualities such as device handling, shelf life, and moisture sensitive chemistry. To our best knowledge no studies have been done to investigate these potential issues for paper-based applications.

2.3.9. Diffusion-like model

The L-W equation is widely used and frequently researched in liquid penetration applications. It is widely known that paper's pores do not resemble the idealized capillary tubes. This has led to a wide range of modifications with the aim of obtaining a slightly more accurate model. The key disadvantage in using the L-W model for porous materials is the assumption of a saturated flow front (e.g. completely wet or complexly dry). Macroscopic observations have clearly shown this is not the case (Alava et al. 2004; Alava and Niskanen 2006).

Diffusion-like models aim to surpass this binary flow by treating the porous material as an unsaturated flow. Diffusion-like models emphasize concepts to obtain valuable predictions. The underlying mechanism of liquid penetration is not caused by molecular diffusion, but by mechanisms analogous to diffusion. Unlike capillary flows where the system is binary wetting; fully saturated or fully dry, flow in porous media, particularly hygroscopic systems, a gradient of liquid is seen during the advancing of the front (see Fig. 2.6). These models are often used in soil science, therefore such terminology will be used while placing emphasis on important concepts.

To our best knowledge, no application of diffusion-like theory has specifically been applied in the field of paper-based microfluidics. This is likely because the saturation gradient at the front is seen to be of little interest. But as Berli et al. (2016) has pointed out, during solute capture in lateral flow assays, concentrations are important for efficient detection. As such gradients at the liquid front will have a direct impact on detection. Nonetheless, the paper-based microfluidics community should be aware due to the saturation/wetting dependent parameters mentioned in previous sections.

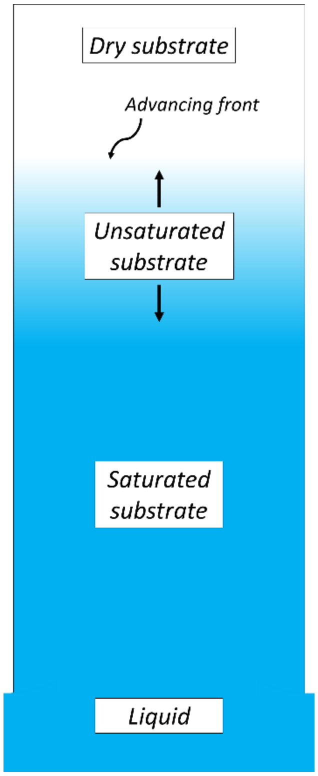

Fig. 2.6 Unsaturated flow in a porous substrate.

2.3.10. Richard's equation

The fundamental equation governing unsaturated flows is the Richard's equation (Richards 1931), which is derived by assuming permeability and suction are dependent on volumetric water content, θ. These assumptions, along with Darcy's law and mass conservation, leads to,

$$\frac{\partial\theta}{\partial t}=\frac{\partial}{\partial x}\left(\tilde{K}(\theta)\frac{\partial\Psi}{\partial x}\right) \tag{2.21}$$

where $\tilde{K}(\theta)$ is the hydraulic conductivity and Ψ is the pressure head (suction). Eq. 2.21 can also be rewritten as,

$$\frac{\partial \Theta}{\partial t} = \frac{\partial}{\partial x}\left(D(\Theta) \frac{\partial \Theta}{\partial x} \right) \tag{2.22}$$

where $D(\Theta) = \tilde{K}(\theta)\frac{\partial \Psi}{\partial \theta}$ and is referred to as the water diffusivity. Eq. 2.21 can also be written in several other formulations, other with or without a gravity term (Ashari et al. 2010; Gillespie 1959; Jaganathan et al. 2009; Kao and Hunt 1996; Lockington et al. 2007; Ruoff et al. 1960). For clarity, saturation, Θ, is defined as the ratio between volumetric water content and porosity, $\Theta = \frac{\theta}{\phi}$. The system is fully saturated when volumetric water content and porosity are equal. Due to the high non-linearity of Eq. 2.22, an analytical solution is seldom attainable. In order for the Richard's equation to be solvable, the permeability and pressure head need to be functions of saturation (Jaganathan et al. 2009).

2.3.11. Permeability and pressure head

Similarly to the L-W equation, permeability is key to obtaining useful results. The most widely used formulation to model permeability is the Brook and Corey (1964) power law relationship,

$$K(\Theta) = K_s \Theta^n \tag{2.23}$$

where K_s represents the intrinsic permeability (e.g. Darcy permeability) of the material. Since in Eq. 2.23 K_s represents the intrinsic permeability, the power function can be taken as the relative permeability being a function of saturation. This is frequently shown as

$K(\Theta) = K_s K_r$ (Jaganathan et al. 2009; Nilsson and Stenstrom 1997). Therefore, if the flow is not fully saturated, the permeability will be reduced.

Suction pressure, similar to permeability, is also saturation dependent. This is seen from the water diffusivity of Eq. 2.22. Brook and Corey (1964) proposed that the capillary pressure follows,

$$P_c = P_b (\Theta)^{-1/\lambda} \tag{2.24}$$

where P_b is a constant parameter of the substrate measuring the maximum pore size forming a continuous network of flow channels within the substrate and λ is also a constant parameter which characterizes the pore size distribution.

2.4. Characterizing flow

Attaining consistent and precise liquid control is desired when designing paper-based microfluidics devices. This is achieved by applying the theoretical knowledge and building a fluid control framework through experimentation. Unlike the numerous fabrication methods available, in the context of paper-based microfluidics, development of this experimental framework has not been as rapid. Characterization of the fluid flow serves to both visually validate observe flow behavior and associated predictions.

2.4.1. Flow visualization

Visualizing fluid flows is a valuable tool to researchers and to paper device designers. It is often necessary to obtain flow characterization and gives visual feedback of flow dynamics. The easiest and widely used method is to record the imbibition process and subsequently measuring the liquid front (Elizalde et al. 2016; Fu et al. 2010b; Tian et al. 2016) (Fig. 2.7a). To better visualize the liquid front, a high contrast dye can be used, but is not required. Caution should be taken when using dyes at high concentrations, as clogging of the pores may occur in addition to dye-water separation. As an alternative to dyes, fluorescent markers can also be used (Hong and Kim 2015; Kauffman et al. 2010) (Fig. 2.7b). A key advantage of fluorescent visualization, is that concentration gradients within the flow can be seen. This can aid in optimizing detection zones and delivery methods for the desired concentrations. To visualize such flow profiles, (Kauffman et al. 2010) developed an electrochemical marking method where a pH sensitive marker is used. Flow profiles are observed by varying the local pH through cycling electrical pulses (Fig. 2.7c). Bathany et al. (2015) used a more advanced electrochemical system to measure real-time liquid uptake in paper-based devices. Their system records the amperometric signal created in the electrolyte solution as it moves through the paper device.

Computational simulations are also used, especially when detailed characterization is desired. Martic et al. (2002; 2004) used molecular dynamic simulations to study the early stages of the velocity dependent contact angle. Simulations can be particular important when the channel design increases in complexity. Fu et al. (2010a) and Masoodi et al. (2011) used simulations to validate and visualize flow in expanding and contracting channels. Mendez et al. (2010) similarly validated results in fan-shaped porous channels. WitkowskaNery et al. (2016) investigated an array of channel geometries where computational simulations were used to optimize the channel geometry for glucose and uric acid detection (Fig. 2.7d). Using electrochemical measurements along the channel allowed them to obtained concentration reading. Which compared to simulations, showed good agreement to each other.

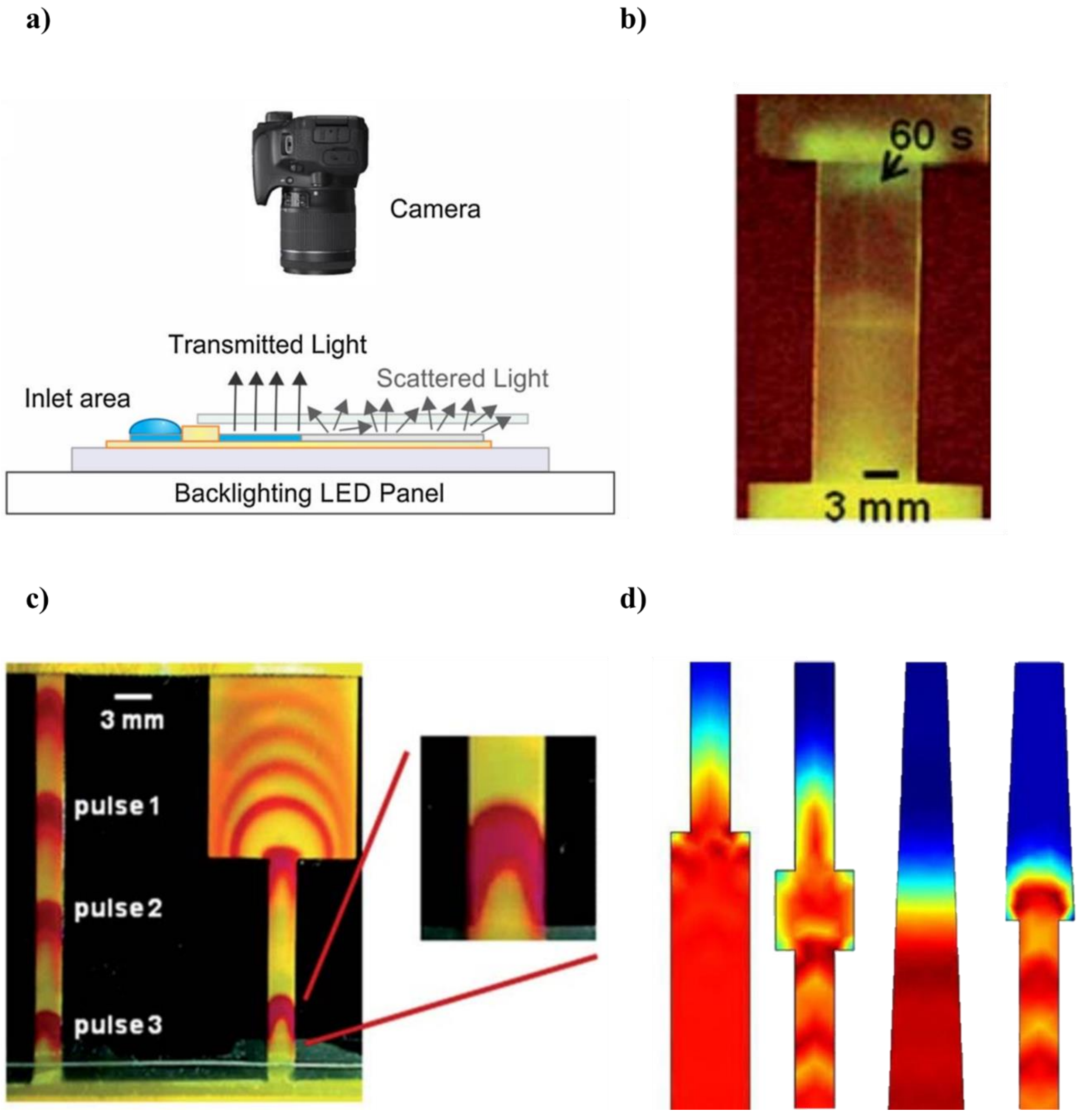

Fig. 2.7 Flow visualization. a) Optically measuring dye front (Elizalde et al. 2016). b) Using fluorescence intensity (Kauffman et al. 2010). c) Electrochemical system set-up (Kauffman et al. 2010). d) Computer simulations (WitkowskaNery et al. 2016).

As beneficial as these simulations are, a key disadvantage over experimentally determined flow, is the paper structure itself. As mentioned in earlier sections, modeling the paper structure is especially difficult due to its anisotropy and inhomogeneity, which can lead to inaccurate fluid flow representation. Advanced imaging methods however have enabled the accurate representation of the paper structure and fluid flow. Nuclear magnetic resonance (NMR) cryoporometry has frequently been used in the geology and soil science field to non-destructively determine pore parameter such as the porosity and pore size distribution of the material (Gane et al. 2004; Strange et al. 1993). For a detailed review see (Mitchell et al. 2008). The NMR technique has been applied to paper for determining porosity and pore size distribution as well as to characterize the morphology of the paper (Capitani et al. 2002). NMR has also been used to evaluate the moisture content (Froix and Nelson 1975) and to determine the diffusivity coefficient with relation to moisture content (Topgaard and Soderman 2001). de Azevedo et al. (2008) used magnetic resonance imaging (MRI) to determine the diffusivity of paper fibers. They were able to characterize imbibition in unsized paper and determine the existence of a precursor film that develops in front of the macroscopic liquid front.

Imbibition simulations using accurate representation of the paper structure can be done using x-ray imaging techniques. In x-ray microtomography, a large number of two-dimensional projections of the material can be combined to reconstruct the paper sample. Hyvaluoma et al. (2006) used this technique to study radial liquid penetration in paper board, which is a much thicker form of paper. They determined that unidirectional penetration is described well by the L-W equation. They also theorized that the leading liquid front proceeds along fibers, a similar conclusion to that of de Azevedo et al. (2008). Lavrykov et al. (2016) developed a technique to determine the directional permeabilities of the paper substrate. By using x-ray microtomography, the three-dimensional paper reconstruction was able to be skeletonize. Once skeletonize, simulations allowed the resistances and tortuosities to be correlated to permeabilities.

X-ray microtomography has also been used to study the link between paper's manufacturing process and its microstructure and the mechanical properties of the fibers (Marulier et al. 2012). Using x-ray densitometry, a detailed visualization of the imbibition in paper can be obtained (Beuther et al. 2010). From these images, the roughening of the liquid front can be seen in detail along with potential precursor films and the liquid gradients assumed in Richard's equations.

2.5. Conclusion

Paper-based microfluidics has generated a great amount of interest for the development of diagnostic and self-contained analytical devices. They are inexpensive, rapid, and user-friendly making them ideal diagnostic tools for resource limited settings. Obtaining precise fluid control during imbibition will allow for more sophisticated device functions. Paper being the main substrate is a versatile material readily available with an array of appealing physical properties. Understanding the transport properties of paper and its interaction with water has led to an understanding of complex fibrous structures. The highly stochastic nature of the paper manufacturing process leads to a high anisotropic material where the macroscopic flow in paper is influenced by the microscopic arrangement of cellulose fibers and pore space. This complicates the modeling of the structure which leads to physical inaccuracies during fluid characterization. Models ranging from simple capillary tubes to highly dynamic percolation theory and fractal geometry have been implemented. The advanced and sophisticated models are valuable in understanding the detailed dynamics occurring within and during the imbibition process. However, practical implementation of these models under the context of paper-based microfluidic devices is lacking mainly due to the extensive empirical model parameters required to reproduce the highly dynamic imbibition phenomena. Consequently, the Lucas-Washburn model is still widely used by the paper-based microfluidic community due to its simplicity, ease-of-use, and adequate accuracy for the current characterization needs.

References

Abe K, Kotera K, Suzuki K, Citterio D (2010) Inkjet-printed paperfluidic immuno-chemical sensing device Anal Bioanal Chem 398:885-893 doi:10.1007/s00216-010-4011-2

Alava M, Dube M, Rost M (2004) Imbibition in disordered media Adv Phys 53:83-175 doi:Doi 10.1080/00018730410001687363

Alava M, Niskanen K (2006) The physics of paper Rep Prog Phys 69:669-723 doi:Doi 10.1088/0034-4885/69/3/R03

Allen SG, Stephenson PCL, Strange JH (1997) Morphology of porous media studied by nuclear magnetic resonance J Chem Phys 106:7802-7809 doi:Doi 10.1063/1.473780

Ambrosi D (2002) Infiltration through deformable porous media Z Angew Math Mech 82:115-124 doi:Doi 10.1002/1521-4001(200202)82:2<115::Aid-Zamm115>3.0.Co;2-4

Ashari A, Bucher TM, Tafreshi HV, Tahir MA, Rahman MSA (2010) Modeling fluid spread in thin fibrous sheets: Effects of fiber orientation Int J Heat Mass Tran 53:1750-1758 doi:10.1016/j.ijheatmasstransfer.2010.01.015

Balankin AS, Lopez HZ, Leon EP, Matamoros DM, Ruiz LM, Lopez DS, Rodriguez MA (2013) Depinning and dynamics of imbibition fronts in paper under increasing ambient humidity Phys Rev E 87 doi:Artn 014102
Doi 10.1103/Physreve.87.014102

Balankin AS, Paredes RG, Susarrey O, Morales D, Vacio FC (2006) Kinetic roughening and pinning of two coupled interfaces in disordered media Phys Rev Lett 96 doi:Artn 056101
10.1103/Physrevlett.96.056101

Barry DA, Parlange JY, Lockington DA, Wissmeier L (2009) Comment on "The effect of evaporation on the wicking of liquids into a metallic weave" by N. Fries, K. Odic, M. Conrath and M. Dreyer J Colloid Interf Sci 336:374-375 doi:Doi 10.1016/J.Jcis.2009.04.006

Bathany C, Han JR, Abi-Samra K, Takayama S, Cho YK (2015) An electrochemical-sensor system for real-time flow measurements in porous materials Biosensors & bioelectronics 70:115-121 doi:10.1016/j.bios.2015.03.002

Benavente D, Lock P, Del Cura MAG, Ordonez S (2002) Predicting the capillary imbibition of porous rocks from microstructure Transport Porous Med 49:59-76 doi:Doi 10.1023/A:1016047122877

Benner EM, Petsev DN (2013) Potential flow in the presence of a sudden expansion: Application to capillary driven transport in porous media Phys Rev E 87 doi:Artn 033008
Doi 10.1103/Physreve.87.033008

Berli CLA, Kler PA (2016) A quantitative model for lateral flow assays Microfluid Nanofluid 20 doi:Artn 104
10.1007/S10404-016-1771-9

Beuther PD, Veith MW, Zwick KJ (2010) Characterization of Absorbent Flow Rate in Towel and Tissue J Eng Fiber Fabr 5:1-7

Beyhaghi S, Geoffroy S, Prat M, Pillai KM (2014) Wicking and evaporation of liquids in porous wicks: A simple analytical approach to optimization of wick design Aiche J 60:1930-1940 doi:10.1002/aic.14353

Blunt MJ (2001) Flow in porous media - pore-network models and multiphase flow Curr Opin Colloid In 6:197-207 doi:Doi 10.1016/S1359-0294(01)00084-X

Bohm A, Carstens F, Trieb C, Schabel S, Biesalski M (2014) Engineering microfluidic papers: effect of fiber source and paper sheet properties on capillary-driven fluid flow Microfluid Nanofluid 16:789-799 doi:10.1007/s10404-013-1324-4

Bosanquet CH (1923) On the flow of liquids into capillary tubes. Philos Mag 45:525-531

Bracher PJ, Gupta M, Whitesides GM (2010) Patterned paper as a template for the delivery of reactants in the fabrication of planar materials Soft Matter 6:4303-4309 doi:10.1039/c0sm00031k

Bracke M, Devoeght F, Joos P (1989) The Kinetics of Wetting - the Dynamic Contact-Angle Prog Coll Pol Sci S 79:142-149

Brooks RH, Corey AT Hydraulic Properties of Porous Media. In, Colorado State University, 1964. Hydrology Papers

Cai JC, Yu BM (2011) A Discussion of the Effect of Tortuosity on the Capillary Imbibition in Porous Media Transport Porous Med 89:251-263 doi:DOI 10.1007/s11242-011-9767-0

Cai JC, Yu BM, Mei MF, Luo L (2010) Capillary Rise in a Single Tortuous Capillary Chinese Phys Lett 27 doi:Artn 054701 10.1088/0256-307x/27/5/054701

Camplisson CK, Schilling KM, Pedrotti WL, Stone HA, Martinez AW (2015) Two-ply channels for faster wicking in paper-based microfluidic devices Lab Chip 15:4461-4466 doi:10.1039/c5lc01115a

Capitani D, Proietti N, Ziarelli F, Segre AL (2002) NMR study of water-filled pores in one of the most widely used polymeric material: The paper Macromolecules 35:5536-5543 doi:10.1021/ma020174w

Carrilho E, Martinez AW, Whitesides GM (2009) Understanding Wax Printing: A Simple Micropatterning Process for Paper-Based Microfluidics Anal Chem 81:7091-7095 doi:10.1021/ac901071p

Chitnis G, Ding ZW, Chang CL, Savran CA, Ziaie B (2011) Laser-treated hydrophobic paper: an inexpensive microfluidic platform Lab Chip 11:1161-1165 doi:10.1039/c0lc00512f

Clarke SE, Foster JR (2012) A history of blood glucose meters and their role in self-monitoring of diabetes mellitus Brit J Biomed Sci 69:83-93

Credou J, Berthelot T (2014) Cellulose: from biocompatible to bioactive material J Mater Chem B 2:4767-4788 doi:10.1039/c4tb00431k

de Azevedo EN, Alme LR, Engelsberg M, Fossum JO, Dommersnes P (2008) Fluid imbibition in paper fibers: Precursor front Phys Rev E 78 doi:Artn 066317 10.1103/Physreve.78.066317

Degennes PG (1985) Wetting - Statics and Dynamics Rev Mod Phys 57:827-863 doi:DOI 10.1103/RevModPhys.57.827

Diersch HJG et al. (2010) Modeling Unsaturated Flow in Absorbent Swelling Porous Media: Part 1. Theory Transport Porous Med 83:437-464 doi:10.1007/s11242-009-9454-6

Dullien FAL (1991) Characterization of Porous-Media - Pore Level Transport Porous Med 6:581-606

Dullien FAL, Elsayed MS, Batra VK (1977) Rate of Capillary Rise in Porous-Media with Nonuniform Pores J Colloid Interf Sci 60:497-506 doi:Doi 10.1016/0021-9797(77)90314-9

Dussan EB (1979) Spreading of Liquids on Solid-Surfaces - Static and Dynamic Contact Lines Annu Rev Fluid Mech 11:371-400 doi:DOI 10.1146/annurev.fl.11.010179.002103

Eichhorn SJ et al. (2001) Review: Current international research into cellulosic fibres and composites J Mater Sci 36:2107-2131 doi:Doi 10.1023/A:1017512029696

Elizalde E, Urteaga R, Berli CLA (2015) Rational design of capillary-driven flows for paper-based microfluidics Lab Chip 15:2173-2180 doi:10.1039/c4lc01487a

Elizalde E, Urteaga R, Berli CLA (2016) Precise capillary flow for paper-based viscometry Microfluid Nanofluid 20 doi:10.1007/s10404-016-1800-8

Engoy T, Maloy KJ, Hansen A, Roux S (1994) Roughness of two-dimensional cracks in wood Phys Rev Lett 73:834-837 doi:10.1103/PhysRevLett.73.834

Fenton EM, Mascarenas MR, Lopez GP, Sibbett SS (2009) Multiplex Lateral-Flow Test Strips Fabricated by Two-Dimensional Shaping Acs Appl Mater Inter 1:124-129 doi:Doi 10.1021/Am800043z

Forgerini FL, Marchiori R (2014) A brief review of mathematical models of thin film growth and surfaces. A possible route to avoid defects in stents Biomatter 4:e28871 doi:10.4161/biom.28871

Fries N, Dreyer M (2008) An analytic solution of capillary rise restrained by gravity J Colloid Interf Sci 320:259-263 doi:DOI 10.1016/j.jcis.2008.01.009

Fries N, Odic K, Conrath M, Dreyer M (2008) The effect of evaporation on the wicking of liquids into a metallic weave J Colloid Interf Sci 321:118-129 doi:Doi 10.1016/J.Jcis.2008.01.019

Froix MF, Nelson R (1975) Interaction of Water with Cellulose from Nuclear Magnetic-Resonance Relaxation-Times Macromolecules 8:726-730 doi:Doi 10.1021/Ma60048a011

Fu E, Kauffman P, Lutz B, Yager P (2010a) Chemical signal amplification in two-dimensional paper networks Sensor Actuat B-Chem 149:325-328 doi:Doi 10.1016/J.Snb.2010.06.024

Fu E, Lutz B, Kauffman P, Yager P (2010b) Controlled reagent transport in disposable 2D paper networks Lab Chip 10:918-920 doi:10.1039/b919614e

Fu EL, Ramsey S, Kauffman P, Lutz B, Yager P (2011) Transport in two-dimensional paper networks Microfluid Nanofluid 10:29-35 doi:Doi 10.1007/S10404-010-0643-Y

Gane PAC et al. (2004) Comparison of NMR cryoporometry, mercury intrusion porosimetry, and DSC thermoporosimetry in characterizing pore size distributions of compressed finely ground calcium carbonate structures Ind Eng Chem Res 43:7920-7927 doi:10.1021/ie049448p

Gebart BR (1992) Permeability of Unidirectional Reinforcements for Rtm J Compos Mater 26:1100-1133 doi:Doi 10.1177/002199839202600802

Ghassemzadeh J, Sahimi M (2004) Pore network simulation of fluid imbibition into paper during coating: II. Characterization of paper's morphology and computation of its effective permeability tensor Chem Eng Sci 59:2265-2280 doi:10.1016/j.ces.2004.01.057

Gillespie T (1959) The Capillary Rise of a Liquid in a Vertical Strip of Filter Paper Journal of Colloid Science 14:123-130

Giokas DL, Tsogas GZ, Vlessidis AG (2014) Programming Fluid Transport in Paper-Based Microfluidic Devices Using Razor-Crafted Open Channels Anal Chem 86:6202-6207 doi:10.1021/ac501273v

Hamraoui A, Nylander T (2002) Analytical approach for the Lucas-Washburn equation J Colloid Interf Sci 250:415-421 doi:DOI 10.1006/jcis.2002.8288

Hatami-Marbini H (2016) Scaling properties of three-dimensional random fibre networks Phil Mag Lett 96:165-174 doi:10.1080/14786435.2016.1177223

Hayes RE, Bertrand FH, Tanguy PA (2000) Modelling of fluid/paper interaction in the application nip of a film coater Transport Porous Med 40:55-72 doi:Doi 10.1023/A:1006680607586

Hodgson KT, Berg JC (1988) The Effect of Surfactants on Wicking Flow in Fiber Networks J Colloid Interf Sci 121:22-31 doi:Doi 10.1016/0021-9797(88)90404-3

Hong S, Kim W (2015) Dynamics of water imbibition through paper channels with wax boundaries Microfluid Nanofluid 19:845-853 doi:10.1007/s10404-015-1611-3

Horvath VK, Stanley HE (1995) Temporal Scaling of Interfaces Propagating in Porous-Media Phys Rev E 52:5166-5169 doi:DOI 10.1103/PhysRevE.52.5166

Hossain SMZ, Luckham RE, McFadden MJ, Brennan JD (2009) Reagentless Bidirectional Lateral Flow Bioactive Paper Sensors for Detection of Pesticides in Beverage and Food Samples Anal Chem 81:9055-9064 doi:10.1021/ac901714h

Hu J, Wang SQ, Wang L, Li F, Pingguan-Murphy B, Lu TJ, Xu F (2014) Advances in paper-based point-of-care diagnostics Biosensors & bioelectronics 54:585-597 doi:Doi 10.1016/J.Bios.2013.10.075

Hua FJ, Qian MP (2001) Synthesis of self-crosslinking sodium polyacrylate hydrogel and water-absorbing mechanism J Mater Sci 36:731-738 doi:Doi 10.1023/A:1004849210718

Hubbe MA, Venditti RA, Rojas OJ (2007) What Happens to Cellulosic Fibers during Papermaking and Recycling? A Review Bioresources 2:739-788

Hunt AG (2005) Basic transport properties in natural porous media - Continuum percolation theory and fractal model Complexity 10:22-37 doi:10.1002/cplx.20067

Hyvaluoma J, Raiskinmaki P, Jasberg A, Koponen A, Kataja M, Timonen J (2006) Simulation of liquid penetration in paper Phys Rev E 73 doi:Artn 036705 10.1103/Physreve.73.036705

Isichenko MB (1992) Percolation, Statistical Topography, and Transport in Random-Media Rev Mod Phys 64:961-1043 doi:DOI 10.1103/RevModPhys.64.961

Jafry AT, Lim H, Kang SI, Suk JW, Lee J (2016) comparative study of paper-based microfluidic devices with respect to channel geometry Colloid Surface A 492:190-198 doi:10.1016/j.colsurfa.2015.12.033

Jaganathan S, Tafreshi HV, Pourdeyhimi B (2009) A realistic modeling of fluid infiltration in thin fibrous sheets J Appl Phys 105 doi:Artn 113522
Doi 10.1063/1.3141737

Jahanshahi-Anbuhi S et al. (2014) Paper-based microfluidics with an erodible polymeric bridge giving controlled release and timed flow shutoff Lab Chip 14:229-236 doi:10.1039/c3lc50762a

Jiang X, Fan ZH (2016) Fabrication and Operation of Paper-Based Analytical Devices Annual review of analytical chemistry 9:203-222 doi:10.1146/annurev-anchem-071015-041714

Joubert JM, Krige GJR, Borgin K (1959) Evidence for a Hydrate of Cellulose from Studies of Its Surface Properties Nature 184:1561-1562 doi:Doi 10.1038/1841561b0

Kao CS, Hunt JR (1996) Prediction of wetting front movement during one-dimensional infiltration into soils Water Resour Res 32:55-64 doi:Doi 10.1029/95wr02974

Kauffman P, Fu E, Lutz B, Yager P (2010) Visualization and measurement of flow in two-dimensional paper networks Lab Chip 10:2614-2617 doi:Doi 10.1039/C004766j

Kettler H, White K, Hawkes S (2004) Mapping the landscape of diagnostics for sexually transmitted infections World Health Organization

Klemm D, Heublein B, Fink HP, Bohn A (2005) Cellulose: Fascinating biopolymer and sustainable raw material Angew Chem Int Edit 44:3358-3393 doi:10.1002/anie.200460587

Kopelman R, Parus S, Prasad J (1986) Fractal-Like Exciton Kinetics in Porous Glasses, Organic Membranes, and Filter Papers Phys Rev Lett 56:1742-1745 doi:DOI 10.1103/PhysRevLett.56.1742

Koponen A et al. (1998) Permeability of three-dimensional random fiber webs Phys Rev Lett 80:716-719 doi:DOI 10.1103/PhysRevLett.80.716

Kwon TH, Hopkins AE, ODonnell SE (1996) Dynamic scaling behavior of a growing self-affine fractal interface in a paper-towel-wetting experiment Phys Rev E 54:685-690 doi:DOI 10.1103/PhysRevE.54.685

Landeryou M, Eames I, Cottenden A (2005) Infiltration into inclined fibrous sheets J Fluid Mech 529:173-193 doi:10.1017/S0022112005003356

Laughlin RD, Davies JE (1961) Some Aspects of Capillary Absorption in Fibrous Textile Wicking Text Res J 31:904-910

Lavrykov S, Singh SK, Ramarao BV, Ramaswamy S, Pande H (2016) Analysis of the permeability tensor and the correlation length of heterogeneities in paper using X-ray microtomography Dry Technol 34:871-882 doi:10.1080/07373937.2015.1057837

Liu RC, Jiang YJ, Li B, Yu LY (2016) Estimating permeability of porous media based on modified Hagen-Poiseuille flow in tortuous capillaries with variable lengths Microfluid Nanofluid 20 doi:Artn 120
10.1007/S10404-016-1783-5

Liukkonen A (1997) Contact angle of water on paper components: Sessile drops versus environmental scanning electron microscope measurements Scanning 19:411-415

Lockington DA, Parlange JY, Lenkopane M (2007) Capillary absorption in porous sheets and surfaces subject to evaporation Transport Porous Med 68:29-36 doi:10.1007/s11242-006-9056-5

Lundblad A, Bergman B (1997) Determination of contact angle in porous molten-carbonate fuel-cell electrodes J Electrochem Soc 144:984-987 doi:Doi 10.1149/1.1837517

Lutz B, Liang T, Fu E, Ramachandran S, Kauffman P, Yager P (2013) Dissolvable fluidic time delays for programming multi-step assays in instrument-free paper diagnostics Lab Chip 13:2840-2847 doi:10.1039/c3lc50178g

Mantanis GI, Young RA, Rowell RM (1995) Swelling of Compressed Cellulose Fiber Webs in Organic Liquids Cellulose 2:1-22

Marmur A (1992) Penetration and Displacement in Capillary Systems of Limited Size Adv Colloid Interfac 39:13-33 doi:Doi 10.1016/0001-8686(92)80053-Z

Martic G, Gentner F, Seveno D, Coulon D, De Coninck J, Blake TD (2002) A molecular dynamics simulation of capillary imbibition Langmuir : the ACS journal of surfaces and colloids 18:7971-7976 doi:10.1021/la020068n

Martic G, Gentner F, Seveno D, De Coninck J, Blake TD (2004) The possibility of different time scales in the dynamics of pore imbibition J Colloid Interf Sci 270:171-179 doi:10.1016/j.jcis.2003.08.046

Martinez AW, Phillips ST, Butte MJ, Whitesides GM (2007) Patterned paper as a platform for inexpensive, low-volume, portable bioassays Angew Chem Int Edit 46:1318-1320 doi:Doi 10.1002/Anie.200603817

Martinez AW, Phillips ST, Wiley BJ, Gupta M, Whitesides GM (2008) FLASH: A rapid method for prototyping paper-based microfluidic devices Lab Chip 8:2146-2150 doi:10.1039/b811135a

Marulier C, Dumont PJJ, Orgeas L, Caillerie D, du Roscoat SR (2012) Towards 3D analysis of pulp fibre networks at the fibre and bond levels Nord Pulp Pap Res J 27:245-255 doi:10.3183/Npprj-2012-27-02-P245-255

Masoodi R, Pillai KM (2010) Darcy's Law-Based Model for Wicking in Paper-Like Swelling Porous Media Aiche J 56:2257-2267 doi:Doi 10.1002/Aic.12163

Masoodi R, Pillai KM (2012) Wicking in porous materials : traditional and modern modeling approaches. CRC Press, Masoodi R, Pillai KM, Varanasi PP (2007) Darcy's law-based models for liquid absorption in polymer wicks Aiche J 53:2769-2782 doi:10.1002/aic.11322

Masoodi R, Tan H, Pillai KM (2011) Darcy's Law-Based Numerical Simulation for Modeling 3D Liquid Absorption into Porous Wicks Aiche J 57:1132-1143 doi:10.1002/aic.12343

Mendez S et al. (2010) Imbibition in Porous Membranes of Complex Shape: Quasi-stationary Flow in Thin Rectangular Segments Langmuir : the ACS journal of surfaces and colloids 26:1380-1385 doi:Doi 10.1021/La902470b

Mitchell J, Webber JBW, Strange JH (2008) Nuclear magnetic resonance cryoporometry Phys Rep 461:1-36 doi:10.1016/j.physrep.2008.02.001

Modaressi H, Garnier G (2002) Mechanism of wetting and absorption or water droplets on sized paper: Effects of chemical and physical heterogeneity Langmuir : the ACS journal of surfaces and colloids 18:642-649 doi:10.1021/la0104931

Moon RJ, Martini A, Nairn J, Simonsen J, Youngblood J (2011) Cellulose nanomaterials review: structure, properties and nanocomposites Chem Soc Rev 40:3941-3994 doi:Doi 10.1039/C0cs00108b

Nabovati A, Llewellin EW, Sousa ACM (2009) A general model for the permeability of fibrous porous media based on fluid flow simulations using the lattice Boltzmann method Compos Part a-Appl S 40:860-869 doi:10.1016/j.compositesa.2009.04.009

Nilsson L, Stenstrom S (1997) A study of the permeability of pulp and paper Int J Multiphas Flow 23:131-153 doi:Doi 10.1016/S0301-9322(96)00064-X

Noh H, Phillips ST (2010) Fluidic Timers for Time-Dependent, Point-of-Care Assays on Paper Anal Chem 82:8071-8078 doi:10.1021/ac1005537

Park J, Shin JH, Park JK (2016) Experimental Analysis of Porosity and Permeability in Pressed Paper Micromachines-Basel 7 doi:10.3390/mi7030048

Perfect E, Kay BD (1991) Fractal Theory Applied to Soil Aggregation Soil Sci Soc Am J 55:1552-1558

Qi D, Uesaka T (1996) Numerical experiments on paper-fluid interaction - Permeability of a three-dimensional anisotropic fibre network J Mater Sci 31:4865-4870 doi:Doi 10.1007/Bf00355874

Renault C, Li X, Fosdick SE, Crooks RM (2013) Hollow-channel paper analytical devices Anal Chem 85:7976-7979 doi:10.1021/ac401786h

Richards LA (1931) Capillary conduction of liquids through porous mediums Physics-J Gen Appl P 1:318-333 doi:Doi 10.1063/1.1745010

Rideal EK (1922) On the flow of liquids under capillary pressure Philos Mag 44:1152-1159

Ridgway CJ, Gane PAC, Schoelkopf J (2002) Effect of capillary element aspect ratio on the dynamic imbibition within porous networks J Colloid Interf Sci 252:373-382 doi:10.1006/jcis.2002.8468

Ruoff AL, Stewart GH, Shin HK, Giddings JC (1960) Diffusion of liquids in unsaturated paper Kolloid-Zeitschrift 173:14 doi:10.1007/BF01513622

Sahimi M (1993) Flow Phenomena in Rocks - from Continuum Models to Fractals, Percolation, Cellular-Automata, and Simulated Annealing Rev Mod Phys 65:1393-1534 doi:DOI 10.1103/RevModPhys.65.1393

Sauret A, Boulogne F, Soh B, Dressaire E, Stone HA (2015) Wetting morphologies on randomly oriented fibers Eur Phys J E 38 doi:Artn 62 10.1140/Epje/I2015-15062-Y

Schilling KM, Lepore AL, Kurian JA, Martinez AW (2012) Fully Enclosed Microfluidic Paper-Based Analytical Devices Anal Chem 84:1579-1585 doi:10.1021/ac202837s

Schuchardt DR, Berg JC (1991) Liquid Transport in Composite Cellulose-Superabsorbent Fiber Networks Wood Fiber Sci 23:342-357

Shou DH, Ye L, Fan JT, Fu KK (2014) Optimal Design of Porous Structures for the Fastest Liquid Absorption Langmuir : the ACS journal of surfaces and colloids 30:149-155 doi:10.1021/la4034063

Spiegelman M (1993) Flow in Deformable Porous-Media .1. Simple Analysis J Fluid Mech 247:17-38 doi:Doi 10.1017/S0022112093000369

Strange JH, Rahman M, Smith EG (1993) Characterization of Porous Solids by Nmr Phys Rev Lett 71:3589-3591 doi:DOI 10.1103/PhysRevLett.71.3589

Szekely J, Neumann AW, Chuang YK (1971) Rate of Capillary Penetration and Applicability of Washburn Equation J Colloid Interf Sci 35:273-+ doi:Doi 10.1016/0021-9797(71)90120-2

Thompson KE (2002) Pore-scale modeling of fluid transport in disordered fibrous materials Aiche J 48:1369-1389 doi:DOI 10.1002/aic.690480703

Tian T, Li JX, Song YL, Zhou LJ, Zhu Z, Yang CYJ (2016) Distance-based microfluidic quantitative detection methods for point-of-care testing Lab Chip 16:1139-1151 doi:10.1039/c5lc01562f

Toley BJ, McKenzie B, Liang T, Buser JR, Yager P, Fu E (2013) Tunable-Delay Shunts for Paper Microfluidic Devices Anal Chem 85:11545-11552 doi:Doi 10.1021/Ac4030939

Topgaard D, Soderman O (2001) Diffusion of water absorbed in cellulose fibers studied with H-1-NMR Langmuir : the ACS journal of surfaces and colloids 17:2694-2702 doi:Doi 10.1021/La000982l

VanderWesthuizen J, DuPlessis JP (1996) An attempt to quantify fibre bed permeability utilizing the phase average Navier-Stokes equation Compos Part a-Appl S 27:263-269 doi:Doi 10.1016/1359-835x(95)00039-5

Wang XH, Liu ZF, Wu QS, Li B (2002) Statistical properties for two-dimensional fluid flow in percolation porous media Physica A 311:320-326 doi:Pii S0378-4371(02)00838-5
Doi 10.1016/S0378-4371(02)00838-5

Weng CH, Chen MY, Shen CH, Yang RJ (2014) Colored wax-printed timers for two-dimensional and three-dimensional assays on paper-based devices Biomicrofluidics 8 doi:Artn 066502
10.1063/1.4902246

Wheatcraft SW, Tyler SW (1988) An Explanation of Scale-Dependent Dispersivity in Heterogeneous Aquifers Using Concepts of Fractal Geometry Water Resour Res 24:566-578 doi:Doi 10.1029/Wr024i004p00566

Wiklund H, Uesaka T (2012) Edge-wicking: Micro-fluidics of two-dimensional liquid penetration into porous structures Nord Pulp Pap Res J 27:403-408 doi:10.3183/Npprj-2012-27-02-P403-408

WitkowskaNery E, Santhiago M, Kubota LT (2016) Flow in a Paper-based Bioactive Channel – Study on Electrochemical Detection of Glucose and Uric Acid Electroanalysis 28:2245-2252 doi:10.1002/elan.201600210

Wyllie MRJ, Gregory AR (1955) Fluid Flow through Unconsolidated Porous Aggregates - Effect of Porosity and Particle Shape on Kozeny-Carman Constants Ind Eng Chem 47:1379-1388 doi:Doi 10.1021/Ie50547a037

Xia YY, Si J, Li ZY (2016) Fabrication techniques for microfluidic paper-based analytical devices and their applications for biological testing: A review Biosensors & bioelectronics 77:774-789 doi:10.1016/j.bios.2015.10.032

Xu P, Yu BM (2008) Developing a new form of permeability and Kozeny-Carman constant for homogeneous porous media by means of fractal geometry Adv Water Resour 31:74-81 doi:10.1016/j.advwatres.2007.06.003

Yetisen AK, Akram MS, Lowe CR (2013) Paper-based microfluidic point-of-care diagnostic devices Lab Chip 13:2210-2251 doi:10.1039/c3lc50169h

Yu BM, Cheng P (2002) A fractal permeability model for bi-dispersed porous media Int J Heat Mass Tran 45:2983-2993 doi:Pii S0017-9310(02)00014-5
Doi 10.1016/S0017-9310(02)00014-5

Yu BM, Lee LJ (2002) A fractal in-plane permeability model for fabrics Polym Composite 23:201-221 doi:Doi 10.1002/Pc.10426

Zhmud BV, Tiberg F, Hallstensson K (2000) Dynamics of capillary rise J Colloid Interf Sci 228:263-269 doi:DOI 10.1006/jcis.2000.6951

Zhong ZW, Wang ZP, Huang GXD (2012) Investigation of wax and paper materials for the fabrication of paper-based microfluidic devices Microsyst Technol 18:649-659 doi:10.1007/s00542-012-1469-1

3. CHARACTERIZING EFFECTS OF HUMIDITY AND CHANNEL SIZE ON IMBIBITION IN PAPER-BASED MICROFLUIDIC CHANNELS

3.1. Introduction

Paper-based microfluidics has generated a great amount of interest for the development of diagnostic and self-contained analytical devices. Applications range from healthcare, food safety, environmental monitoring, among others. What has in part attracted attention is the low-cost, ease-of-use, and adaptability of these paper devices. Compared to conventional microfluidic devices, the paper-based counterparts are able to utilize paper's inherent wicking property to eliminate the external pumping needed to drive the fluid. Channels are easily formed by either selectively removing sections of the paper substrate or by pattering channel boundaries with a hydrophobic material. The former methods ranges from using high precision CO_2 laser-cutting (Chitnis et al. 2011; Fu et al. 2010) to craft cutting (Fenton et al. 2009) while the latter methods range from those of photolithography (Martinez et al. 2008b) to techniques using commercially available printers with inkjet (Abe et al. 2010) or solid ink (Carrilho et al. 2009) technology. Ultimately, the common result of these fabrication methods is the creation of a defined impermeable boundary for fluid transport. Thorough reviews on fabrication methods have recently been published (Jiang and Fan 2016; Xia et al. 2016; Yetisen et al. 2013). In spite of the benefits and advantages described above, paper-based microfluidic technologies often lack the necessary sensitivity and sophistication available in conventional microfluidic devices. In order to be a competitive alternative, paper-based microfluidics require improvement and novel development of feasible detection methods. These methods will likely require increasingly complex chemistry and control of reagents. Thus, obtaining precise, accurate, and consistent fluid handling within the paper device will be crucial.

Currently, the most widely used imbibition model in the paper-based microfluidic community is the Lucas-Washburn (L-W) equation (Lucas 1918; Washburn 1921) where the progression of the imbibition front is taken to be proportional to the square-root of time. More extensive theoretical models for imbibition as well as fluid front concentration gradients in analyte transport (Berli and Kler 2016) are available from the porous media research community. These imbibition models include models derived from diffusion dynamics (Richards 1931), models that include fluctuations created by the roughness of the material (Krug and Meakin 1991), and models based on statistical methods (Kardar et al. 1986), among others (Alava et al. 2004). These models are valuable and used to understand the detailed dynamics occurring within and during the imbibition process. However, practical implementation of these models under the context of paper-based microfluidic devices is lacking mainly due to the extensive empirical model parameters required to reproduce the highly dynamic imbibition phenomena. Consequently, the L-W model is still widely used by the paper-based microfluidic community due to its simplicity, ease-of-use, and adequate accuracy for the current characterization needs. The L-W equation has been used to compare superabsorbent material to lab grade filter paper (Schuchardt and Berg 1991), used to design simple sequential delivery devices (Fridley et al. 2014; Fu et al. 2010; Lutz et al. 2013), and to characterize wettability of modified paper (Bohm et al. 2014; Li et al. 2010; Lutz et al. 2013). Even though the L-W equation is arguably the standard in paper-based microfluidics, for the field to continue advancing toward more sophisticated and precise device functions, it is imperative that better knowledge in and tools for characterization of the liquid imbibition be available to researchers.

One of the primary applications of paper-based microfluidics is analyte detection. Various flow control methods have been investigated in order to provide the necessary fluid handling for the varying degree of detection processes. These processes can range from simple glucose detection (Martinez et al. 2007) or signal amplification (Fu et al. 2010) to more complex processes where sequential and timed handling of the fluid sample and reagents are required such as with enzyme-linked immunosorbent assay (ELISA) (Apilux et al. 2013) and with “paper machines” where fluid handling is integrated with loop-mediated isothermal amplification (LAMP) (Connelly et al. 2015). Methods to control imbibition include changing the channel geometry and the physical properties of the paper. Several groups have investigated and proposed several cross-section geometries. The Yager group investigated the wet-out and fully wetted flows in 2-D channel networks (Fu et al. 2011; Kauffman et al. 2010), Mendez et al. (2010) studied fan-shaped expansion channels that can induce quasi-steady-state flows in the preceding straight channel section, Shou et al. (2014) investigated contraction/expansion segments along the channel, and Elizalde et al. (2015) proposed a general expression for continuous cross-sectional change in geometry as a way to control fluid flow. In addition to geometrical manipulation of the paper channel, modifying and adjusting the permeability of the paper have also been shown to be effective. These methods, among others include using hydrophobic polymers (Bohm et al. 2014; Noh and Phillips 2010; Weng et al. 2014), using dissolvable and erodible barriers (Jahanshahi-Anbuhi et al. 2014; Lutz et al. 2013), as well as physical methods such as compressing paper (Park et al. 2016) and selectively cutting the paper (Giokas et al. 2014; Renault et al. 2013). Although considerable knowledge exists on techniques to manipulate fluid within the paper channel, what is lacking are studies on how non-laboratory conditions (e.g. relative humidity) influence fluid flow.

The present study aims to address this gap. In particular, we focus on the effects of relative humidity and channel width. We report a series of controlled imbibition experiments using cellulose papers commonly used in the field of paper-based microfluidics. We show that both the imposed relative humidity and the channel width have critical design considerations in paper-based devices. Additionally, we compare three models, the L-W model, the Fries et al. (2008) model which incorporates evaporation, and a newly developed water saturation model. We assess their accuracy in representing the experimental data and systematically evaluate the importance of evaporation and water saturation under a wide range of relative humidity conditions.

3.2. Materials and methods

3.2.1. Material and device fabrication

Four different paper types were surveyed in this study: Whatman qualitative filter paper of Grade #1, Grade #4, Grade #5, and Whatman chromatography (Chr) paper of Grade 1 (GE Healthcare, Pittsburgh, PA). Based on the distance wicked over time, the paper types can be classified into three qualitative imbibition speeds (slow, medium, and fast). The test device and the specified paper pieces' dimensions were designed in SolidWorks (Dassault Systèmes, Vélizy-Villacoublay, France) and cut using a Zing 16 CO_2 laser cutter (Epilog Laser, Golden, CO). All wetting and imbibition experiments were conducted using ultrapure water (18.2 MΩ-cm) prepared by a Millipore Synergy UV water purification system (Billerica, MA). Relevant properties of the surveyed papers are summarized in Table 3.1. An ambient temperature of 25 ± 0.5°C was maintained throughout the experiments in this study.

Table 3.1 Properties of the surveyed paper types in the current study. * See Appendix A for more information.

Paper type (speed)	**Density of cellulose fiber, ρ_c**	**Thickness, T**	**Basis Weight*, W_B**	**Porosity* , Φ**
Whatman #1 (Medium)	1,500-1,600 kg/m^3 (Bledzki and Gassan 1999; Moon et al. 2011)	180 μm	81.71 g/m^2	0.707
Whatman #4 (Fast)		205 μm	83.96 g/m^2	0.736
Whatman #5 (Slow)		200 μm	92.35 g/m^2	0.702
Whatman Chr-1 (Medium)		180 μm	81.98 g/m^2	0.706

3.2.2. Characterization of evaporation flux

Evaporation flux was experimentally measured in two ways as described below: evaporation from a fixed pre-wetted area (static evaporation) and evaporation from a dynamically wetted area (dynamic evaporation).

In the static evaporation experiment, a 40 x 40 mm laser-cut piece of paper was hung on an analytical scale (Model TP-64, Denver Instrument, Bohemia, NY) placed inside an environmentally controlled chamber (Model 5503-E, Electro-Tech Systems, Glenside, PA). Preliminary studies showed that the lowest possible relative humidity that was able to be maintained during the imbibition process was 18%. The chamber was set to a specified relative humidity value (18, 25, 50, 75, 90, or 99%) and left for an hour to allow the paper piece to reach equilibrium with the chamber environment. The paper was then wetted by evenly applying water using a micropipette. 0.25 mL of water fully wetted the sample without visible excess water accumulating at the edges. The mass of the paper was recorded as water evaporated over 30 minutes while relative humidity was maintained at the designated value. This experiment was repeated 5 times for each relative humidity value and each paper type. The rate of evaporated water mass was divided by the total surface area of the paper piece to calculate the evaporation flux, *F*.

In the dynamic evaporation experiment, the evaporation rate was measured from a laser-cut piece of paper (50 x 150 mm) undergoing the imbibition process on top of an analytical scale. The relative humidity was set to 25, 50, and 75%. The evaporation flux was calculated using the rate of water evaporation from the piece of paper and the changing surface area of the wetted region. Similarly to the static evaporating experiments, measurements were repeated 5 times for each relative humidity value and each paper type.

3.2.3. Characterization of residual water

A 70 x 70 mm laser-cut piece of paper was put in an open glass container and dried at 105°C for one hour in a convection oven (Model FD-53, Binder, Bohemia, NY). The glass container was then immediately sealed with a dry lid and transferred to the environmentally controlled chamber. Once the chamber reached its lowest possible relative humidity value (3%), the paper sample was taken out and immediately placed on the analytical scale to measure its dry mass. The paper strip was then hung on the scale and left for an hour at a specified relative humidity value (10, 18, 25, 50, 75, 90, or 99%) to reach equilibrium before its mass was measured and recorded. Ten replicates were tested for each relative humidity value and each paper type. Based on the dry mass of paper, the amount of water retained (i.e., volume fraction of residual water) in the unwet paper, here called water saturation S_w, was calculated for each relative humidity. See Appendix C for more information.

3.2.4. Measurement of imbibition distance

The paper device was mounted vertically on the test fixture inside the environmentally controlled chamber (Fig. 3.1a-b). As shown in Fig. 3.1c, each device features 41 mm long channels of 1 mm, 2 mm, 4 mm, 10 mm, and 20 mm widths. A water reservoir was placed on a laboratory jack (Model L-490, Thorlabs, Newton, NJ). The jack's platform was then raised quickly to the start line of the channels. The imbibition process was recorded using a Nikon D5100 digital camera (Tokyo, Japan). Image frames were then extracted from the recorded video files using Adobe Premiere Pro CS6 (San Jose, CA). Image brightness was adjusted digitally to increase the contrast of the imbibition front. Imbibition distance was then measured at the centerline position of the liquid front using ImageJ with the Manual Tracking plug-in. Ten replicates were tested for each combination. The combinations include variations in channel width (1, 2, 4, 10, 20 mm), relative humidity (18, 25, 50, 75, 90 and 99%) and paper type (Whatman #1, #4, #5, and Chr-1).

3.2.5. Calculation of effective permeability

A custom MATLAB script was written and used to calculate effective permeabilities, K, of the L-W model, the Fries et al. model, and the water saturation model by curve fitting against the experimentally obtained imbibition data. The effective permeability value was chosen based on the highest R^2 value.

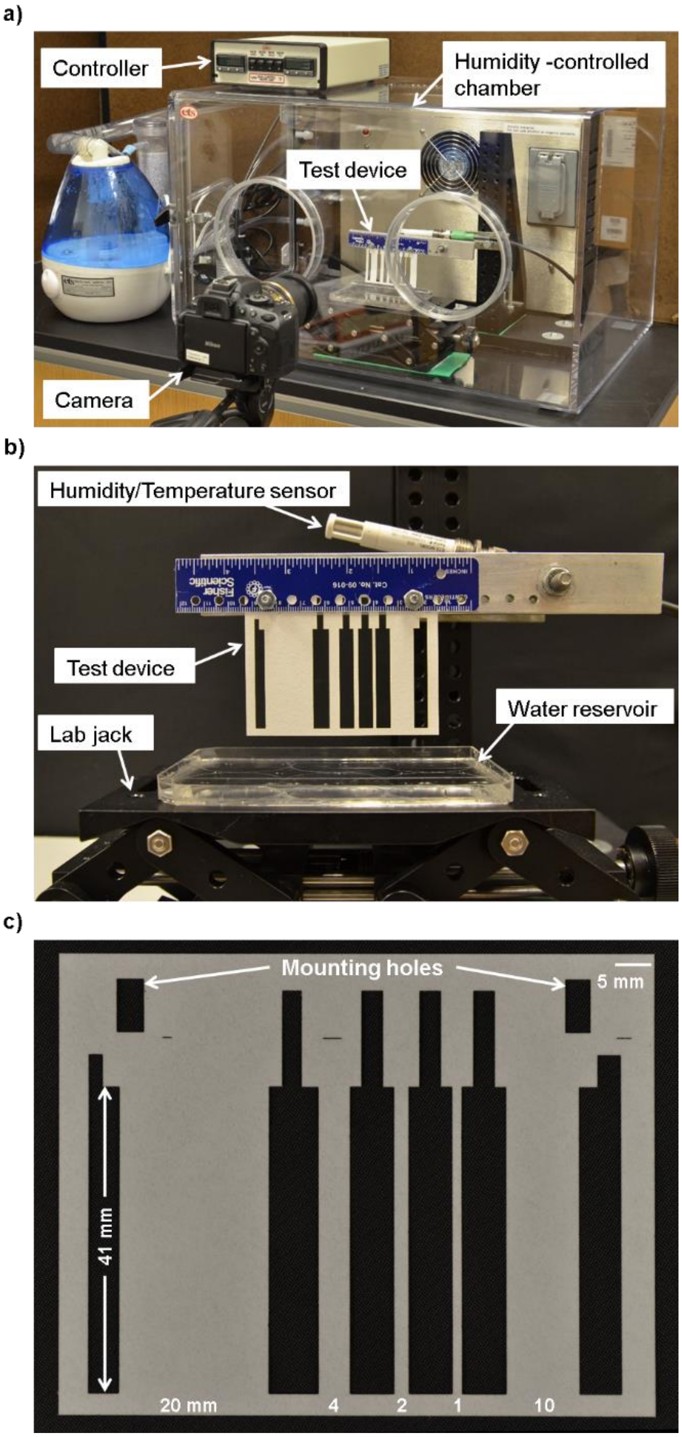

Fig. 3.1 Test set-up for imbibition experiments. a) Overview of test set-up. A pair of gloves (not shown) were attached to the glove ports and used during the experiments to access the sample and the laboratory jack. b) Close-up view of the testing section. c) An unmounted paper device featuring 5 channels of 1, 2, 4, 10, and 20 mm width.

3.3. Results and discussion

3.3.1. Imbibition studies

An array of imbibition studies was conducted to explore a wide range of imbibition scenarios. These scenarios included combinations of five different channel widths (1, 2, 4, 10, and 20 mm), four commonly used paper types (Whatman #1, #4, #5, and Chr-1), and six different relative humidity values (18, 25, 50, 75, 90, and 99%). Fig. 3.2 shows imbibition distance vs. time for different channel widths at selected relative humidity values for each surveyed paper (complete set available in Appendix E Fig. E.2-E.5).

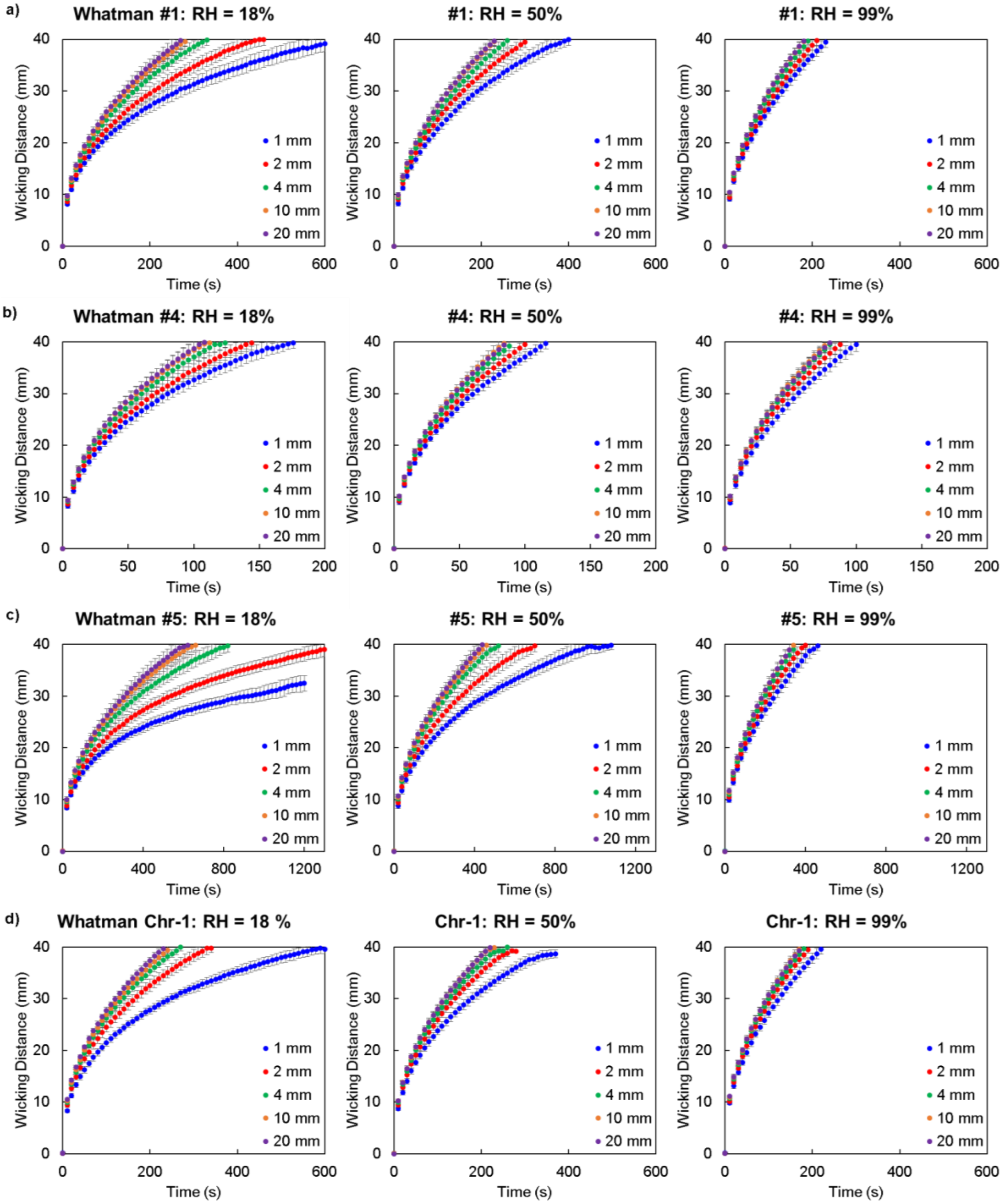

Fig. 3.2 Imbibition distance vs. time of surveyed paper types at selected relative humidity: a) Whatman #1, b) Whatman #4, c) Whatman #5, and d) Whatman Chr-1. Channel width tested: 1, 2, 4, 10, and 20 mm. Data shown as mean ± SD (N = 10).

Within each paper type, two relations were consistently observed. First, the imbibition distance at a specified time increased as relative humidity increased. This phenomenon is visible at about 15 mm and becomes clear as the channel length increases. For example, to reach a height of 40 mm with a 2 mm wide channel the relative humidity can delay the liquid front by as much as 60-800 seconds depending on the type (speed) of the Whatman paper. This demonstrates the strong inhibitory effect of low relative humidity on liquid imbibition. The second observed relation corresponds to the channel width. For a specified relative humidity, the liquid front travels less distance for narrow channels after an elapsed time and becomes less pronounced as the channel width increases. This phenomenon becomes visible at about 20 mm and becomes clear as the channel length increases. This channel width effect decreases as the relative humidity increases. The channel width dependence on imbibition has previously been observed in channels with hydrophobic boundaries. The inhibitory effect is suggested to be caused when the fiber length is larger than the width of the channel, terminating the flow at the side edges of the channel (known as dead-end pores) (Bohm et al. 2014) or caused by the increase in contact angle seen at the wall (Hong and Kim 2015). Nonetheless, a narrow channel has an increased resistance, with an asymptotic plateau for wider channels. Interestingly, the dependence in both relative humidity and channel width are more pronounced in slower wicking papers.

3.3.2. Imbibition modeling

A detailed description of imbibition becomes increasingly complicated as the parameters involved are frequently time and length-scale dependent. These parameters, among others, include properties involving pore size, porosity, tortuosity, contact angle, the degree of swelling, and roughening terms describing perturbations of liquid front. Extensive studies have been done to understand the underlining imbibition dynamics, and sophisticated models have been derived from diffusion theory (Richards 1931), stochastic theory (Kardar et al. 1986), and percolation theory (Amaral et al. 1995). However, the shared trait among these advanced models is the large number of parameters and theoretical constants needed, often requiring fit to the specific situation to be addressed. Even analytically friendly models incorporating swelling are case specific and swelling parameters need fitting to the experimental data (Masoodi and Pillai 2010). For practical characterization and usage in the paper-based microfluidics filed, more user-friendly models are preferred.

The current standard for paper-based microfluidic modeling is the L-W model (Eq. 3.1), a simple imbibition model derived by combining capillary theory with Hagen-Poiseuille flow. (Lucas 1918; Washburn 1921). Though known to be theoretically inaccurate in describing the imbibition flow (Alava et al. 2004), the L-W equation is frequently used as a first order approximation due to the very good empirical description of the liquid front and the ease-of-use. The liquid front is described by,

$$y_f = \sqrt{\frac{D_e \gamma \cos\theta}{4\mu} t} \tag{3.1}$$

where, y_f is the imbibition distance of the liquid front, D_e is the effective capillary diameter, γ is the surface tension of the liquid, θ is the capillary contact angle, μ is the dynamic viscosity, and t is the imbibition time. Since the L-W model is only dependent on effective material pore and the liquid properties, it predicts that any channel width will have the same imbibition behavior. However, the simple characterization attributes associated with the L-W equation can be invalidated in non-ideal laboratory settings, such as imbibition in different relative humidity. This specific issue raises questions and concerns about relative humidity effects such as evaporation and water saturation. Therefore, there is a need in the paper-based microfluidic field to characterize such possible effects in a straight forward manner and with approachability.

To characterize the imbibition front of all surveyed combinations and to assess the importance of relative humidity, we compare three models, the L-W model, the Fries et al. (2008) model which incorporates evaporation, and a newly developed water saturation model, where evaporation and residual water are incorporated.

The Fries et al. model stems from the need of an evaporation based model. Originally derived for metal weaves, the Fries et al. model results in a relatively simple, straight forward imbibition equation that takes evaporation into account.

$$y_f = \left[\frac{a - a\exp(-2bt)}{b} \right]^{\frac{1}{2}}$$

$$a = \frac{K\gamma\cos\theta}{D_e\phi\mu}, b = \frac{F(W+T)}{\phi\rho WT} \tag{3.2}$$

where, D_e is the effective pore diameter, K is the effective permeability, ϕ is the porosity of the material, F is the evaporation flux, ρ is the liquid density, W is the channel width, and T is the paper thickness.

Paper, unlike metal weaves, is hygroscopic by nature, and will absorb moisture at high relative humidity. Accounting for this, we developed a model that includes residual water associated with the relative humidity. The resulting model (see Appendix F for derivation) is a modified version of the Fries et al. model accounting for the internal volume changes due to the residual water. With gravitational effects being negligible, the implicit model simplifies to Eq. 3.3, here on called the water saturation model,

$$y_f = \left[\frac{a - a\exp(-2bt)}{b}\right]^{\frac{1}{2}}$$

$$a = \left(\frac{K}{2\phi}\right)^{1/2} \frac{\gamma\cos\theta}{\mu}, b = \frac{F(W+T)}{\phi\rho(1-S_w)WT} \quad (3.3)$$

where S_w is the degree of water saturation.

To compare Eq. 3.3 to the L-W model and the Fries et al. model, Hagen-Poiseuille and Darcy flows are related so as to produce an alternative form of the L-W equation,

$$y_f = \sqrt{\left(\left(\frac{2K}{\phi}\right)^{1/2} \frac{\gamma\cos\theta}{\mu} t\right)} \quad (3.4)$$

Similarly, the Fries et al. model becomes,

$$y_f = \left[\frac{a - a\exp(-2bt)}{b} \right]^{\frac{1}{2}} \tag{3.5}$$

$$a = \left(\frac{K}{2\phi} \right)^{1/2} \frac{\gamma \cos\theta}{\mu}, b = \frac{F(W+T)}{\phi\rho WT}$$

It is to be noted that when evaporation is zero ($F = 0$), both Eq. 3.3 and Eq. 3.5 reduce to the L-W model (Eq. 3.4).

3.3.3. Evaporation flux

The evaporation flux, F in both Eq. 3.3 and Eq. 3.5 were modelled as being constant. To determine this value, a static evaporation flux was calculated by measuring the mass of evaporated water over time under different relative humidity and paper type. Fig. B.1 in Appendix B shows the linear relationships between mass evaporation and time among all relative humidity/paper combinations. The linear relationship confirms that at constant relative humidity the rate of evaporation (i.e., slope of the plot divide by area) from a constant area is constant irrespective of the wetness of the paper. The only exception was when the majority of the water is evaporated. The nonlinearity is seen during the last 5 minutes of 18% relative humidity (Fig. B.1). At this instant, the four surveyed papers contained at most 5% of the 0.25 mL water added. This results in an approximate liquid-to-surface-area ratio of 8 nL/mm^2 after 30 minutes at 18% relative humidity. Since the longest imbibition time was approximately 22 minutes (see Fig. 3.2), the linear approximation for 18% relative humidity was assumed. The evaporation flux vs. relative humidity is plotted in Fig. 3.3 with a linear best-fit line for each paper type.

As shown, for all paper types the evaporation flux is an almost identical with a linear decline as the relative humidity increases.

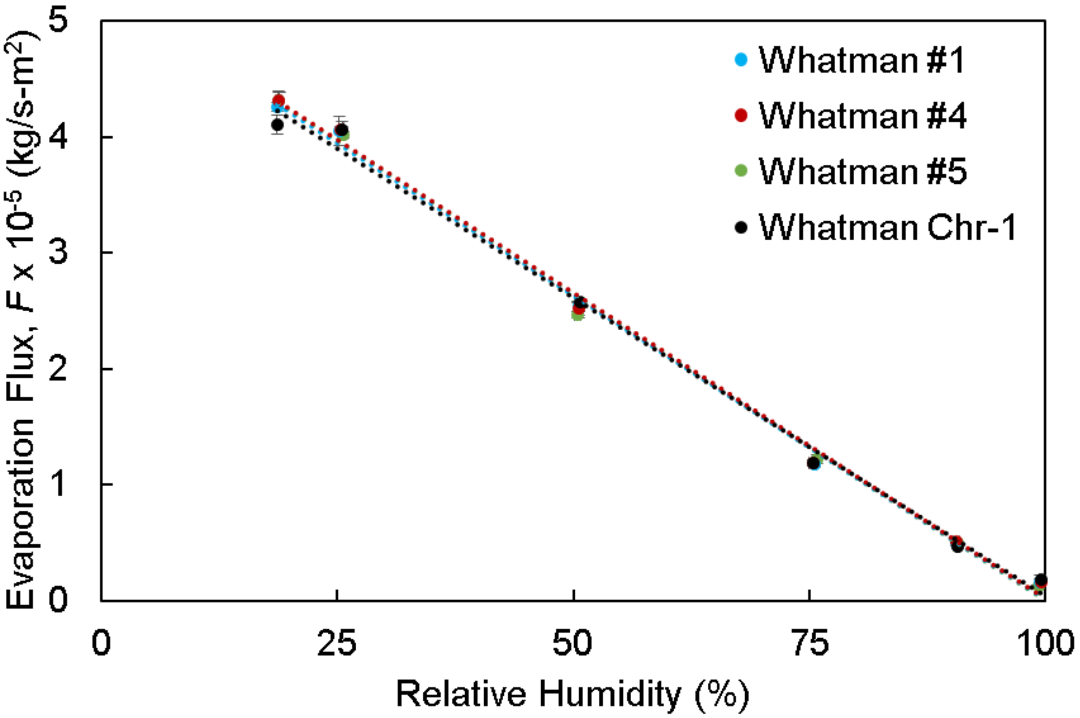

Fig. 3.3 Static evaporation flux vs. relative humidity of surveyed paper types with linear fit (mean R^2 = 0.9965). Data shown as mean ± SD (N = 5).

The assumption of constant evaporation flux in Eq. 3.3 and Eq. 3.5 makes the usage of the models more user-friendly. As the paper undergoes the imbibition process, the continuously increasing wetted area might lead to a dynamic evaporation process. Dynamic evaporation results showed, comparable to the static evaporation, the four surveyed papers exhibited similar evaporation fluxes at each relative humidity (Fig. 3.4). The dynamic behavior was seen more explicitly at the higher relative humidity (i.e., 75%). Interestingly, the evaporation flux approached and reached the static evaporation flux values observed in Fig. 3.3. Because of the relatively fast asymptotic approach of the dynamic evaporation flux to the static value, as well as the decreasing effect of evaporation with higher relative humidity, we concluded that the static flux values represented evaporation during imbibition reasonably well and therefore used in the subsequent imbibition analysis.

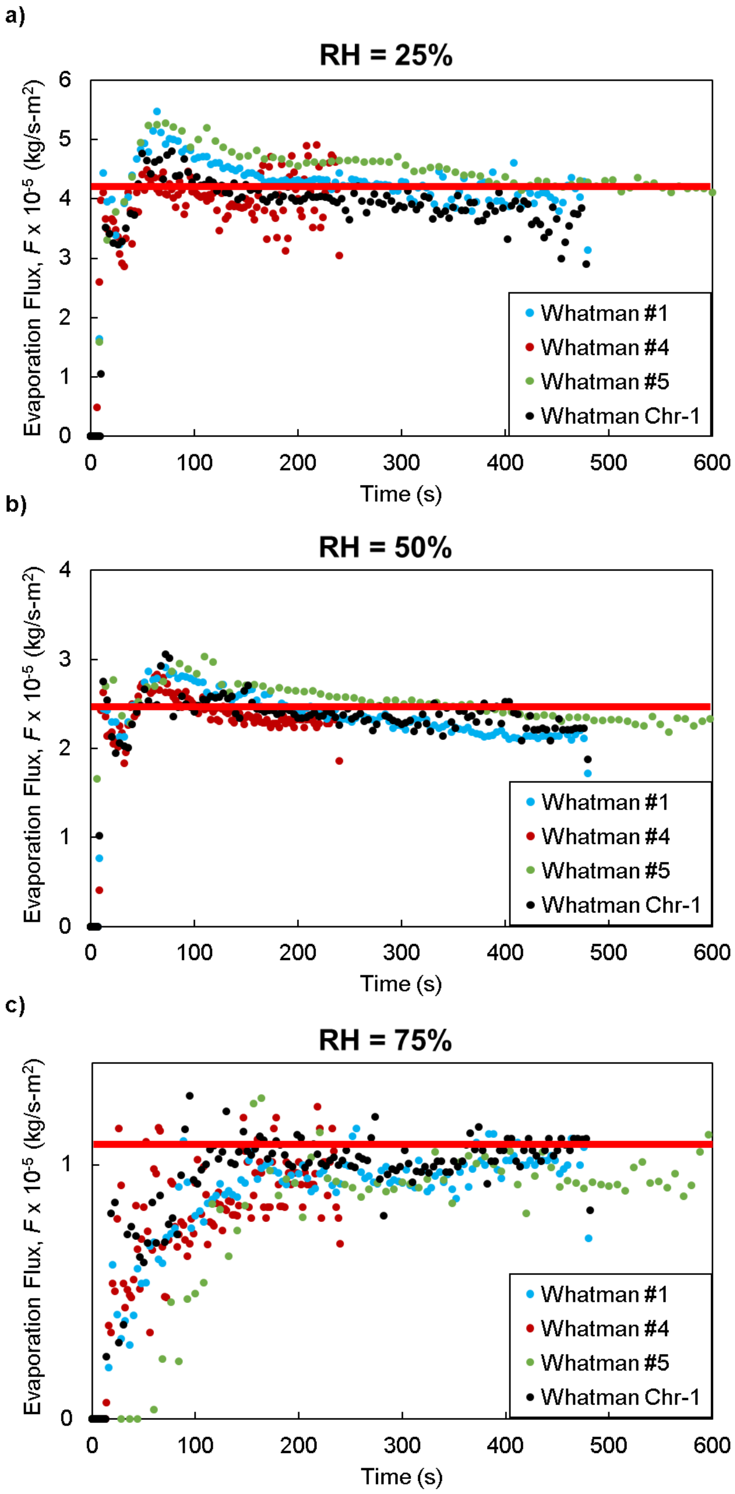

Fig. 3.4 Dynamic evaporation flux of surveyed paper types vs. time. Horizontal line shows the average static evaporation flux value of the four paper types at the specified relative humidity. Data shown as mean (N = 5).

3.3.4. Water saturation

The degree of residual water (i.e., water saturation) at specified relative humidity is particularly important when it comes to paper due to the hygroscopic nature of cellulose. Fig. 3.5 shows the calculated water saturation S_w for each paper type at relative humidity of 10, 18, 25, 50, 75, 90, and 99%. For each relative humidity, water saturation was observed to be similar across the surveyed paper types up to about 50% relative humidity. Above 50%, the Whatman #4 absorbed water noticeably less than the others. This can be due in part to the relatively large pore structure within this specific paper (Appendix D Fig. D.1). Water retention at 99% relative humidity resulted in a maximum water saturation of 7.5% for Whatman #4 and about 9% for the other three paper types.

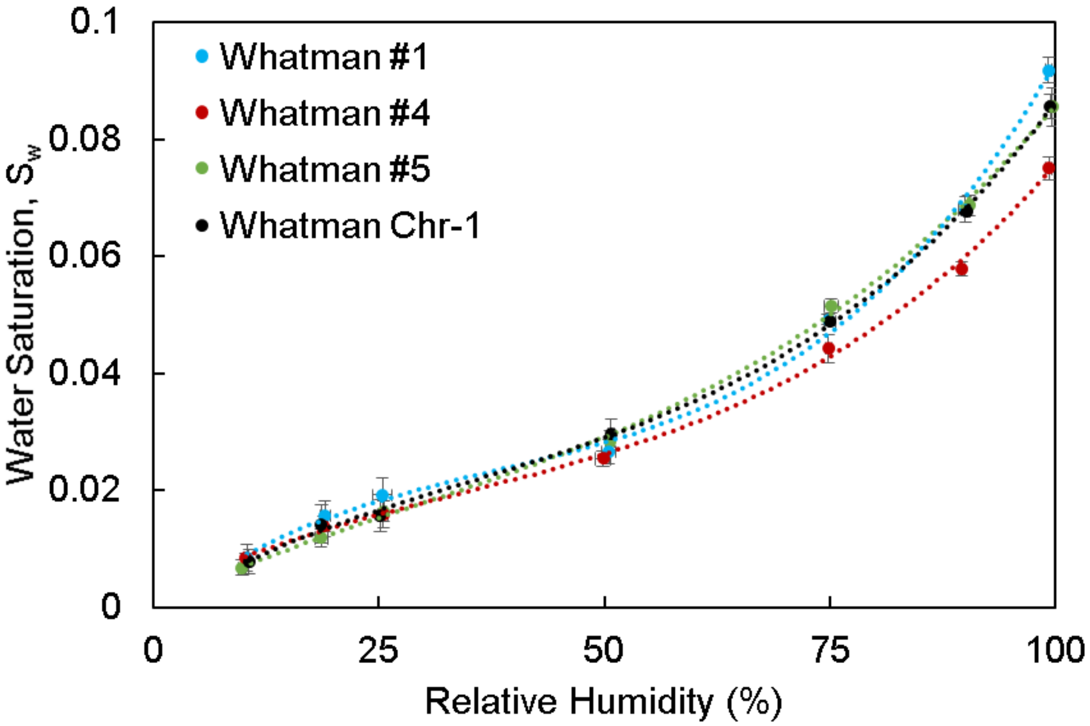

Fig. 3.5 Water saturation vs. relative humidity of surveyed paper types with a cubic fit (mean $R^2 = 0.9986$). Data shown as mean ± SD (N = 10).

3.3.5. Effective permeability and model comparison

The effective permeability, *K,* of the channel was determined as a way to characterize the observed imbibition behavior. The effective permeability for each scenario (channel width, relative humidity, paper type) was extracted by fitting the L-W model (Eq. 3.4), the Fries et al. model (Eq. 3.5) , and the water saturation model (Eq. 3.3) to the imbibition distance vs. time data (see Appendix E for the complete set). It should be noted that the L-W model is inherently independent of channel width and relative humidity but here it was fitted to each scenario. This allowed for a direct comparison of the three models. Because of paper's high affinity to water and the highly dynamic contact angle within the porous media, the water-paper interface was taken as perfectly wetting ($\theta = 0^\circ$) (Ballerini et al. 2011; Liukkonen 1997; Songok et al. 2014).

The resultant effective permeabilities for each paper type were plotted as a function of relative humidity (Fig. 3.6–3.8). Direct comparisons between the models show that the permeabilities are higher with the inclusion of the evaporation term, in particular, at low relative humidity. A linear relationship with a positive constant slope was observed, irrespective of the channel width and model. Additionally, the effective permeability asymptotically approached an upper limit with the increasing channel width. These simple practical relationships that are conserved across different paper types can be used by researchers to design better paper devices. Specifically, by knowing the slope and the intercept in the vertical axis (see Appendix G Table G.1, G.2, and G.3), the imbibition behavior can be easily calculated for a specific paper type, a specific channel width, and a relative humidity value.

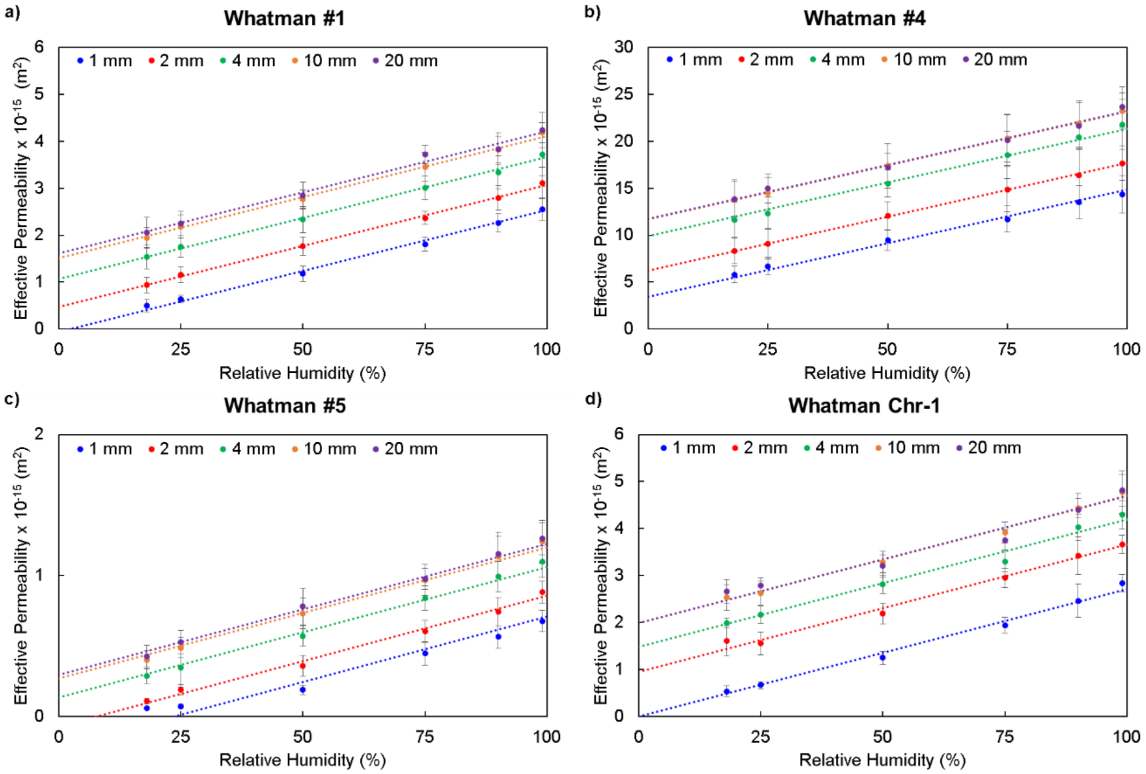

Fig. 3.6 Effective permeability vs. relative humidity of surveyed paper types for the L-W model. a) Whatman #1, b) Whatman #4, c) Whatman #5, and d) Whatman Chr-1. Dotted lines are best-fit lines with a constant slope. Data points shown as mean ± SD (N = 10).

Comparing the effective permeability associated with the L-W model (Fig. 3.6) to either the Fries et al. model (Fig. 3.7) or the water saturation model (Fig. 3.8) shows the importance of evaporation, particularly the high evaporation rate that occurs at low humidity. Without a designated term for evaporation, the effective permeability in the L-W model must account for the slowing of imbibition due to evaporation. Differences in the models become less apparent as the relative humidity increases because of the reduced evaporation. This results in a convergence of the L-W model (Eq. 3.4) and the evaporation models (Eq. 3.3 and Eq. 3.5).

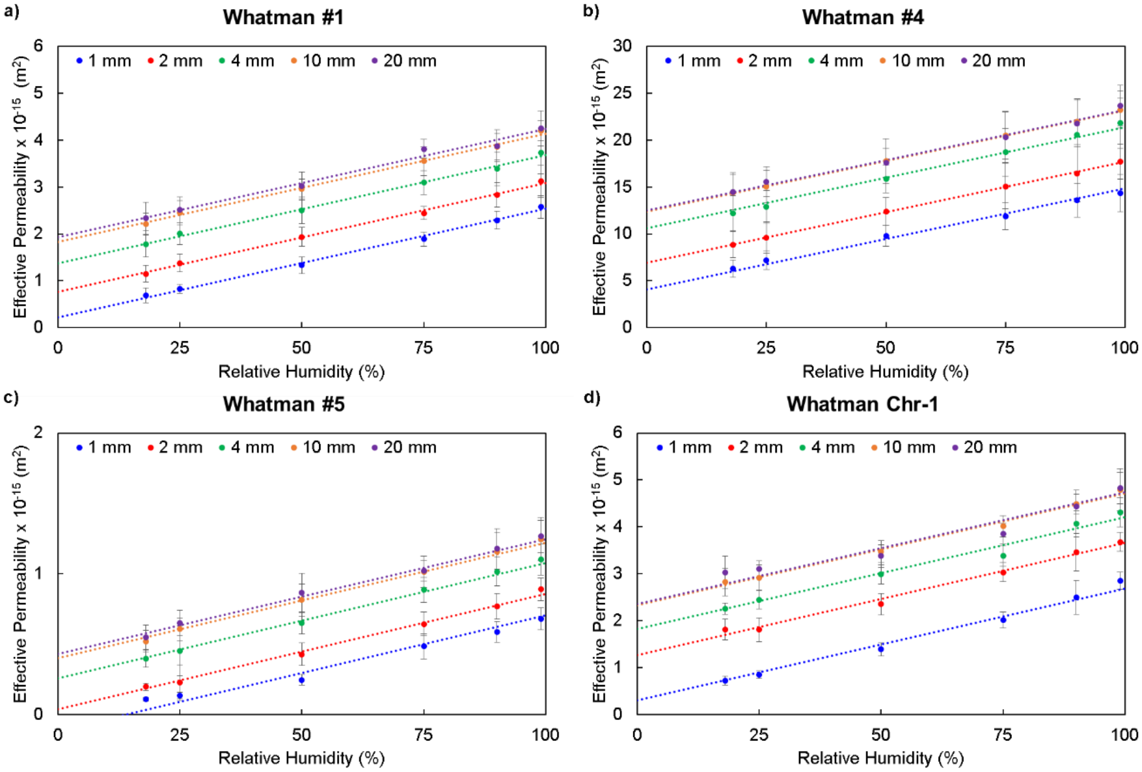

Fig. 3.7 Effective permeability vs. relative humidity of surveyed paper types for the Fries et al. model. a) Whatman #1, b) Whatman #4, c) Whatman #5, and d) Whatman Chr-1. Dotted lines are best-fit lines with a constant slope. Data points shown as mean ± SD (N = 10).

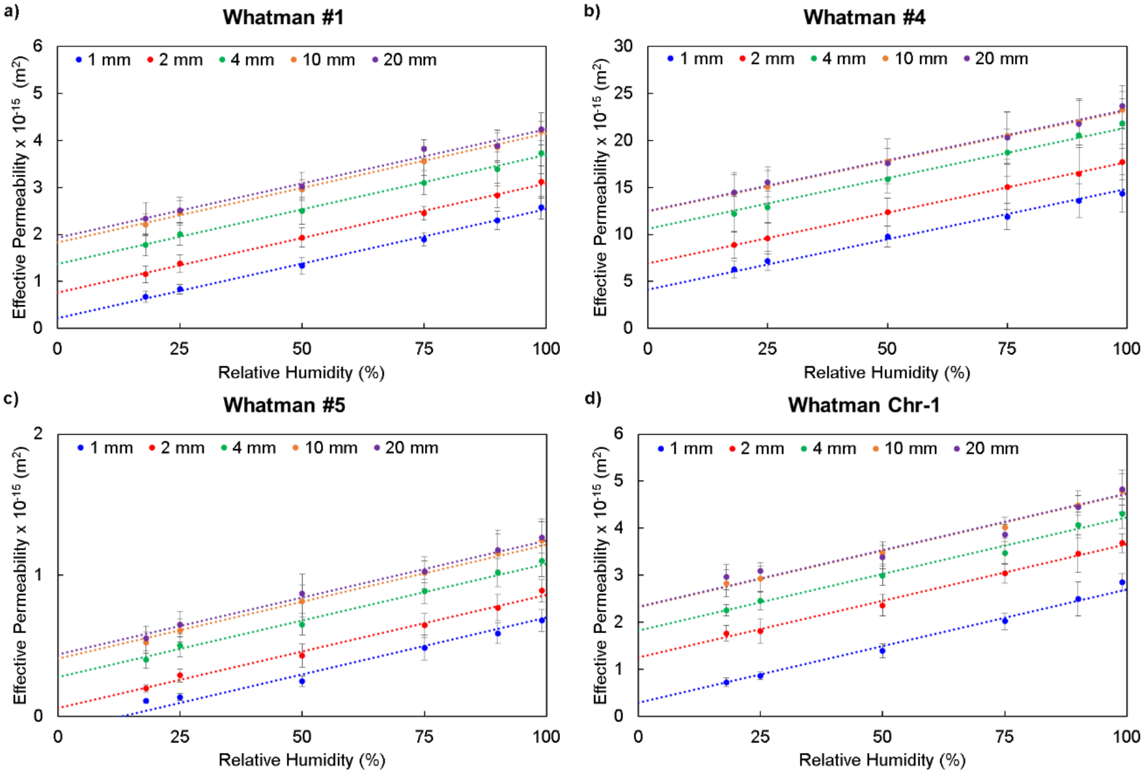

Fig. 3.8 Effective permeability vs. relative humidity of surveyed paper types for the water saturation model. a) Whatman #1, b) Whatman #4, c) Whatman #5, and d) Whatman Chr-1. Dotted lines are best-fit lines with a constant slope. Data points shown as mean ± SD (N = 10).

In comparing the accuracy in these effective permeabilities, the coefficient of determination, R^2, was investigated. Fig. 3.9 shows the R^2 value (note difference in vertical axis) for all the permeabilities associated with the surveyed papers at selected relative humidity (for full set see Appendix H). The relatively low R^2 value at low relative humidity for the L-W model reiterates its limitations associated with evaporation. Interestingly, as the relative imbibition speed of the paper decreases (e.g. slow imbibition in Whatman #5), the accuracy of the evaporation models also decreases with that of the

L-W model being the most prominent, (Fig. 3.9c). On the other hand, the accuracy of these models increases as the channel width increases. Collectively, this comparison shows a critical importance of treating the permeability and hence the effective pore diameter as a function of both relative humidity and channel geometry.

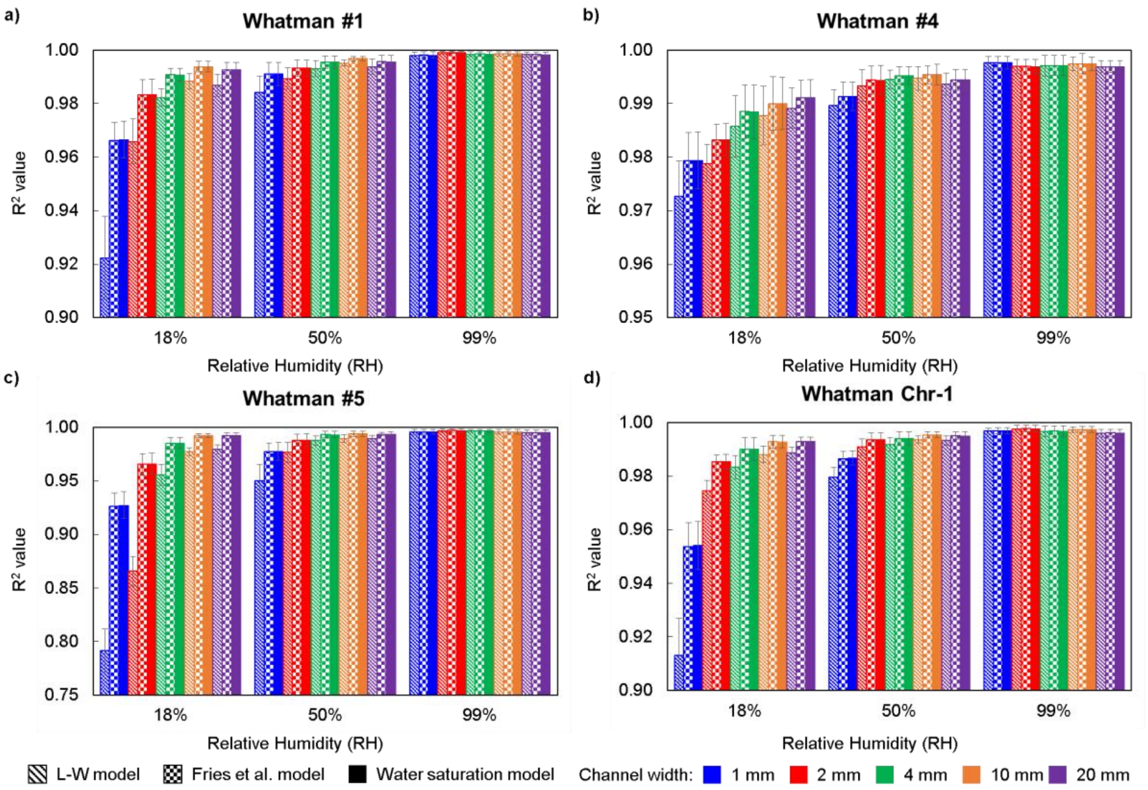

Fig. 3.9 R^2 values of effective permeability of surveyed paper types at selected relative humidity for L-W model, Fries et al. model, and the water saturation model. a) Whatman #1, b) Whatman #4, c) Whatman #5, and d) Whatman Chr-1. Data shown as mean ± SD (N = 10).

In comparing the water saturation model to the Fries et al. model, it is found that the effective permeability values are almost identical. This result can be foreseen by finding the ratio of the evaporation to the water saturation. At high relative humidity, evaporation is low while water saturation is at its highest. At low relative humidity, evaporation is high while water saturation is at its lowest. Irrespective of the case, for these types of paper, the evaporation term dominates over the water saturation at a specified relative humidity. Therefore, for characterization purposes the degree of water saturation is found to be negligible, although water saturation might have a significant impact on other aspects in paper-based microfluidic devices (e.g. morphological changes, moisture sensitive chemistry, device handling, shelf life). These types of investigations are beyond the scope of this study.

3.4. Conclusion

In the current study, we characterized the effect of relative humidity and channel width on imbibition for paper-based microfluidic applications. The significant role of relative humidity on imbibition was demonstrated, as well as the impact of channel width on imbibition. Comparing the L-W model to the evaporation models showed the ineffectiveness of the former in accurately describing flows at low relative humidity. In addition, comparison of the water saturation model to the Fries et al. model showed the water saturation term to be negligible for characterizing the fluid front. The strong interdependence of different parameters (relative humidity, channel width, paper type) has left the paper-based microfluidic device designers with an optimization challenge.

Practical tools to accurately describe fluid transport in paper devices will become increasingly important as the designs of the devices evolve from 1-D to 3-D (Han et al. 2016; Kalish and Tsutsui 2014; Kalish and Tsutsui 2016; Li and Liu 2014; Liu and Crooks 2011; Martinez et al. 2008a) as well as incorporate advanced timing (Chen et al. 2012; Fu et al. 2012; Toley et al. 2013; Toley et al. 2015) and demultiplexing/multiplexing functions (Cate et al. 2015; Lopez-Marzo and Merkoci 2016). The current study has created a library of paper-specific properties (e.g. water saturation, evaporation flux, effective permeability) for common cellulose papers used in the field of paper-based microfluidics. Effective use of this information will allow researchers to design more precise and reproducible paper-based microfluidic devices.

References

Abe K, Kotera K, Suzuki K, Citterio D (2010) Inkjet-printed paperfluidic immuno-chemical sensing device Analytical and Bioanalytical Chemistry 398:885-893 doi:10.1007/s00216-010-4011-2

Alava M, Dube M, Rost M (2004) Imbibition in disordered media Adv Phys 53:83-175 doi:Doi 10.1080/00018730410001687363

Amaral LAN, Barabasi AL, Buldyrev SV, Harrington ST, Havlin S, Sadrlahijany R, Stanley HE (1995) Avalanches and the Directed Percolation Depinning Model - Experiments, Simulations, and Theory Phys Rev E 51:4655-4673 doi:DOI 10.1103/PhysRevE.51.4655

Apilux A, Ukita Y, Chikae M, Chailapakul O, Takamura Y (2013) Development of automated paper-based devices for sequential multistep sandwich enzyme-linked immunosorbent assays using inkjet printing Lab Chip 13:126-135 doi:10.1039/c2lc40690j

Ballerini DR, Li X, Shen W (2011) Flow control concepts for thread-based microfluidic devices Biomicrofluidics 5 doi:Artn 014105
10.1063/1.3567094

Berli CLA, Kler PA (2016) A quantitative model for lateral flow assays Microfluid Nanofluid 20 doi:Artn 104
10.1007/S10404-016-1771-9

Bledzki AK, Gassan J (1999) Composites reinforced with cellulose based fibres Prog Polym Sci 24:221-274 doi:Doi 10.1016/S0079-6700(98)00018-5

Bohm A, Carstens F, Trieb C, Schabel S, Biesalski M (2014) Engineering microfluidic papers: effect of fiber source and paper sheet properties on capillary-driven fluid flow Microfluid Nanofluid 16:789-799 doi:10.1007/s10404-013-1324-4

Carrilho E, Martinez AW, Whitesides GM (2009) Understanding Wax Printing: A Simple Micropatterning Process for Paper-Based Microfluidics Anal Chem 81:7091-7095 doi:10.1021/ac901071p

Cate DM, Noblitt SD, Volckens J, Henry CS (2015) Multiplexed paper analytical device for quantification of metals using distance-based detection Lab Chip 15:2808-2818 doi:10.1039/c5lc00364d

Chen H, Cogswell J, Anagnostopoulos C, Faghri M (2012) A fluidic diode, valves, and a sequential-loading circuit fabricated on layered paper Lab Chip 12:2909-2913 doi:Doi 10.1039/C2lc20970e

Chitnis G, Ding ZW, Chang CL, Savran CA, Ziaie B (2011) Laser-treated hydrophobic paper: an inexpensive microfluidic platform Lab Chip 11:1161-1165 doi:10.1039/c0lc00512f

Connelly JT, Rolland JP, Whitesides GM (2015) "Paper Machine" for Molecular Diagnostics Anal Chem 87:7595-7601 doi:10.1021/acs.analchem.5b00411

Elizalde E, Urteaga R, Berli CLA (2015) Rational design of capillary-driven flows for paper-based microfluidics Lab Chip 15:2173-2180 doi:10.1039/c4lc01487a

Fenton EM, Mascarenas MR, Lopez GP, Sibbett SS (2009) Multiplex Lateral-Flow Test Strips Fabricated by Two-Dimensional Shaping Acs Applied Materials & Interfaces 1:124-129 doi:Doi 10.1021/Am800043z

Fridley GE, Le H, Yager P (2014) Highly Sensitive Immunoassay Based on Controlled Rehydration of Patterned Reagents in a 2-Dimensional Paper Network Anal Chem 86:6447-6453 doi:10.1021/ac500872j

Fries N, Odic K, Conrath M, Dreyer M (2008) The effect of evaporation on the wicking of liquids into a metallic weave J Colloid Interf Sci 321:118-129 doi:Doi 10.1016/J.Jcis.2008.01.019

Fu E, Kauffman P, Lutz B, Yager P (2010) Chemical signal amplification in two-dimensional paper networks Sensor Actuat B-Chem 149:325-328 doi:Doi 10.1016/J.Snb.2010.06.024

Fu E, Liang T, Spicar-Mihalic P, Houghtaling J, Ramachandran S, Yager P (2012) Two-Dimensional Paper Network Format That Enables Simple Multistep Assays for Use in Low-Resource Settings in the Context of Malaria Antigen Detection Anal Chem 84:4574-4579 doi:Doi 10.1021/Ac300689s

Fu EL, Ramsey S, Kauffman P, Lutz B, Yager P (2011) Transport in two-dimensional paper networks Microfluid Nanofluid 10:29-35 doi:Doi 10.1007/S10404-010-0643-Y

Giokas DL, Tsogas GZ, Vlessidis AG (2014) Programming Fluid Transport in Paper-Based Microfluidic Devices Using Razor-Crafted Open Channels Anal Chem 86:6202-6207 doi:10.1021/ac501273v

Han KN, Choi JS, Kwon J (2016) Three-dimensional paper-based slip device for one-step point-of-care testing Sci Rep-Uk 6 doi:Artn 25710
10.1038/Srep25710

Hong S, Kim W (2015) Dynamics of water imbibition through paper channels with wax boundaries Microfluid Nanofluid 19:845-853 doi:10.1007/s10404-015-1611-3

Jahanshahi-Anbuhi S et al. (2014) Paper-based microfluidics with an erodible polymeric bridge giving controlled release and timed flow shutoff Lab Chip 14:229-236 doi:10.1039/c3lc50762a

Jiang X, Fan ZH (2016) Fabrication and Operation of Paper-Based Analytical Devices Annual review of analytical chemistry 9:203-222 doi:10.1146/annurev-anchem-071015-041714

Kalish B, Tsutsui H (2014) Patterned adhesive enables construction of nonplanar three-dimensional paper microfluidic circuits Lab Chip 14:4354-4361 doi:10.1039/c4lc00730a

Kalish B, Tsutsui H (2016) Using Adhesive Patterning to Construct 3D Paper Microfluidic Devices Journal of visualized experiments : JoVE doi:10.3791/53805

Kardar M, Parisi G, Zhang YC (1986) Dynamic Scaling of Growing Interfaces Phys Rev Lett 56:889-892 doi:DOI 10.1103/PhysRevLett.56.889

Kauffman P, Fu E, Lutz B, Yager P (2010) Visualization and measurement of flow in two-dimensional paper networks Lab Chip 10:2614-2617 doi:Doi 10.1039/C004766j

Krug J, Meakin P (1991) Kinetic Roughening of Laplacian Fronts Phys Rev Lett 66:703-706 doi:DOI 10.1103/PhysRevLett.66.703

Li X, Liu XY (2014) Fabrication of three-dimensional microfluidic channels in a single layer of cellulose paper Microfluid Nanofluid 16:819-827 doi:DOI 10.1007/s10404-014-1340-z

Li X, Tian JF, Garnier G, Shen W (2010) Fabrication of paper-based microfluidic sensors by printing Colloids and Surfaces B-Biointerfaces 76:564-570 doi:Doi 10.1016/J.Colsurfb.2009.12.023

Liu H, Crooks RM (2011) Three-Dimensional Paper Microfluidic Devices Assembled Using the Principles of Origami J Am Chem Soc 133:17564-17566 doi:Doi 10.1021/Ja2071779

Liukkonen A (1997) Contact angle of water on paper components: Sessile drops versus environmental scanning electron microscope measurements Scanning 19:411-415

Lopez-Marzo AM, Merkoci A (2016) Paper-based sensors and assays: a success of the engineering design and the convergence of knowledge areas Lab Chip doi:10.1039/c6lc00737f

Lucas R (1918) The time law of the capillary rise of liquids. Kolloid-Zeitschrift 23:15-22 doi:Doi 10.1007/Bf01461107

Lutz B, Liang T, Fu E, Ramachandran S, Kauffman P, Yager P (2013) Dissolvable fluidic time delays for programming multi-step assays in instrument-free paper diagnostics Lab Chip 13:2840-2847 doi:10.1039/c3lc50178g

Martinez AW, Phillips ST, Butte MJ, Whitesides GM (2007) Patterned paper as a platform for inexpensive, low-volume, portable bioassays Angew Chem Int Edit 46:1318-1320 doi:Doi 10.1002/Anie.200603817

Martinez AW, Phillips ST, Whitesides GM (2008a) Three-dimensional microfluidic devices fabricated in layered paper and tape P Natl Acad Sci USA 105:19606-19611 doi:DOI 10.1073/pnas.0810903105

Martinez AW, Phillips ST, Wiley BJ, Gupta M, Whitesides GM (2008b) FLASH: A rapid method for prototyping paper-based microfluidic devices Lab Chip 8:2146-2150 doi:10.1039/b811135a

Masoodi R, Pillai KM (2010) Darcy's Law-Based Model for Wicking in Paper-Like Swelling Porous Media Aiche Journal 56:2257-2267 doi:Doi 10.1002/Aic.12163

Mendez S et al. (2010) Imbibition in Porous Membranes of Complex Shape: Quasi-stationary Flow in Thin Rectangular Segments Langmuir : the ACS journal of surfaces and colloids 26:1380-1385 doi:Doi 10.1021/La902470b

Moon RJ, Martini A, Nairn J, Simonsen J, Youngblood J (2011) Cellulose nanomaterials review: structure, properties and nanocomposites Chem Soc Rev 40:3941-3994 doi:Doi 10.1039/C0cs00108b

Noh N, Phillips ST (2010) Metering the Capillary-Driven Flow of Fluids in Paper-Based Microfluidic Devices Anal Chem 82:4181-4187 doi:10.1021/ac100431y

Park J, Shin JH, Park JK (2016) Experimental Analysis of Porosity and Permeability in Pressed Paper Micromachines-Basel 7 doi:10.3390/mi7030048

Renault C, Li X, Fosdick SE, Crooks RM (2013) Hollow-channel paper analytical devices Anal Chem 85:7976-7979 doi:10.1021/ac401786h

Richards LA (1931) Capillary conduction of liquids through porous mediums Physics-J Gen Appl P 1:318-333 doi:Doi 10.1063/1.1745010

Schuchardt DR, Berg JC (1991) Liquid Transport in Composite Cellulose-Superabsorbent Fiber Networks Wood Fiber Sci 23:342-357

Shou DH, Ye L, Fan JT, Fu KK, Mei MF, Wang HJ, Chen Q (2014) Geometry-Induced Asymmetric Capillary Flow Langmuir : the ACS journal of surfaces and colloids 30:5448-5454 doi:10.1021/la500479e

Songok J, Salminen P, Toivakka M (2014) Temperature effects on dynamic water absorption into paper J Colloid Interface Sci 418:373-377 doi:10.1016/j.jcis.2013.12.017

Toley BJ, McKenzie B, Liang T, Buser JR, Yager P, Fu E (2013) Tunable-Delay Shunts for Paper Microfluidic Devices Anal Chem 85:11545-11552 doi:Doi 10.1021/Ac4030939

Toley BJ et al. (2015) A versatile valving toolkit for automating fluidic operations in paper microfluidic devices Lab Chip 15:1432-1444 doi:10.1039/c4lc01155d

Washburn EW (1921) The dynamics of capillary flow. Physical Review 17:273-283 doi:Doi 10.1103/Physrev.17.273

Weng CH, Chen MY, Shen CH, Yang RJ (2014) Colored wax-printed timers for two-dimensional and three-dimensional assays on paper-based devices Biomicrofluidics 8 doi:Artn 066502
10.1063/1.4902246

Xia Y, Si J, Li Z (2016) Fabrication techniques for microfluidic paper-based analytical devices and their applications for biological testing: A review Biosensors & bioelectronics 77:774-789 doi:10.1016/j.bios.2015.10.032

Yetisen AK, Akram MS, Lowe CR (2013) Paper-based microfluidic point-of-care diagnostic devices Lab Chip 13:2210-2251 doi:10.1039/c3lc50169h

4. IMBIBITION IN TWO-DIMENSIONAL WAX-BOUND PAPER CHANNELS

4.1. Introduction

Paper-based microfluidics have emerged as a tool to create inexpensive microfluidic devices for chemical analysis or medical diagnosis. Such devices commonly use cellulose paper or nitrocellulose membranes. Because paper is a low-cost, ubiquitous, and a self-wicking material, it is an ideal substrate for developing simple-to-use, portable, and disposable devices for fluid specimen. Existing devices are typically simple lateral-flow tests whose functions are limited to low-level qualitative detection of analytes. To significantly expand functionality of paper-based analytical devices, it is necessary to better understand fluid transport within the channel networks defined on the paper substrate.

Channels in paper-based microfluidics are fabricated by either cutting the paper substrate to the desired design or by pattering the design with a hydrophobic material on the paper substrate. When pattering the channel network is preferred, methods range from those of traditional photolithography (Martinez et al. 2007; Martinez et al. 2008), to techniques using commercially available printers, including ink-jet (Abe et al. 2010; Abe et al. 2008) or solid ink (Carrilho et al. 2009; Lu et al. 2009). In solid ink printing, a commercially available printer (e.g. Xerox ColorQube 8880) uses a wax-based ink. After the pattern is printed, the wax pattern is either melted using an oven or a hotplate, resulting in an impermeable channel boundary.

In order to improve paper-based microfluidics' capabilities, the paper device must incorporate multi-step processes such as those found in enzyme-linked immunosorbent assays (ELISA) where timed sequences of manual pipetting are needed with washes in between every step. An important aspect of the multi-step processes is attained through controlled sequential delivery. Fu et al. (2010) used a laser to cut nitrocellulose membrane with varying channel lengths to create a multi-step mixing process. Lutz et al. (2011) used a nitrocellulose membrane network of varying channel lengths in a plastic housing containing a buffer solution that served all inlets. This platform allows for sequential delivery as well as a programmed disconnection of flow in the channels. In addition to the channel length, changing the cross section of the channel can also be used to implement sequential delivery. Fu et al. (2011) briefly investigated how sudden geometric changes, such as expansion and contraction of the channel, affected fluid flow in a nitrocellulose membranes. As expected, an expansion of the width of the channel slowed the fluid front propagation, while a contraction caused the fluid front to accelerate. Analytical relationships for the wet-out (imbibition) process have been developed with the aim of better understanding fluid flow in two-dimensional paper networks. Medina et al. (2001) investigated wicking in blotting paper with different geometrical shapes and found that correction terms to the Lucas-Washburn (L-W) equation are needed to appropriately describe the flow in the channels. Mendez et al. (2010) investigated how the radial expansion in two-dimensions affected flow in nitrocellulose membranes. It was found that the gradual increase in cross-sectional area of the channel caused the wicking fluid to maintain a quasi-steady state flow, where the fluid speed remains constant.

Here, the effort of fluid manipulation is continued, specifically to that of cellulose paper. We qualitatively investigate channels with the most basic geometrical changes that may be present in complex fluidic designs. These include a sudden increase in channel width, a sudden decrease in channel width, and a square box along the channel (as a reaction or mixing chamber).

4.2. Materials and methods

4.2.1. Materials and fabrication

Three different paper types were surveyed in this study: Whatman qualitative filter paper of Grade #1, Grade #4, and Grade #5 (GE Healthcare, Pittsburgh, PA). Based on the distance wicked over time, the paper types can be classified into three qualitative imbibition speeds, medium, fast, and slow, respectively. The channel geometries were designed in SolidWorks (Dassault Systèmes, Vélizy-Villacoublay, France). The designed channels were printed on filter paper using a solid wax ink printer (Xerox Phaser 8860) following previously published methods (Carrilho et al. 2009; Lu et al. 2009). The printed paper was then placed on a hotplate for two minutes at 170°C melting the wax, allowing it to penetrate through the paper, creating hydrophobic channel boundaries. Channels were designed such that the desired channel dimensions are achieved postmelting (see Fig. I.1 in Appendix I). All imbibition experiments were conducted using a 5 mM solution of Allura Red AC. Allura Red AC was purchased from Sigma-Aldrich (St. Louis, MO) and dissolved in ultrapure water (18.2 MΩ-cm) prepared by a Millipore Synergy UV water purification system (Billerica, MA).

4.2.2. Data acquisition and analysis

The imbibition process took place in an open lab environment with an ambient relative humidity of 50 ± 2% and temperature of 22 ± 1°C. The channels were fixed vertically on a mount. A reservoir containing the wicking fluid was placed onto a laboratory jack (Model L-490, Thorlabs, Newton, NJ). The jack's platform was then raised quickly to the start line of the channels.

The imbibition process was recorded using a Nikon D5100 digital camera (Tokyo, Japan). Image frames were then extracted from the recorded video files. Imbibition distance was then measured at the centerline position of the liquid front using ImageJ with the Manual Tracking plug-in. Six replicates were tested for each combination. The combinations include variations in paper type and channel geometry type with three respective contraction-expansion variations.

4.3. Results and discussion

We investigate the most basic geometrical changes that can occur in a channel network. These include a sudden increase in channel width, a sudden decrease in channel width, and a square box along the channel (as a reaction or mixing chamber). It is worth noting that some of these sudden changes in channel width violate the non-limiting source requirement of the L-W equation. Nevertheless, in certain instances L-W like flow seems to hold.

These wax-bound channels are two-dimensional wet-out flows with sudden rectangular geometry changes. It was shown that channels with a larger expansion had larger wicking times (Fig. 4.1). This was due to the radial fluid front expanding onto the increased volume. In the case of sudden contraction, the width of the larger segment acted as a non-limiting source to the smaller segment. This allowed flow in the downstream of the narrower segment to follow the L-W equation, with a slight increase in speed at the varying geometric interface. To better visualize the divergence from the L-W flow, the wicking distance curves are plotted as a function of the square root of time (Fig. 4.1). In these plots, L-W flow is when the curves are linear with a positive slope.

4.3.1. Sudden channel expansion

Relating to Fu’s observation in nitrocellulose membrane (Fu et al. 2010), a sudden expansion of channel width should cause a decrease in flow speed. We confirmed that this is indeed happening and investigated the effect of expansion ratio on imbibition in the three paper types. We compared three different expansion ratios, 1:2, 1:3, and 1:4, with a base channel of 2 mm in three different paper types. With the geometric change located at a distance of 10 mm. For example, a Whatman #1 with a 1:3 ratio will have an initial channel of 2 mm up to a distance of 10 mm and a larger channel of 6 mm after the geometric change.

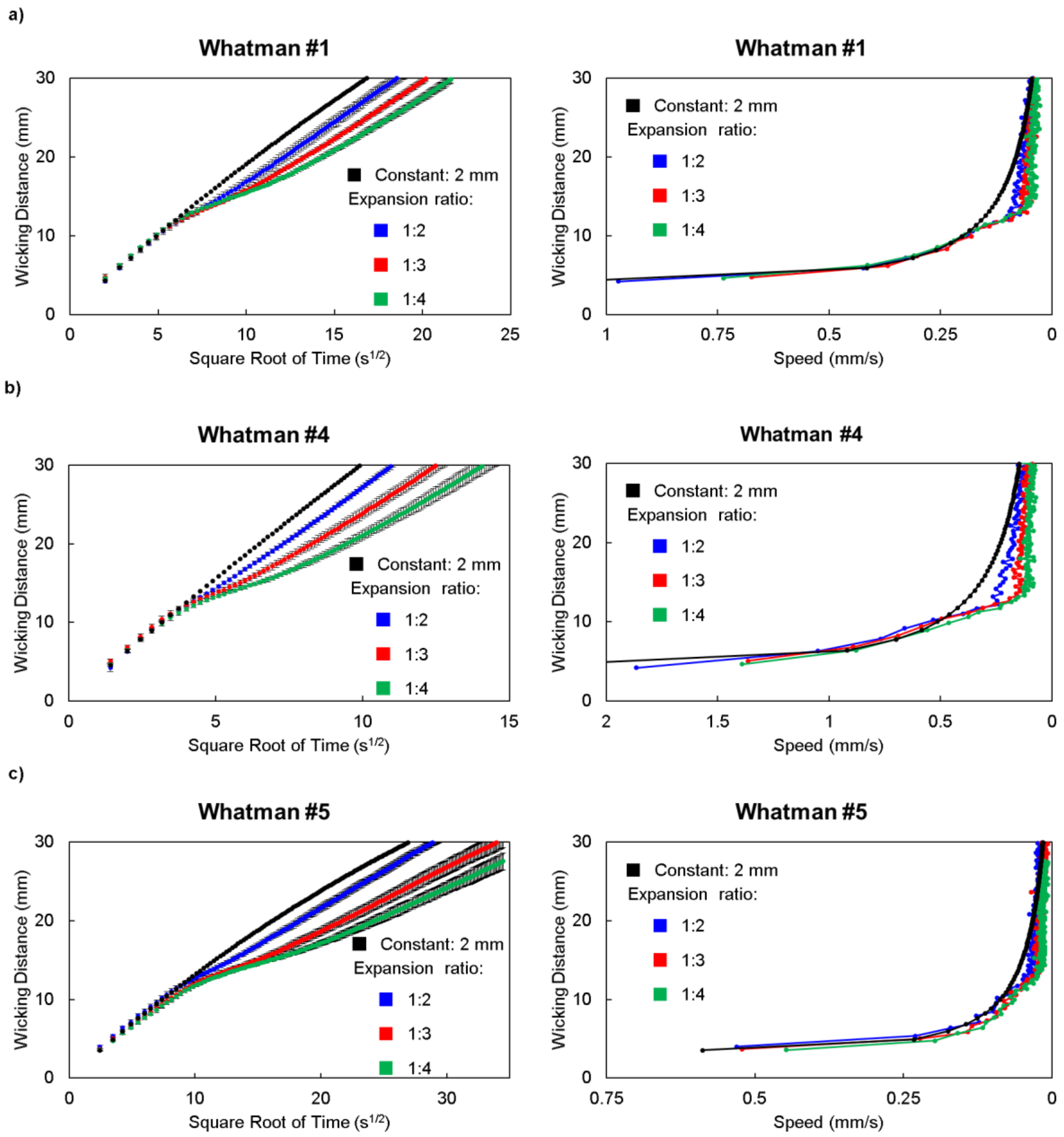

Fig. 4.1 Sudden expansion geometry. a) Whatman #1 paper. b) Whatman #4 paper. c) Whatman #5 paper. Wicking distance data shown as mean ± SD (N = 6).

Fig. 4.1 shows the wicking distance vs square root of time. At the point of the sudden geometry change (~10 mm), the flow stops being L-W like as seen by the deviation from the linearity. At this instance the flow expands radially until it reaches the edge (See Fig. 4.2 for a time sequence visualization). There exists a slight time delay until the fluid front becomes flat at the centerline, at which point, the wicking data becomes linearly dependent on the square root of time. Depending of the paper type and expansion ratio the deviation from L-W flow can last for approximately 25-120 seconds for Whatman #1, 10-40 seconds for Whatman #4, and 45-300 seconds for Whatman #5. The faster the paper type the faster the recovery.

Fig. 4.1 also shows the wicking distance as a function of speed. As seen, in the initial stages of imbibition there is a rapid uptake of water. This sudden up take of water rapidly decreases within a few millimeters. Nonetheless, after the fluid flow reaches a flat front, the speed converges to that of the L-W flow. The deceleration in speed due to the sudden channel expansion is more evident in the faster wicking paper. As expected, the larger the expansion ratio the greater the deceleration. These trends are seen across all three paper types.

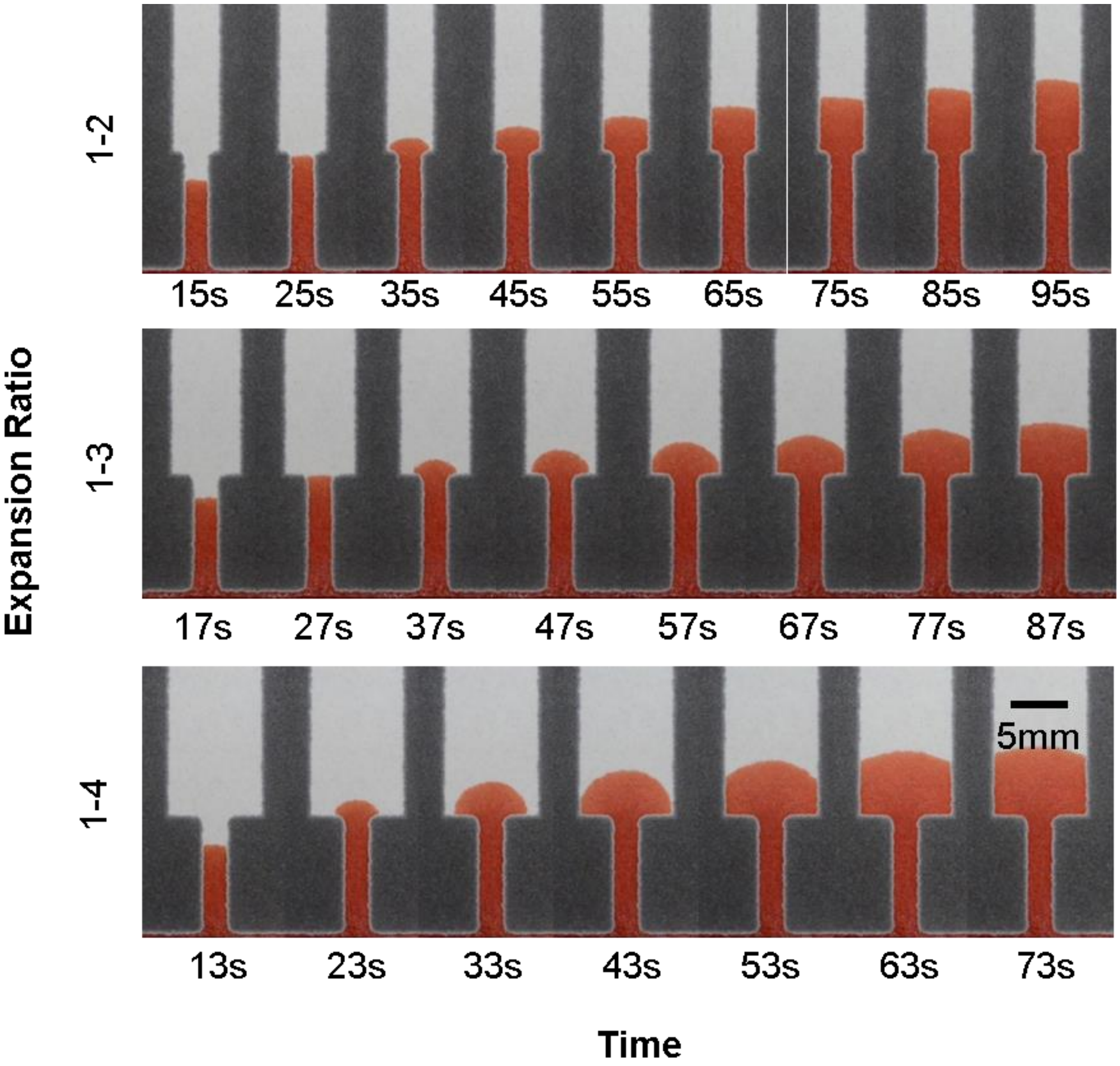

Fig. 4.2 Time lapse of different sudden expansion ratios. Whatman #1 paper shown.

4.3.2. Sudden channel contraction

Next we investigated whether fluid behavior through a sudden contraction of channel width follows the same observations of that seen by Fu et al. (2010). Three contraction ratios, 2:1, 3:1, and 4:1 based on a 2 mm width channel on three different paper types were tested.

Fig. 4.3 shows the wicking distance vs square root of time. At the point of the sudden geometry reduction (~10 mm), the flow slightly stops being L-W like as seen by the deviation from the linearity. At this instance (See Fig. 4.4 for a time sequence visualization) the flow is accelerated briefly until it gradually reconverges to the speed of the constant channel. This observation agrees with Fu et al. (2010) observation of flow continuing the L-W behavior. Depending of the paper type and contraction ratio, the speed can increase approximately 20% for Whatman #1, 60% for Whatman #4, and 8% for Whatman #5. The faster the paper type, the faster the overall increase in speed.

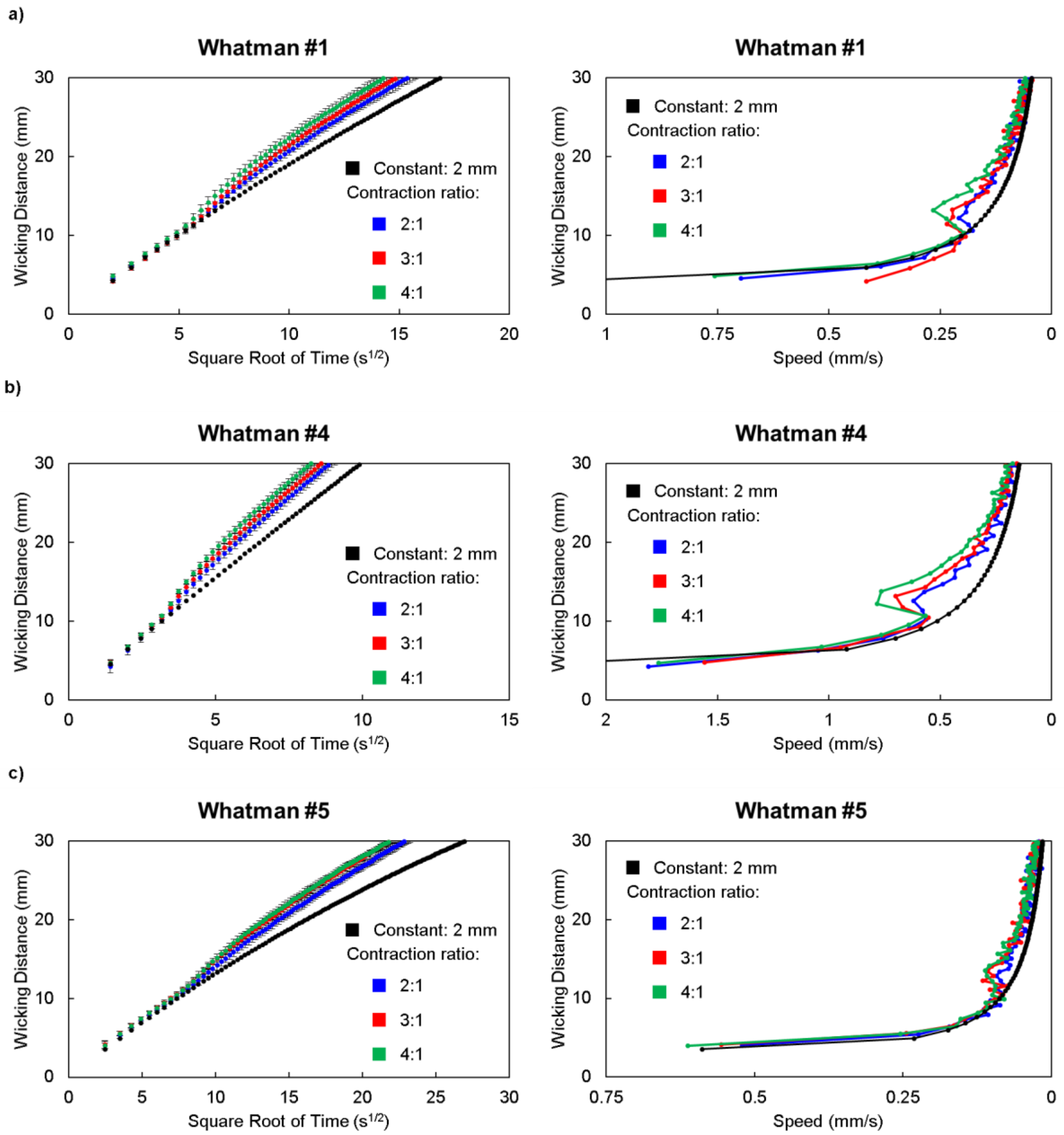

Fig. 4.3 Sudden contraction geometry. a) Whatman #1 paper. b) Whatman #4 paper. c) Whatman #5 paper. Wicking distance data shown as mean ± SD (N = 6).

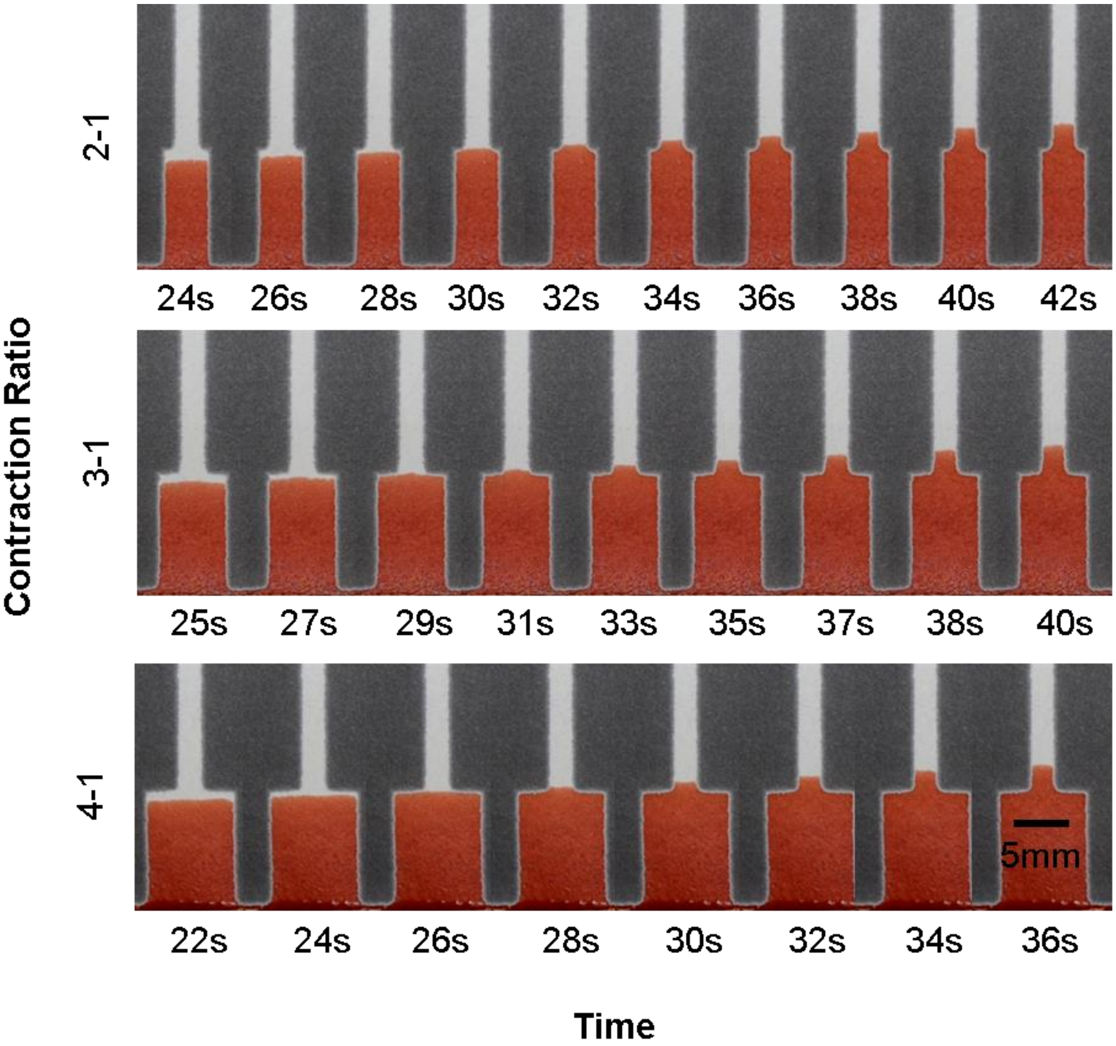

Fig. 4.4 Time lapse of different sudden contraction ratios. Whatman #1 paper shown.

4.3.3. Box along channel

Lastly, we also investigated flow through a sudden square box to see whether the combined expansion and contraction canceled the acceleration/deceleration effects seen earlier. Ratios include, 1:2:1, 1:3:1, 1:4:1. The wicking plots (Fig. 4.5) show that the flow reconverges to that of the constant width channel after the fluid passes thought the box geometry. The flow reconvergence is better seen in the slower wicking paper (Whatman #5). We see that the time of the convergence increases as the box size increases, which is expected since the converging flow happens only when the channel contracts, as seen in the precious section 4.3.2. By incorporating this square box onto a channel, a throttling effect can be created by decreasing and increasing flow speeds transitionally.

Fig. 4.6 shows a time lapse sequence of the Whatman #1 (medium speed) paper during the advancement of the fluid front. As seen previously in the sudden expanding channel, the flow decelerates upon entering the box. This deceleration continues until the fluid front reaches the end of the box, where a sudden contraction occurs.

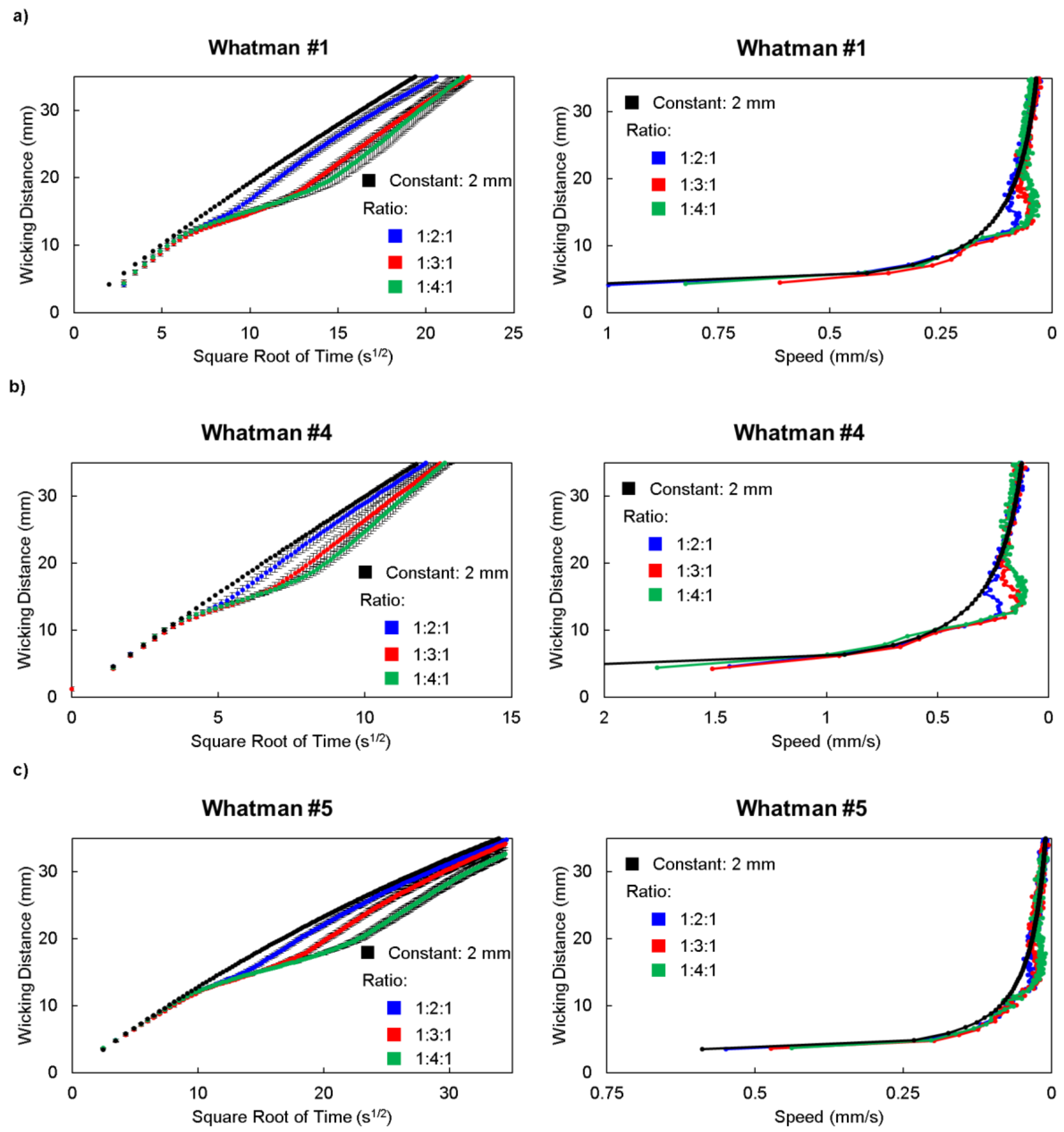

Fig. 4.5 Sudden box along the channel. a) Whatman #1 paper. b) Whatman #4 paper. c) Whatman #5 paper. Wicking distance data shown as mean ± SD (N = 6).

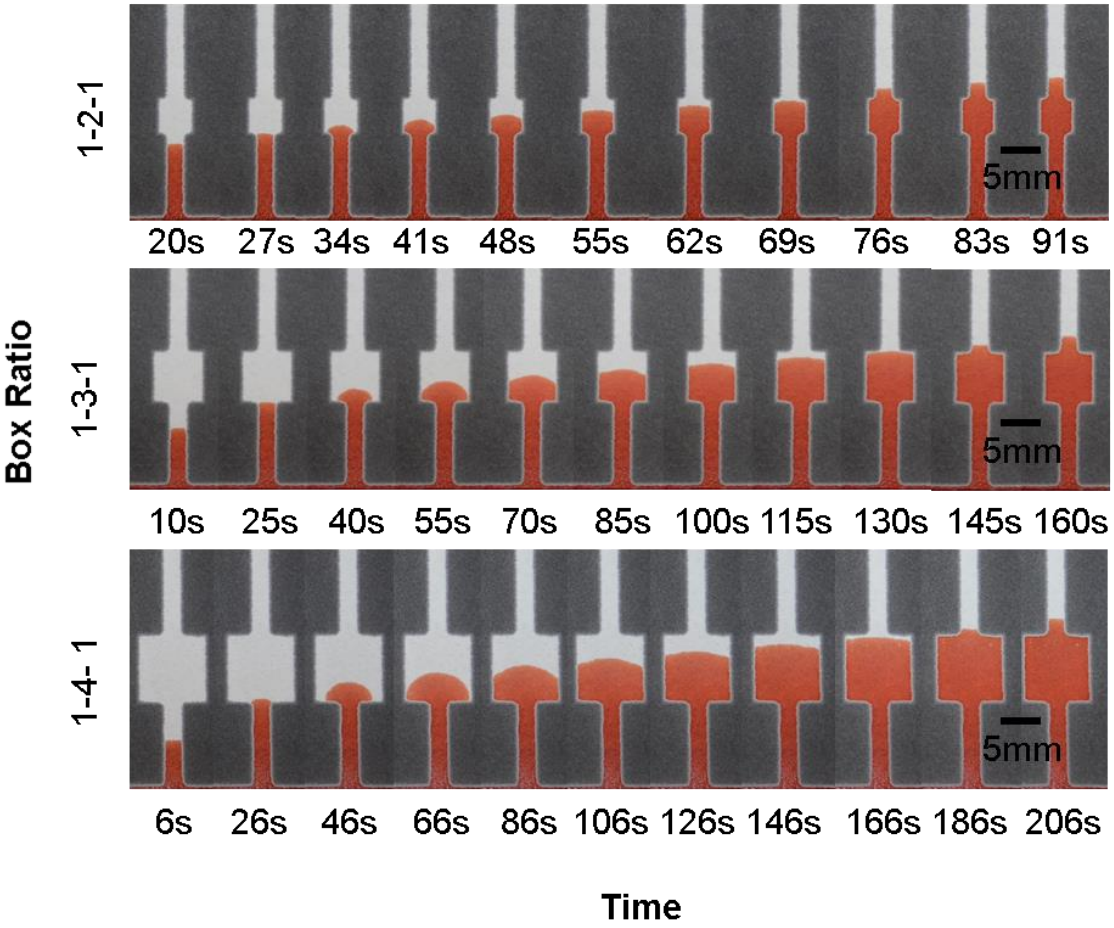

Fig. 4.6 Time lapse of different sudden box ratios. Whatman #1 paper shown.

4.4. Conclusion

Simple lateral-flow tests are limited in functionality. The key to increase the complexity of paper-based microfluidic devices is sequential delivery. A method to accomplish this sequential delivery of fluids is by two-dimensional flows. These flows are created by varying the cross-section of the channel. Here we investigated wax-bound channels encompassing the most basic geometrical changes that may be present in complex fluidic designs; sudden expansion, contraction, and a box along the channel. We found that a sudden expansion can significantly delay and decrease the speed of the fluid flow, with its intensity depending on the paper type and channel ratio. The sudden contraction can momentarily increase the speed of the fluid front. The paper type is a more significant parameter than the channel ratio. Incorporating a box along the channel can potentially serve as a mixing chamber. This geometry set-up combines both the decelerating and accelerating effect seen in the other geometries to momentarily delay the fluid flow.

Though this study was conducted without the use of precise environmental controls such as those used in chapter 3, results show a clear method to accomplish sequential delivery of liquid. These preliminary studies will provide the basis for future studies where more complex geometrical changes are investigated under controlled environments as well as aid in deriving simple yet accurate models toward developing systematic designs of complex channel networks.

References

Abe K, Kotera K, Suzuki K, Citterio D (2010) Inkjet-printed paperfluidic immuno-chemical sensing device Anal Bioanal Chem 398:885-893 doi:10.1007/s00216-010-4011-2

Abe K, Suzuki K, Citterio D (2008) Inkjet-printed microfluidic multianalyte chemical sensing paper Anal Chem 80:6928-6934 doi:10.1021/ac800604v

Carrilho E, Martinez AW, Whitesides GM (2009) Understanding Wax Printing: A Simple Micropatterning Process for Paper-Based Microfluidics Anal Chem 81:7091-7095 doi:10.1021/ac901071p

Fu E, Lutz B, Kauffman P, Yager P (2010) Controlled reagent transport in disposable 2D paper networks Lab Chip 10:918-920 doi:10.1039/b919614e

Fu EL, Ramsey S, Kauffman P, Lutz B, Yager P (2011) Transport in two-dimensional paper networks Microfluid Nanofluid 10:29-35 doi:Doi 10.1007/S10404-010-0643-Y

Lu Y, Shi WW, Jiang L, Qin JH, Lin BC (2009) Rapid prototyping of paper-based microfluidics with wax for low-cost, portable bioassay Electrophoresis 30:1497-1500 doi:Doi 10.1002/Elps.200800563

Lutz BR, Trinh P, Ball C, Fu E, Yager P (2011) Two-dimensional paper networks: programmable fluidic disconnects for multi-step processes in shaped paper Lab Chip 11:4274-4278 doi:10.1039/c1lc20758j

Martinez AW, Phillips ST, Butte MJ, Whitesides GM (2007) Patterned paper as a platform for inexpensive, low-volume, portable bioassays Angew Chem Int Edit 46:1318-1320 doi:Doi 10.1002/Anie.200603817

Martinez AW, Phillips ST, Wiley BJ, Gupta M, Whitesides GM (2008) FLASH: A rapid method for prototyping paper-based microfluidic devices Lab Chip 8:2146-2150 doi:10.1039/b811135a

Medina A, Perez-Rosales C, Pineda A, Higuera FJ (2001) Imbibition in pieces of paper with different shapes Rev Mex Fis 47:537-541

Mendez S et al. (2010) Imbibition in Porous Membranes of Complex Shape: Quasi-stationary Flow in Thin Rectangular Segments Langmuir : the ACS journal of surfaces and colloids 26:1380-1385 doi:Doi 10.1021/La902470b

5. CONCLUSIONS

Paper-based microfluidics, though not new, allow for the creation of an inexpensive self-contained analytical device. Paper is abundant, self-wicking, and a versatile material readily available with an array of physical properties. It is highly adaptable to different fabrication methods ranging from simple craft cutting to using commercially available printing technologies. Since the seminal work by Martinez et al. (2007), the paper-based microfluidic community has rapidly expanded. The low-cost, ease-of-use, lightweight, and rapid prototyping of paper devices have allowed point-of-care technologies to be more accessible to low-resource settings. Reagent detection techniques from simple colorimetry to highly sensitive electrochemical sensing have allowed for a wide range of different applications ranging from food safety to environmental monitoring. There is a continuous effort to increase the sensitivity and specificity to become vital competitors as a diagnostic and analytical tool. An increase in device sophistication is directly coupled with accurately manipulating fluid flow. This has led the field of paper-based microfluidics to develop an array of fluid control methods with complex sequential delivery capabilities.

The accuracy of the liquid behavior has become increasingly important. Imbibition studies are needed to investigate how certain parameters influence the wicking behavior. In this dissertation, an extensive series of controlled experiments where conducted on commonly used paper types to investigate the effect of varying relative humidity and channel width. It was found that as the relative humidity increased the imbibition distance increased and as the channel width increased the imbibition distance increased with the effect reaching an asymptotic value with the increase in channel width. To characterize the imbibition front of all surveyed combinations and to assess the importance of relative humidity, we compared three capillary tube models, the L-W model, the Fries et al. (2008) model which incorporates evaporation, and a newly developed water saturation model, where evaporation and residual water are incorporated. Evaporation is an important parameter for imbibition, therefore must be taken into account. In general, evaporation is dominant compared to water saturation, therefore the water saturation model is not more advantage to the Fries et al. model. Effective use of this information will allow researchers to better design more precise and reproducible paper-based microfluidic devices.

The key to increase the complexity of paper-based microfluidic devices is sequential delivery. Here we investigated wax-bound channels encompassing the most basic geometrical changes that may be present in complex fluidic designs; sudden expansion, contraction, and a box along the channel. The results show a clear method to accomplish sequential delivery of liquid. These studies will provide the basis for future studies where more complex geometrical changes are investigated under controlled environments as well as aid in deriving accurate models to develop systematic designs of complex channel networks.

References

Fries N, Odic K, Conrath M, Dreyer M (2008) The effect of evaporation on the wicking of liquids into a metallic weave J Colloid Interf Sci 321:118-129 doi:Doi 10.1016/J.Jcis.2008.01.019

Martinez AW, Phillips ST, Butte MJ, Whitesides GM (2007) Patterned paper as a platform for inexpensive, low-volume, portable bioassays Angew Chem Int Edit 46:1318-1320 doi:Doi 10.1002/Anie.200603817

6. SUGGESTED FUTURE WORK

6.1. Effect of channel width and relative humidity

The results shown in this dissertation, which investigated the effect of relative humidity and channel width on imbibition, have provided a vast amount of data that can be used by the paper-based microfluidic community. The data was fitted to three capillary models; Lucas-Washburn (Lucas 1918; Washburn 1921), Fries et al. (2008), and a water saturation model to obtain the effective permeabilities of the channels. The effective permeabilities for the models extracted from the experimental data show that the effective permeability asymptotically approaches an upper limit with the increasing channel width. Additionally, a linear relationship with a positive slope with relative humidity, irrespective of the channel width, is observed. Future work in the following three main areas will further the understanding of relationships between the transport properties of paper and its interaction with water.

6.1.1. Channel width obstruction

The asymptotic relation between the effective permeability and channel width is very intriguing. According to the capillary tube model any potential width effect should not be present. This potentially could be an issue attributed to scalability. As suggested by Bohm et al. (2014) possible dead-end pores created when the fiber length is larger than the width of the channel can terminate the flow at the edge causing inhibitory effects. This issue can be further investigated by obtaining high-resolution microscopic images of cut edges such as those obtained from scanning electron microscopy (SEM) or by optical microscopes. The combination with video recording of imbibition in the micro-scale will help determine if dead-end pores do in fact exist as well as if they contribute to the increased flow resistance observed in narrow channels.

Additionally, possible cause of the inhibitory effect is due to the method in which the paper was cut. The laser cutter works by sending a high powered beam capable of obliterating the material. In paper, the cut edge is essentially microscopically burnt. This affects the edge by leaving behind residue such as soot. This can be seen in the image below (Fig. 6.1). If this residue is hydrophobic, the increase in contact angle at the edge will retard the flow as was determined by Hong and Kim (2015) with other hydrophobic materials. Therefore, it will be valuable to investigate whether multiple washes eliminate or reduce such channel width effect. Moreover, alternative fabrication methods that do not deform or significantly alter the channel edge should be explored.

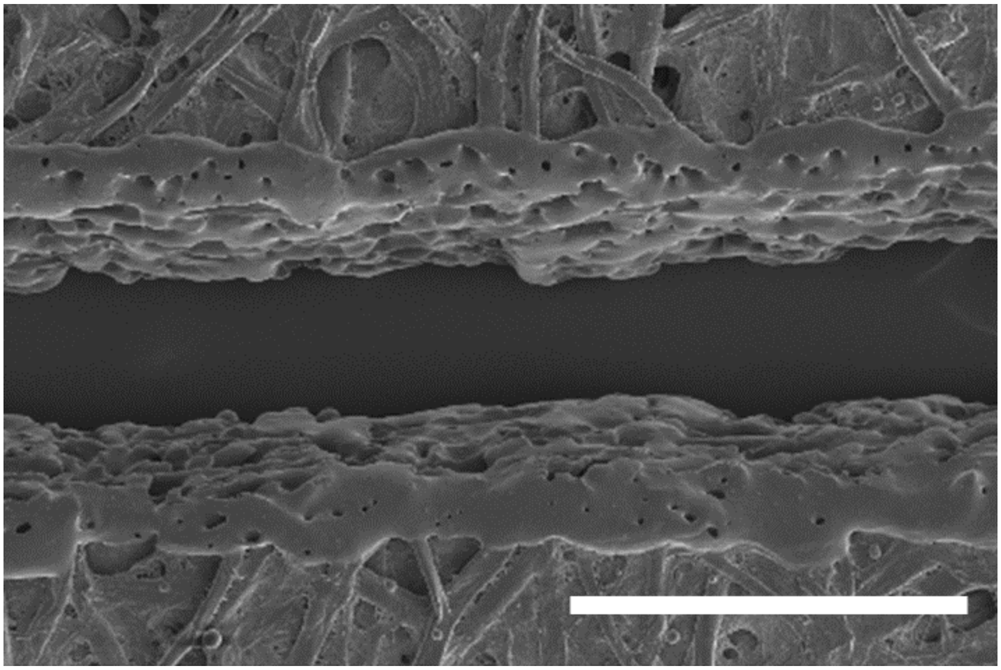

Fig. 6.1 SEM image of Whatman #1 showing laser cut edge. Residue at edges is present after cut. Scale bar: 300 µm.

Finally, the increased resistance associated with channel width could be exclusively a source of the cellulose paper. Therefore, a study investigating other “paper” types that are not made of cellulose fibers, such as nitrocellulose or nylon membranes will help determine the extent of the channel width phenomena.

6.1.2. Relative humidity: Increased imbibition

Relative humidity can alter the paper by two possible mechanisms; 1) either through water leaving the paper 2) or through water entering the paper. The effective permeability extracted for the three models show a consistent linear relationship with a positive slope with relative humidity, irrespective of channel width as well as paper type. Because there is a dependence of relative humidity on the effective permeability, future work will help determine possible unknown sources influencing the liquid flow.

Undetermined evaporation could be a sole culprit. Ways to completely eliminate evaporation should be explored. This can be accomplished by laminating the paper with a transparent film, paying close attention as not to deform the paper substrate. The evaporation flux can be much higher within the imbibition front region creating non-uniform evaporation flux. This was computationally studied by Veran-Tissoires et al. (2012) while investigating salt on porous media. If evaporation is indeed higher than what was measured, the effective permeability vs relative humidity plots are expected to approach a much more horizontal relationship.

Aside from undetermined evaporation, the relative humidity dependence in the effective permeability might be attributed to a previously undetermined effect caused by the residual water. A precursor film with the aid of the residual water at higher relative humidity can potentially develop over the paper fibers. Visually undetected by the user, microscopic precursor films can develop ahead of the macroscopic flow (de Azevedo et al. 2008), particularly along the fibers (Hyvaluoma et al. 2006). Future work can investigate this possible phenomenon using advance imaging techniques such as magnetic resonance imaging (MRI) as well as x-ray microtomography (Beuther et al. 2010). These techniques give a detailed visualization of the imbibition process, down to the cellulose fiber length scales of approximately 30 μm.

6.1.3. Improving model parameters

The three models compared are derived assuming a rigid bundle of capillary tubes. The hygroscopic nature and inhomogeneous structure of the paper produces inherent complexities such as fibrous random networks, swelling deformation, and a wide distribution of pore sizes. To make the capillary tube models more physically meaningful, modifications and decoupling attempts have been proposed. For a brief overview of some of these approaches, please see section 2.3.2 Modification and application of Lucas-Washburn equation to paper media. Nevertheless, the underlining value and usefulness of the model modifications rely on obtaining accurate physical properties of the paper. Therefore future work should improve on the measurement and calculations of these values.

The highly stochastic nature of the paper manufacturing process leads to a high degree of inhomogeneity, where the macroscopic flow is influence by the microscopic arrangement of the cellulose fibers and pore space. This creates a challenge problem to accurately measure important properties such as pore size and porosity. A very valuable future contribution would be to obtain pore size data for the surveyed papers. The bubble point method can be used (Nassehi et al. 2011). It is based on the Young-Laplace equation where the pressure is inversely proportional to the pore diameter. By determining the pressure to force an air bubble though the pore, the average diameter (in the transverse direction) of the paper substrate can be obtained. Similarly to the bubble point method, using mercury intrusion will be useful in determining the pore size and porosity. Additionally, the pore size can be extracted using capillary theory by obtaining the maximum height of the water-paper column.

A more accurate value of pore size and porosity will help eliminate inaccuracies in the permeability calculation. Permeability is a function of the interconnectivity of the pores (tortuosity). Using imaging techniques such as the previously mentioned x-ray microtomography will help determine the arrangement and measure the interconnectivity of the cellulose fiber network. It is important to know that these methods will not result in a single defined value, but by using a combination of methods the individual parameters can be validated. But undoubtedly, the strong interdependence of different properties has left a challenge to future researchers.

6.2. Two-dimensional channels

Chapter 4 presented initial work on two-dimensional fluid flows. Though in its infancy, it gives a quick overview on how a sudden change in the channel’s cross-section can alter fluid flow. Unlike the presented data in chapter 4, future imbibition experiments need to be conducted inside an environmentally controlled chamber similar to the study in chapter 3. Findings obtained from investigating the effect of relative humidity and channel width should be applied to two-dimensional flows. These include physical properties of the paper such as pore size distribution, porosity, and permeability. Once these accurate values are obtained, analytical equations representing the flow should be developed. An analytical model for a two-segment channel was derived and is shown below for the main purpose of discussion. For full details see Appendix J.

$$
\begin{aligned}
& t+\frac{L_1^{\,2}}{2c}\ln\left(\frac{-c+a}{a}\right)=\frac{1}{2e}\ln\left(\frac{-a+c}{e(L-L_1)^2-a+c)}\right)+ \\
& \left(\frac{b}{\sqrt{-\Lambda_0}}\right)\ln\left(\frac{\left(2e(L-L_1)+\sqrt{-\Lambda_0}\right)\left(-\sqrt{-\Lambda_0}\right)}{\left(2e(L-L_1)-\sqrt{-\Lambda_0}\right)\left(\sqrt{-\Lambda_0}\right)}\right) \\
& \Lambda_0=-4e(a-c)
\end{aligned}
$$

$$
a=\left(\frac{K}{2\phi}\right)^{1/2}\frac{\gamma\cos\theta}{\mu};\quad b=\frac{W_2}{W_1}L_1;\quad c=\frac{F(W_1+T)}{\rho\phi W_1 T}L_1^{\,2};\quad e=\frac{F(W_2+T)}{\rho\phi W_2 T}
$$

Where, t is time, K is permeability, ϕ is porosity, μ is dynamic viscosity, And γ is surface tension, θ is contact angle, W_1 is the channel width at segment 1, W_2 is the channel width at segment 2, L_1 is the length of segment 1, F is the evaporation flux, T is the thickness of the paper, ρ is fluid density, and L is the distance from the reservoir of the imbibition front.

The implicit analytical relationship shown above is a model for imbibition in a two rectangular segment channel (similarly to an expansion or contraction channel seen in chapter 4). It incorporates evaporation. The above model simplifies two-dimensional flows by combining the coupled effects between two one-dimensional flows. Yet, even with this simplification the derived model is increasingly more complex than the traditional Lucas-Washburn equation. Therefore caution should be taken when creating analytical expressions. It would be best to accurately measure the physical properties of the paper, followed by numerical and computational simulations using a combination of, MATLAB, COMSOL Multiphysics, and ANSYS CFX. If creating a toolbox is desired that includes the effect of certain cross-sections, then this method will circumvent the need for an immense amount of imbibition experiments.

References

Beuther PD, Veith MW, Zwick KJ (2010) Characterization of Absorbent Flow Rate in Towel and Tissue J Eng Fiber Fabr 5:1-7

Bohm A, Carstens F, Trieb C, Schabel S, Biesalski M (2014) Engineering microfluidic papers: effect of fiber source and paper sheet properties on capillary-driven fluid flow Microfluid Nanofluid 16:789-799 doi:10.1007/s10404-013-1324-4

de Azevedo EN, Alme LR, Engelsberg M, Fossum JO, Dommersnes P (2008) Fluid imbibition in paper fibers: Precursor front Phys Rev E 78 doi:Artn 066317 10.1103/Physreve.78.066317

Fries N, Odic K, Conrath M, Dreyer M (2008) The effect of evaporation on the wicking of liquids into a metallic weave J Colloid Interf Sci 321:118-129 doi:Doi 10.1016/J.Jcis.2008.01.019

Hong S, Kim W (2015) Dynamics of water imbibition through paper channels with wax boundaries Microfluid Nanofluid 19:845-853 doi:10.1007/s10404-015-1611-3

Hyvaluoma J, Raiskinmaki P, Jasberg A, Koponen A, Kataja M, Timonen J (2006) Simulation of liquid penetration in paper Phys Rev E 73 doi:Artn 036705 10.1103/Physreve.73.036705

Lucas R (1918) The time law of the capillary rise of liquids. Kolloid-Zeitschrift 23:15-22 doi:Doi 10.1007/Bf01461107

Nassehi V, Das DB, Shigidi IMTA, Wakeman RJ (2011) Numerical analyses of bubble point tests used for membrane characterisation: model development and experimental validation Asia-Pac J Chem Eng 6:850-862 doi:10.1002/apj.519

Veran-Tissoires S, Marcoux M, Prat M (2012) Discrete Salt Crystallization at the Surface of a Porous Medium Phys Rev Lett 108 doi:Artn 054502 10.1103/Physrevlett.108.054502

Washburn EW (1921) The dynamics of capillary flow. Physical Review 17:273-283 doi:Doi 10.1103/Physrev.17.273

APPENDIX

Appendix A. Porosity of filter paper

The porosity of the surveyed paper (Table 3.1) was calculated using the basis weight, W_B, and thickness, T, as well as the density of cellulose fiber, ρ_c. The basis weight is the mass per unit area hence expressed as

$$W_B = \rho_c (1 - \phi) T \ .$$

The basis weight for the surveyed paper was calculated at RH = 3%. Solving for porosity ϕ,

$$\phi = 1 - \frac{W_B}{\rho_c T} \ .$$

Appendix B. Measurement of evaporated water mass

Rates of evaporation of water from sample paper pieces were recorded as described in the Materials and methods section. Fig. B.1 shows the time course of static evaporation for 6 different relative humidity values (18, 25, 50, 75, 90, and 99%). The slope of best fit line (evaporation rate) of each data set divided by the total surface area results in evaporation fluxes.

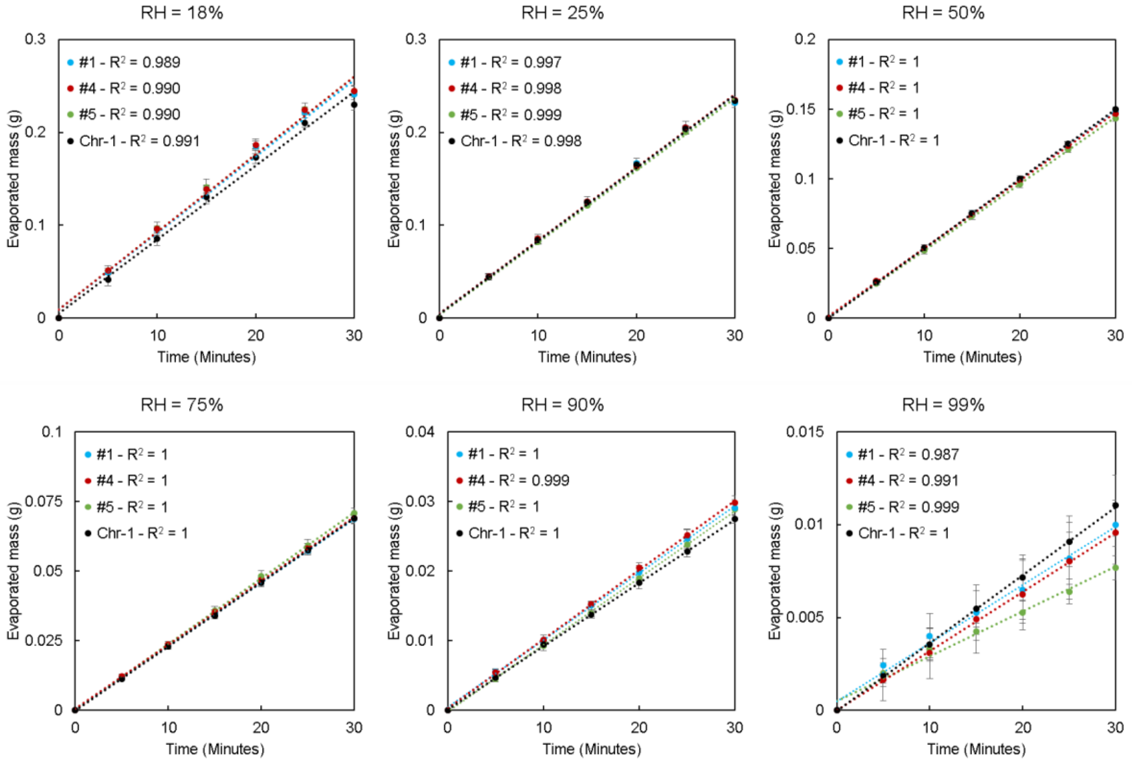

Fig. B.1 Static evaporation. Change of mass in paper strip over time of the surveyed paper types at different relative humidity. Data shown as mean ± SD (N = 5).

Appendix C. Residual water at different relative humidity

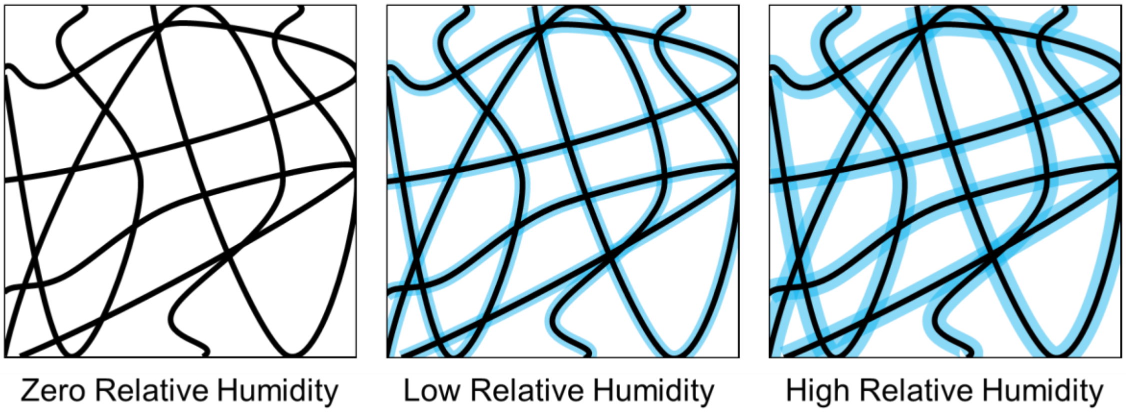

Fig. C.1 Illustration of water absorbed and retained by cellulose fibers in unwetted paper.

As illustrated in Fig. C.1, the paper increasingly absorbs and retains water vapor as the ambient relative humidity of air rises. Water saturation, S_w, is here defined as the volume fraction of the retained water in the available pore volume of the porous substrate (i.e. paper):

$$S_w = \frac{m_{rw}}{\rho \phi V_T},$$

where m_{rw} is mass of the retained water and V_T is the total volume of the paper.

At non-zero relative humidity, the fibers are pre-wetted due to the retained water. This effectively reduces the available pore volume for water from the reservoir to move through. Mathematically, this volume can be written as follows, and the factor of $(1-S_w)$ appears in Eq. F.2 accordingly:

$$\phi V_T - \frac{m_{rw}}{\rho} = \phi V_T\left(1 - \frac{m_{rw}}{\rho\phi V_T}\right) = \phi V(1 - S_w).$$

Appendix D. Scanning electron microscopy (SEM) of papers

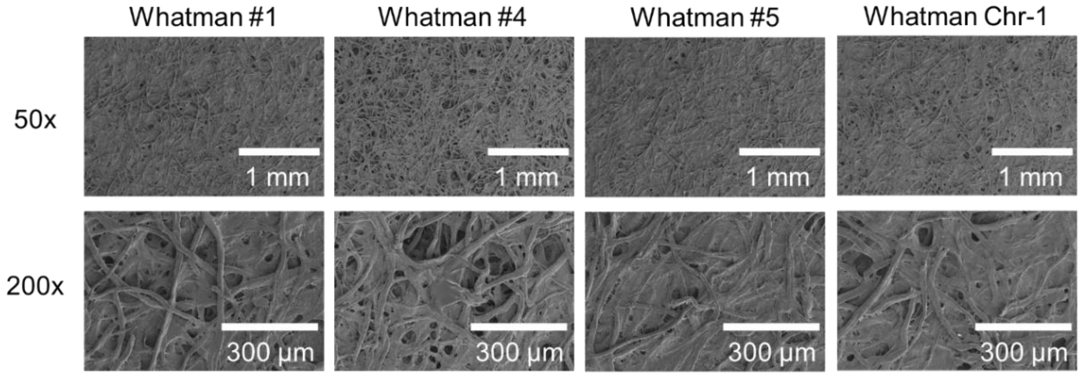

Fig. D.1 SEM images of the surveyed papers.

Appendix E. Measurement of imbibition front

Imbibition of water in the test devices was recorded as described in the Materials and methods section. To illustrate progression of the imbibition fronts in time, a time-lapse sequence is shown in Fig. E.1. Brightness of these images was adjusted in ImageJ to maximize visibility of the imbibition fronts. Imbibition distances vs. time for all paper types, channel widths, and relative humidity are plotted in Fig. E.2– E.5.

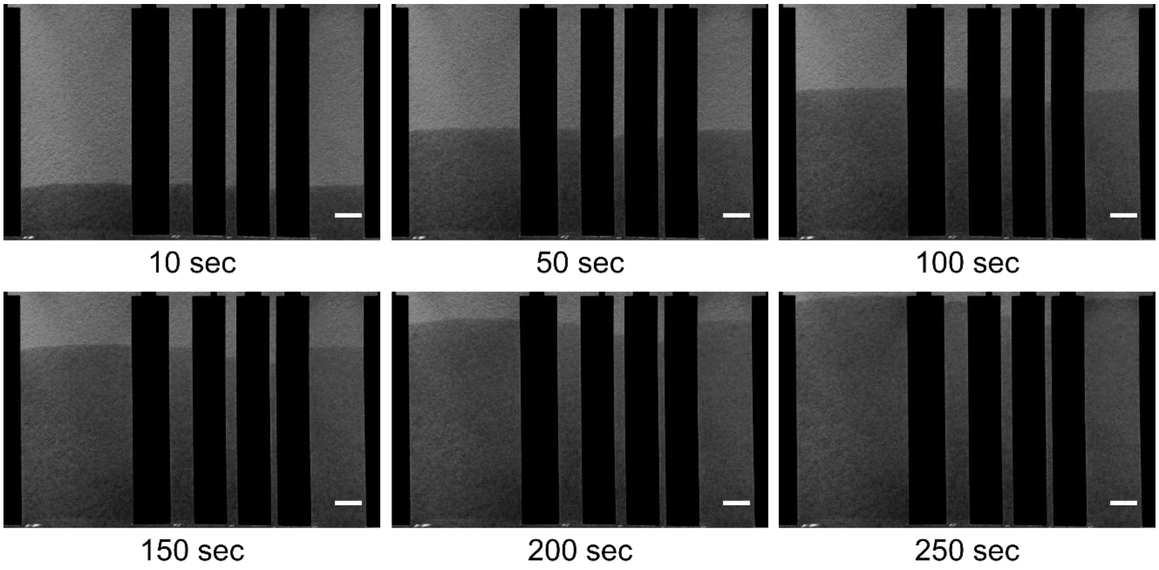

Fig. E.1 Time-lapse images of imbibition experiments of different channels Whatman #1 at 50% relative humidity. Scale bar: 5 mm.

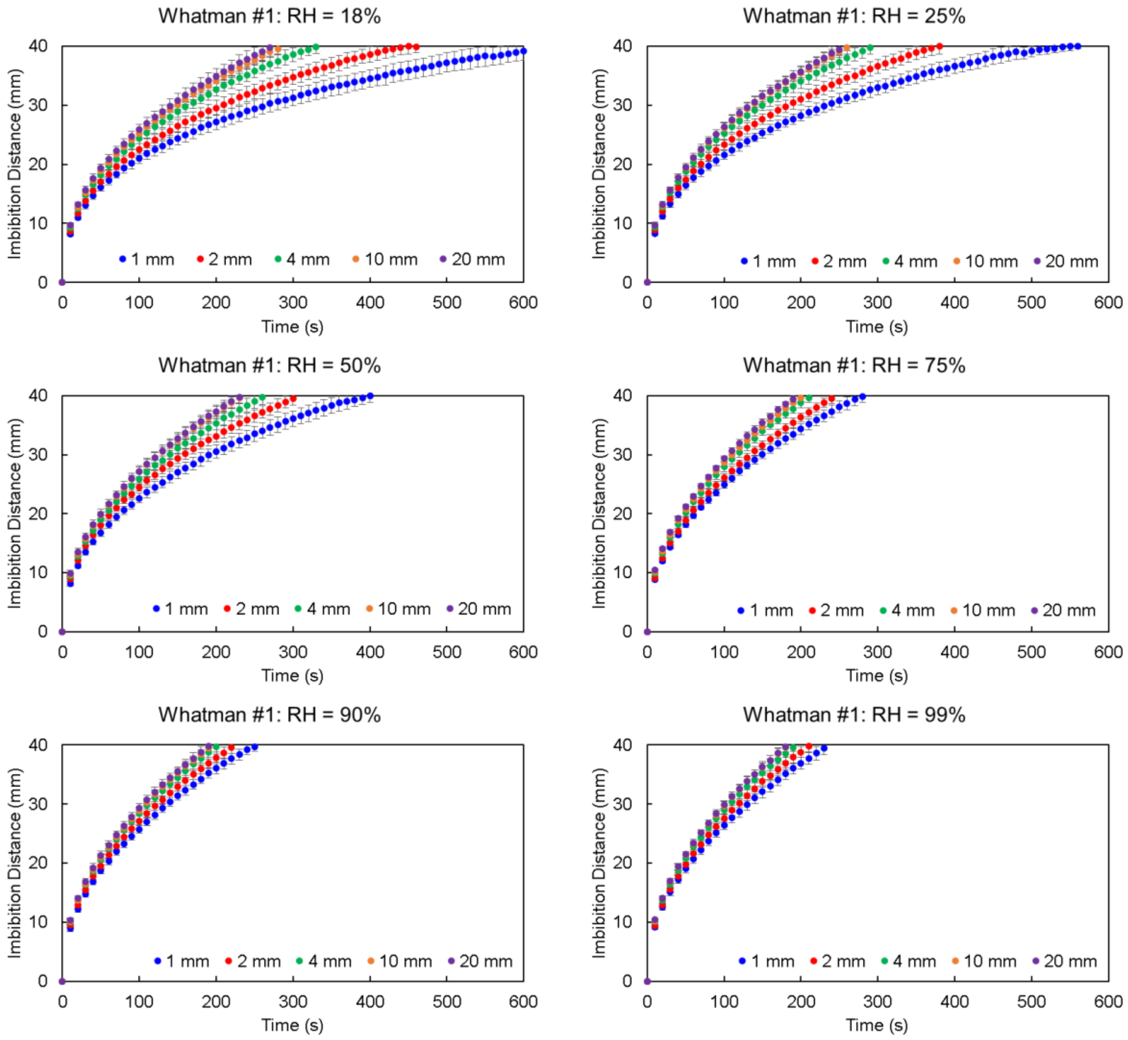

Fig. E.2 Imbibition distance vs. time of Whatman #1 at different relative humidity. Data shown as mean ± SD (N = 10).

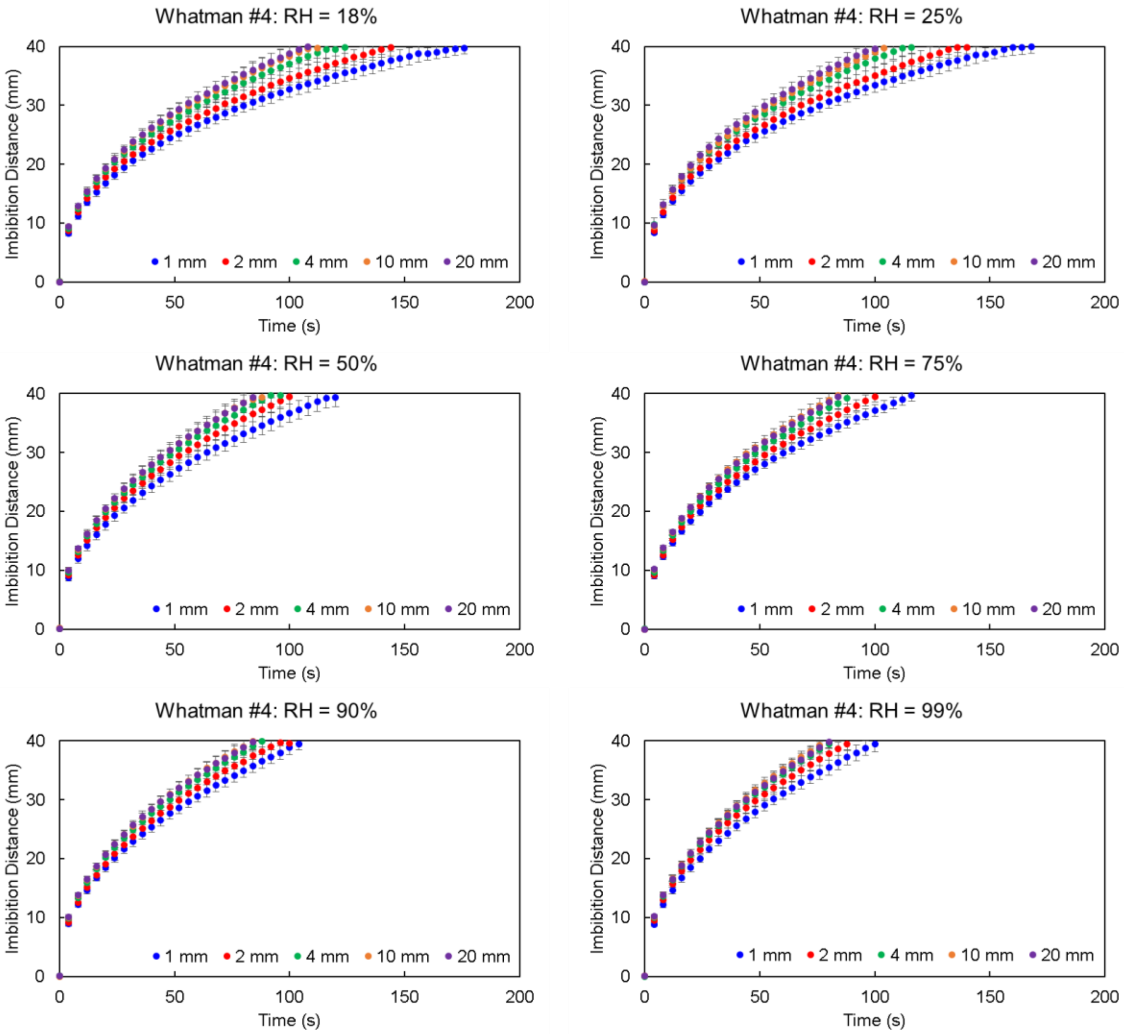

Fig. E.3 Imbibition distance vs. time of Whatman #4 at different relative humidity. Data shown as mean ± SD (N = 10).

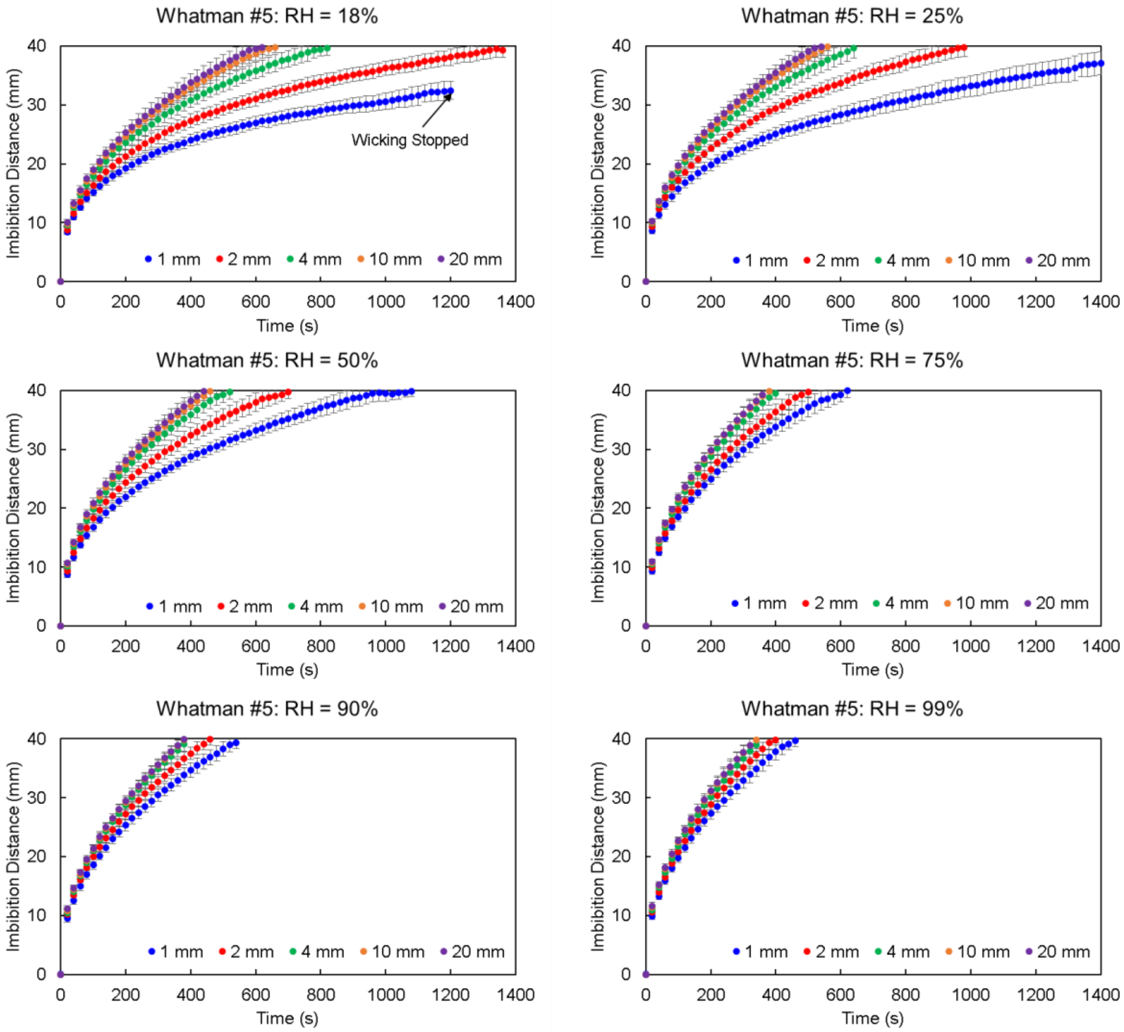

Fig. E.4 Imbibition distance vs. time of Whatman #5 at different relative humidity. Data shown as mean ± SD (N = 10).

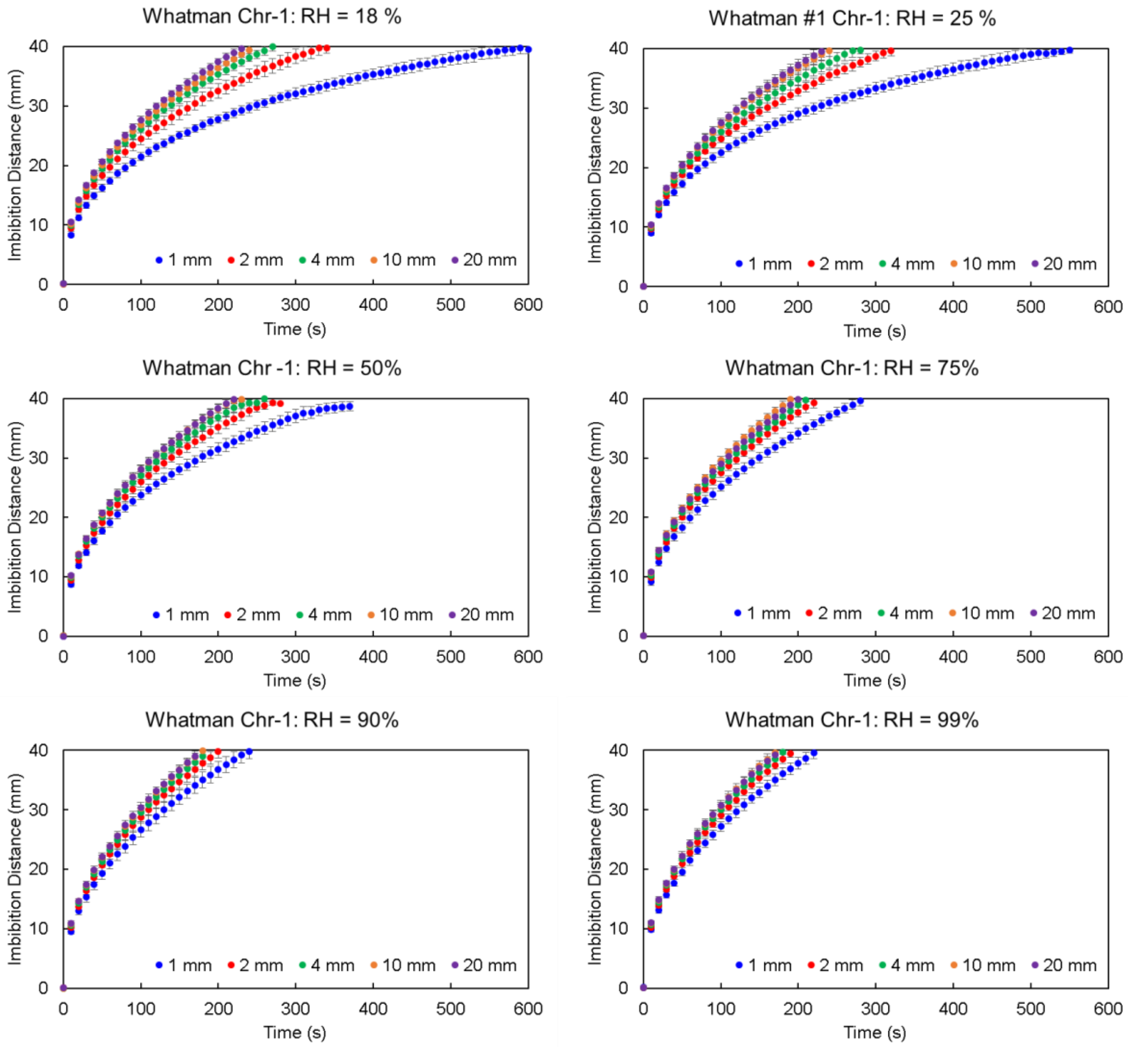

Fig. E.5 Imbibition distance vs time of Whatman Chr-1 at different relative humidity. Data shown as mean ± SD (N = 10).

Appendix F. Theory: Derivation of models

Fig. F.1 shows a schematic of a rectangular paper strip of width *W* and thickness *T*, into which a liquid (e.g., water) rises from an infinite reservoir. While the liquid wicks vertically, it evaporates laterally unless the surrounding atmosphere is fully saturated, in which case a dynamic equilibrium is reached.

Considering a small control volume of length Δy shown in Fig. F.1, the conservation of mass is written as,

$$\dot{M}_y\left(y-\frac{\Delta y}{2}\right)-\dot{M}_y\left(y+\frac{\Delta y}{2}\right)-2\dot{M}_x(y)-2\dot{M}_z(y)=0, \qquad \text{(F.1)}$$

where $\dot{M}_x, \dot{M}_y, \text{and } \dot{M}_z$ are the mass flow rates in the respective directions.

Assuming a flat imbibition front (i.e., 1-D flow), the mass flow rate in the vertical direction can be written as

$$\dot{M}_y(y)=\rho(1-S_w)v(y)W\,, \qquad \text{(F.2)}$$

where ρ is the density of the liquid, S_w is the water saturation of the paper matrix, and $v(y)$ is the vertical flow speed. Here, $(1-S_w)$ is factored in because the cellulose fibers of paper are hygroscopic and absorb water vapor from the atmosphere.

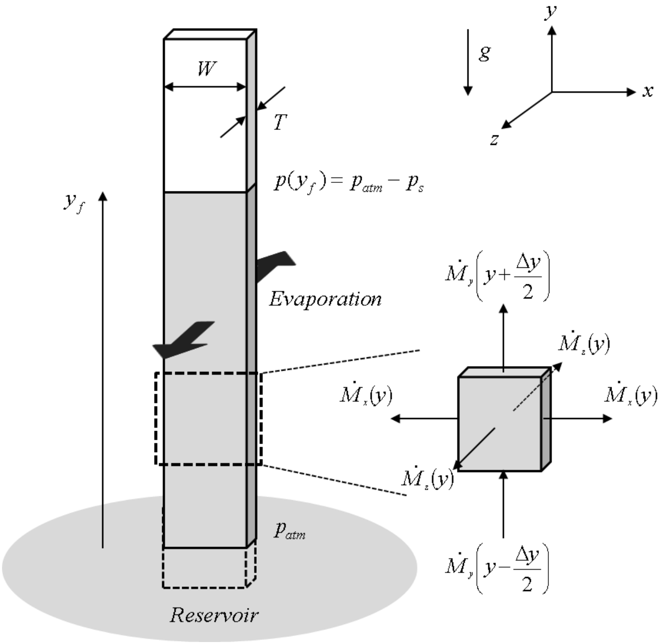

Fig. F.1 Schematic of liquid imbibition in a paper channel.

Similarly, assuming uniform evaporation from the wetted surfaces, the mass flow rates in the lateral directions are written as

$$\dot{M}_x(y) = FT\Delta y, \text{and } \dot{M}_z(y) = FW\Delta y\,, \tag{F.3}$$

where F is the evaporation flux. Unlike the mass flow rate in y direction, those in x and z directions do not include $(1 - S_w)$. This is because F, usually measured experimentally or calculated from experimentally fitted models, takes the effects of the water saturation into account by default.

Substituting Eq. F.2 and F.3 into Eq. F.1 and dividing by Δy, the mass balance is expressed as

$$\left[\frac{v\left(y+\frac{\Delta y}{2}\right)-v\left(y-\frac{\Delta y}{2}\right)}{\Delta y}\right]\rho(1-S_w)WT=-2F(W+T). \tag{F.4}$$

Dividing both sides by $\rho(1-S_w)WT$ and taking the limit of $\Delta y \to 0$, the following differential equation is obtained:

$$\frac{dv}{dy}=-\frac{2F(W+T)}{\rho(1-S_w)WT}. \tag{F.5}$$

Flow velocity in a porous medium is also described by Darcy's law, which is a form of conservation of momentum. For the 1-D flow in the paper strip, it is written as

$$v(y)=-\frac{K}{\mu}\left(\frac{dp}{dy}+\rho g\right), \tag{F.6}$$

where K is the permeability, μ is the dynamic viscosity of water, p is the pressure, and g is the gravitational acceleration. Differentiating once, Eq. F.6 becomes

$$\frac{dv}{dy}=-\frac{K}{\mu}\frac{d^2p}{dy^2}. \tag{F.7}$$

Equating the right hand sides of Eq. F.5 and F.7 and dividing by $-K/\mu$, a 2nd-order differential equation of pressure is obtained:

$$\frac{d^2 p}{dy^2} = \frac{\mu}{K} \frac{2F(W+T)}{\rho(1-S_w)WT}. \qquad \text{(F.8)}$$

Integrating twice and applying two pressure boundary conditions ($p = p_{atm}$ at $y = 0$ and $p = p_{atm} - p_s$ at $y = y_f$, where p_{atm} and p_s are the atmospheric pressure and the capillary suction pressure, respectively) yields,

$$p = \frac{\mu}{K} \frac{F(W+T)}{\rho(1-S_w)WT} y^2 - \left[\frac{p_s}{y_f} + \frac{\mu}{K} \frac{F(W+T)}{\rho(1-S_w)WT} y_f \right] y + p_{atm}. \qquad \text{(F.9)}$$

This expression is then used to evaluate dp/dy at the imbibition front ($y = y_f$),

$$\left. \frac{dp}{dy} \right|_{y=y_f} = \frac{\mu}{K} \frac{F(W+T)}{\rho(1-S_w)WT} y_f - \frac{p_s}{y_f}. \qquad \text{(F.10)}$$

Substituting Eq. F.10 into Eq. F.6 evaluated at the front ($y = y_f$) and recognizing $v(y_f) = \phi v_c(y_f) = \phi dy_f/dt$, where ϕ and v_c are porosity and interstitial velocity respectively, one finds

$$\phi \frac{dy_f}{dt} = \frac{K}{\mu} \frac{p_s}{y_f} - \frac{F(W+T)}{\rho(1-S_w)WT} y_f - \frac{K\rho g}{\mu}. \qquad \text{(F.11)}$$

Dividing by ϕ, Eq. F.11 is simplified as

$$\frac{dy_f}{dt} = \frac{a}{y_f} - b y_f - c, \qquad \text{(F.12)}$$

where $a = \dfrac{4K\gamma\cos\theta}{\phi\mu D_e}, b = \dfrac{F(W+T)}{\phi\rho(1-S_w)WT}$, and $c = \dfrac{K\rho g}{\phi\mu}$.

In the above expression, the capillary suction pressure is defined as,

$$p_s = \frac{4\gamma \cos\theta}{D_e}, \tag{F.13}$$

where γ is the surface tension of the liquid, θ is the liquid-solid contact angle, and D_e is the effective diameter, an equivalent of the diameter in the capillary tube model.

Furthermore, the permeability K and the diameter D_e can be related as follows by comparing the Darcy's law and Hagen-Poiseuille law:

$$K = \frac{\phi D_e^{\ 2}}{32}. \tag{F.14}$$

The solution form of Eq. F.12 is found elsewhere and with the initial condition of $y_f = 0$ at $t = 0$, it is implicitly given as

$$t = -\frac{1}{2b}\ln\left(\frac{-by_f^2 - cy_f + a}{a}\right) - \frac{c}{2b\sqrt{-\Psi}}\ln\left[\frac{\left(2by_f + c + \sqrt{-\Psi}\right)\left(c - \sqrt{-\Psi}\right)}{\left(2by_f + c - \sqrt{-\Psi}\right)\left(c + \sqrt{-\Psi}\right)}\right], \tag{F.15}$$

where $\Psi = -4ab - c^2$.

Eq. F.15 provides an implicit solution of imbibition distance which makes the model inconvenient. It is commonly understood that the effect of gravity is negligible during imbibition up to 10% of the equilibrium height. Inspecting the

Bond number (10-8≪1) which quantifies the ratio between body force to surface tension force adds support to this claim.

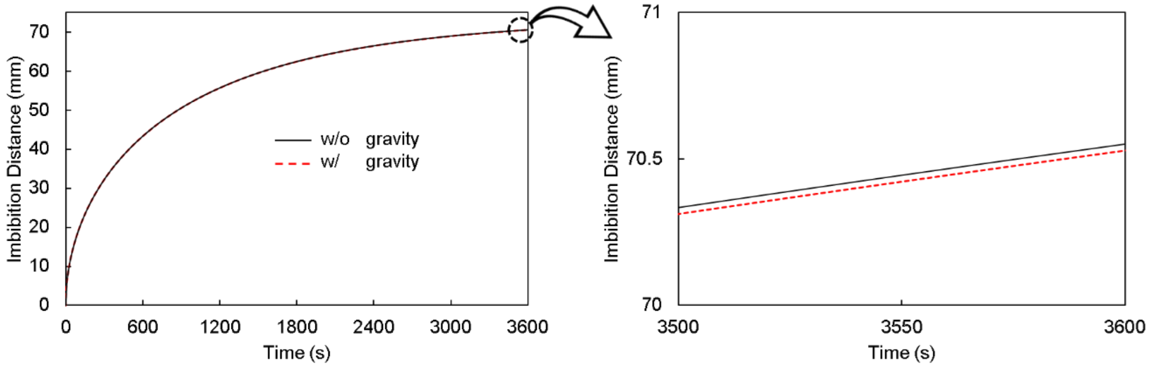

Fig. F.2 Comparison of the developed model with or without gravity.

Comparing the model with and without gravity (Fig. F.2) shows the difference between the equations of only 30 μm or 0.0425% after 1 hour of imbibition for a 2 mm channel at RH = 50%. These results strongly support that the effects of gravity is negligible and that Eq. F.17 provides sufficient results. Therefore if the effect of gravity is neglected (i.e., $c = 0$), Eq. F.15 becomes

$$t = -\frac{1}{2b}\ln\left(\frac{-by_f^{2}+a}{a}\right) \tag{F.16}$$

or

$$y_f = \left[\frac{a - a\exp(-2bt)}{b}\right]^{\frac{1}{2}} . \tag{F.17}$$

When effects of both gravity and evaporation are neglected (i.e., $c = 0$ and $b = 0$), and Eq. F.14 is used, the solution of Eq. F.12 simplifies to the Lucas-Washburn equation:

$$y_f = \sqrt{\frac{D_e \gamma \cos\theta}{4\mu} t} . \tag{F.18}$$

Alternatively, if Eq. F.14 is used the term ‘a’ can be written as,

$$a = \left(\frac{K}{2\phi}\right)^{1/2} \frac{\gamma \cos\theta}{\mu}$$

With Eq. F.18 becoming,

$$y_f = \sqrt{\left(\left(\frac{2K}{\phi}\right)^{1/2} \frac{\gamma \cos\theta}{\mu} t\right)} \tag{F.19}$$

In the current study, perfect wetting was assumed ($\theta = 0^\circ$).

Our current model, without gravity, is derived based on the following assumptions: 1) Overall dimensions of the channel do not change before and after imbibition (i.e., no bulk swelling of paper); 2) Inertia effects are neglected by the use of Darcy’s law; 3) Wetting of paper is binary (fully saturated when wetted, and S_w when unwetted; 4) Evaporation flux of the wetted surface is uniform and solely depends on relative humidity; 5)

Imbibition front is flat; 6) Contact angle θ is zero and independent of relative humidity; and 7) Gravity is neglected. One may critique that some of these assumptions are neglecting potentially important effects. For example, some studies reported importance of inertia effects at the onset of imbibition, or change of θ over time. Nevertheless, these assumptions are required in order to derive the simple, explicit, and powerful model expressed in Eq. F.17 and compare side by side with the L-W model and Fries et al. model.

Appendix G. Slopes and y-intercepts from effective permeability vs RH plots

Table G.1 Lucas-Washburn model. Slopes and y-intercepts corresponding to Fig. 3.6.

Paper type	**Slope x10^{-15} (m^2/RH)**	**y-intercept x10^{-15} (m^2)**				
		Channel width				
		1 mm	***2 mm***	***4 mm***	***10 mm***	***20 mm***
Whatman #1	0.0260	-0.059	0.471	1.066	1.510	1.608
Whatman #4	0.1144	3.437	6.257	9.890	11.690	11.767
Whatman #5	0.0093	-0.219	-0.072	0.133	0.270	0.296
Whatman Chr-	0.0271	0.003	0.953	1.485	1.985	1.992

Table G.2 Fries et al. model. Slopes and y-intercepts corresponding to Fig. 3.7.

Paper type	**Slope x10^{-15} (m^2/RH)**	**y-intercept x10^{-15} (m^2)**				
		Channel width				
		1 mm	***2 mm***	***4 mm***	***10 mm***	***20 mm***
Whatman #1	0.0231	0.223	0.765	1.373	1.828	1.925
Whatman #4	0.1077	4.105	6.934	10.594	12.405	12.479
Whatman #5	0.0082	-0.115	0.037	0.259	0.401	0.428
Whatman Chr-	0.0239	0.301	1.270	1.821	2.330	2.354

Table G.3 Water saturation model. Slopes and y-intercepts corresponding to Fig. 3.8.

Paper type	**Slope x10^{-15} (m^2/RH)**	**y-intercept x10^{-15} (m^2)**				
		Channel width				
		1 mm	***2 mm***	***4 mm***	***10 mm***	***20 mm***
Whatman #1	0.0231	0.223	0.768	1.375	1.830	1.926
Whatman #4	0.1076	4.118	6.946	10.604	12.416	12.491
Whatman #5	0.0081	-0.105	0.057	0.277	0.411	0.439
Whatman Chr-	0.0241	0.293	1.254	1.825	2.320	2.330

Appendix H. R^2 values of effective permeability of surveyed paper types

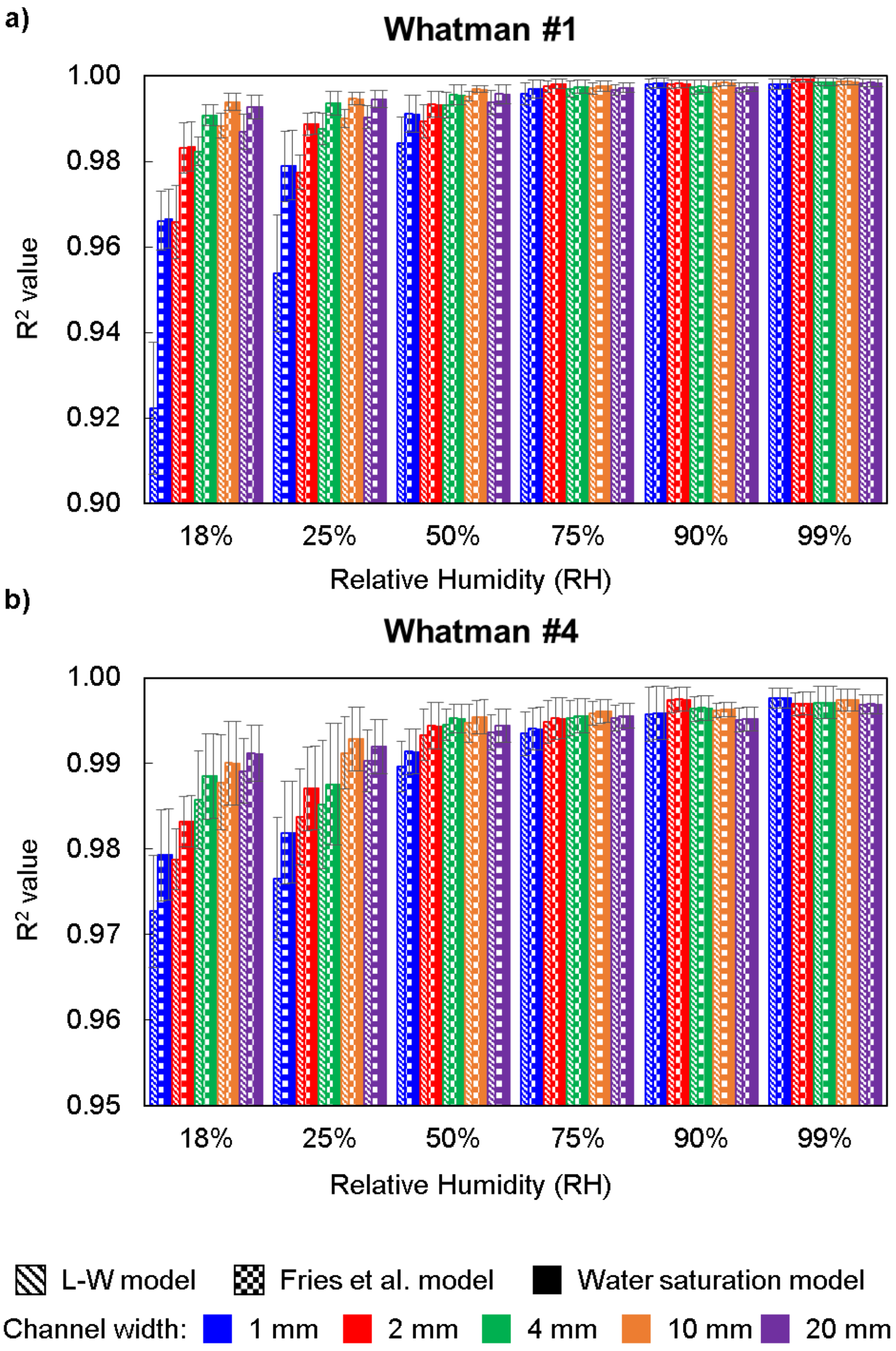

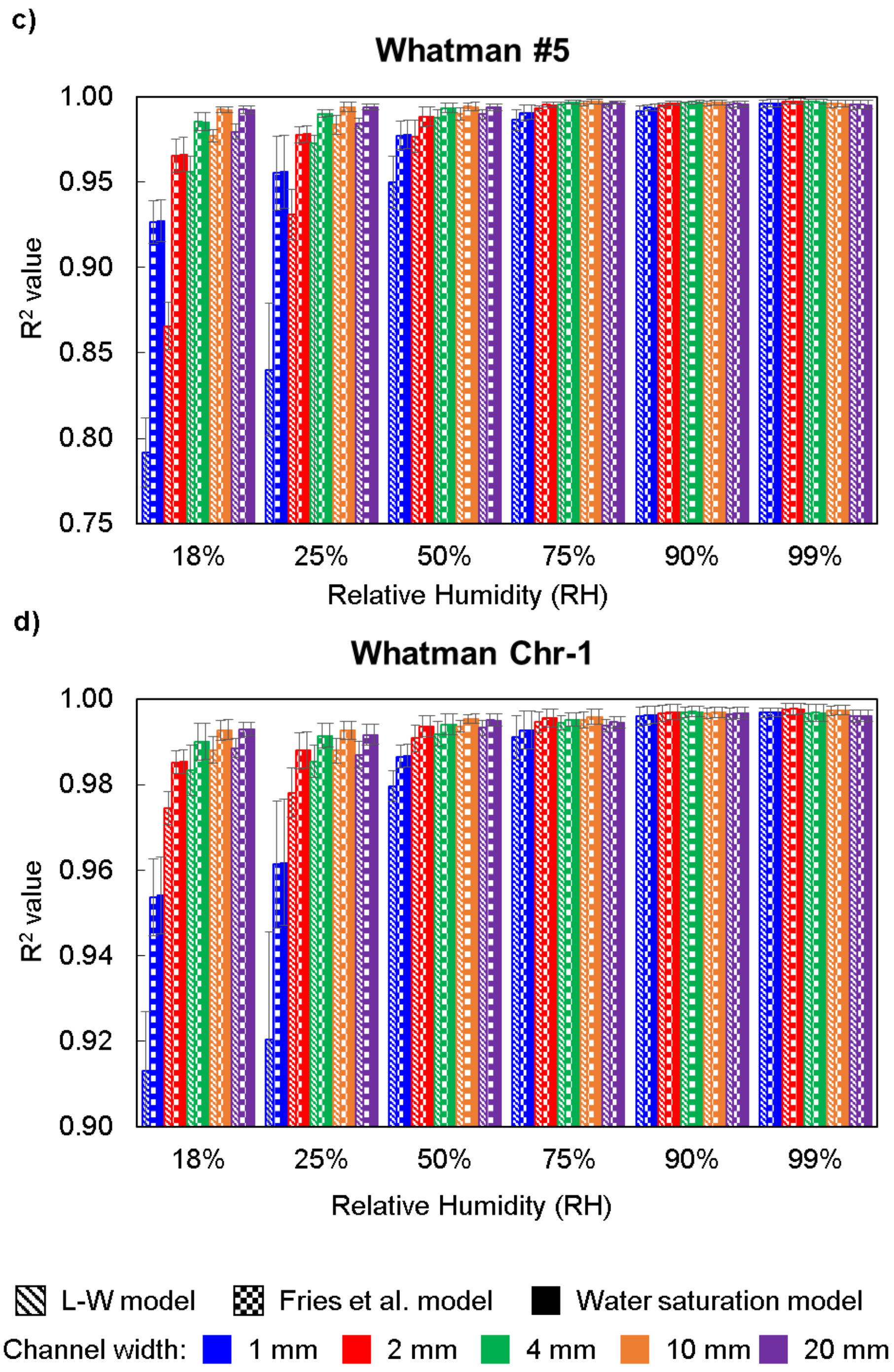

Fig. H.1 R^2 values of effective permeability of surveyed paper types at various relative humidity for L-W model, Fries et al. model, and the water saturation model. a) Whatman #1, b) Whatman #4, c) Whatman #5, and d) Whatman Chr-1. Data shown as mean ± SD (N = 10).

Appendix I.   Wax expansion

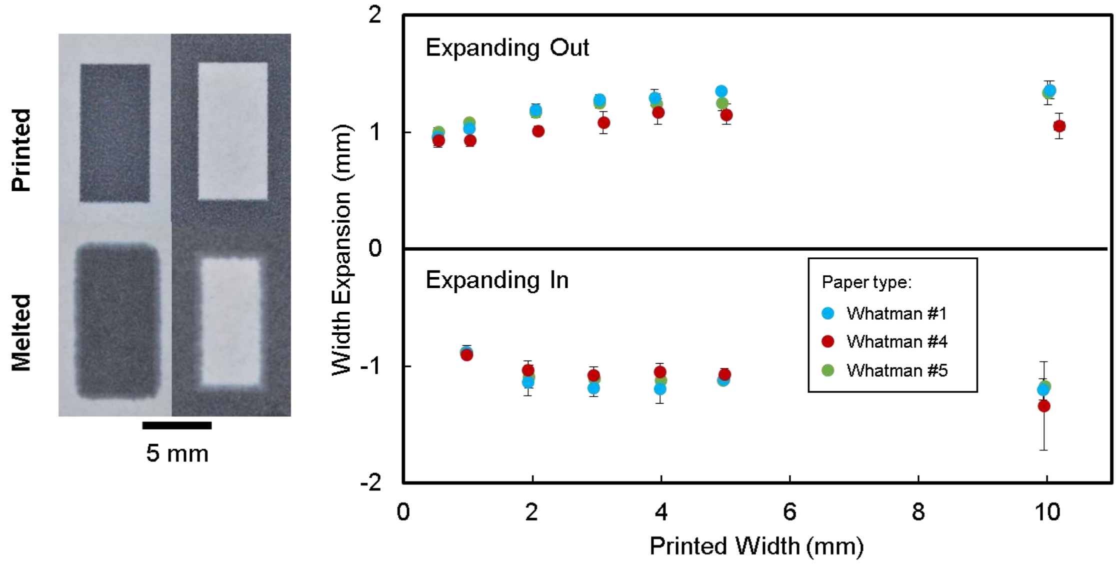

Fig. I.1 Wax expansion plot. Expansion of wax vs printed dimensions.

Appendix J. Theory: Imbibition in a channel with multiple sections

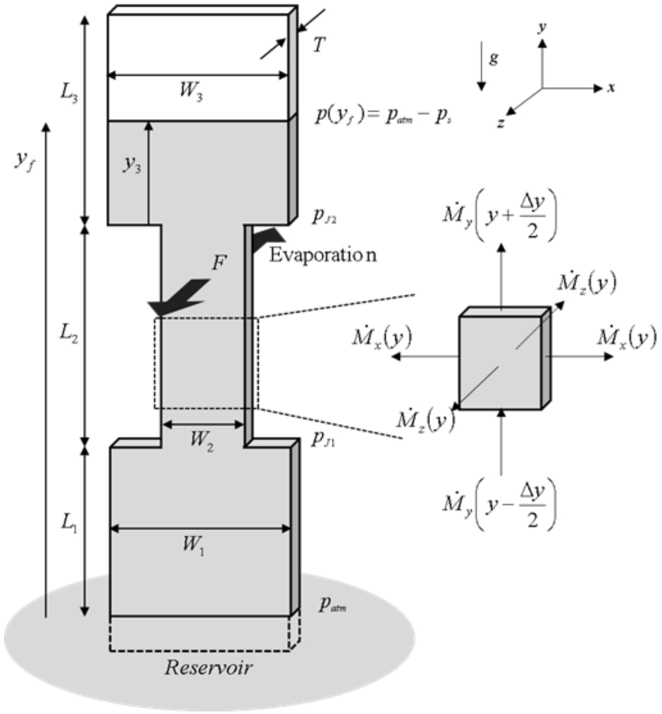

Fig. J.1 Schematic of liquid imbibition in a multi-channel.

Flow in porous media is described by the mass conservation and Darcy's law.

$$\frac{\partial}{\partial t}\int_V \rho dV = -\int_s \rho \vec{V} \cdot \vec{n} dS + q \tag{J.1}$$

$$\vec{v} = -\frac{k}{\mu}\left(\nabla P - \rho \vec{g}\right) \tag{J.2}$$

Here we look at a porous channel that contain a sudden rectangular change in cross section. We take the porous strip to be constant in thickness, *T*, and a constant mass flux (mass/second-area) due to evaporation, *F*.

Assuming incompressible flow, the mass conservation of the second segment can be written as,

$$\dot{M}_y - \dot{M}_y(y+\Delta y) - 2\dot{M}_z - 2\dot{M}_x = 0$$

Similarly to the constant-width channel, the mass conservation can be represented as,

$$\frac{dV_2(y)}{dy_2} = \frac{-2F(W_2+T)}{\rho W_2 T} \tag{J.3}$$

Taking the derivative of Eq. J.2 in the vertical direction with respect to y_2,

$$\frac{dV_2(y)}{dy_2} = -\frac{k}{\mu}\frac{d^2P_2}{dy_2{}^2} \tag{J.4}$$

Substituting Eq. J.4 into Eq. J.3 and solving for the pressure with boundary conditions:

$P_2 = P_{J1}$ @ $y_2 = 0$

$P_2 = P_{atm} - P_s$ @ $y_2 = y_{2f}$

The pressure becomes,

$$P_2 = \frac{F\mu(W_2+T)}{\rho W_2 Tk} y_2{}^2 + \left[\frac{P_{atm} - P_s - P_{J1}}{y_{2f}} - \frac{F\mu(W_2+T)}{\rho W_2 Tk} y_{2f}\right] y_2 + P_{J1} \tag{J.5}$$

Evaluating the gradient at y_{2f},

$$\left.\frac{dP_2}{dy_2}\right|_{y2f} = \frac{F\mu(W_2 + T)}{\rho W_2 Tk} y_{2f} + \frac{P_{atm} - P_s - P_{J1}}{y_{2f}} \tag{J.6}$$

Substituting back into Eq. J.2

$$V_2 = -\frac{k}{\mu}\left(\frac{F\mu(W_2 + T)}{\rho W_2 Tk} y_{2f} + \frac{P_{atm} - P_s - P_{J1}}{y_{2f}} + \rho g\right) \tag{J.7}$$

Rearranging,

$$P_{atm} - P_s - P_{J1} = -y_{2f}\left(\frac{\mu V_2}{k} + \frac{F\mu(W_2 + T)}{\rho W_2 Tk} y_{2f} + \rho g\right) \tag{J.8}$$

We know at the junction the flow rates must be identical,

$$V_1 W_1 T = V_2 W_2 T$$

$$V_1 = \frac{W_2}{W_1} V_2$$

From the constant-width analysis, the V_1 evaluate at the junction L_1, becomes,

$$V_1 = -\frac{k}{\mu}\left(\frac{F\mu(W_1 + T)}{\rho W_1 Tk} L_1 + \frac{P_{J1} - P_{atm}}{L_1} + \rho g\right)$$

(J.9)

Substituting the velocity relationship,

$$-\frac{k}{\mu}\left(\frac{F\mu(W_1+T)}{\rho W_1 Tk}L_1+\frac{P_{J1}-P_{atm}}{L_1}+\rho g\right)=\frac{W_2}{W_1}V_2 \tag{J.10}$$

Rearranging,

$$L_1\left(\frac{\mu W_2}{kW_1}V_2+\frac{F\mu(W_1+T)}{\rho W_1 Tk}L_1+\rho g\right)=P_{atm}-P_{J1} \tag{J.11}$$

Substituting Eq. J.11 into Eq. J.8,

$$L_1\left(\frac{\mu W_2}{kW_1}V_2+\frac{F\mu(W_1+T)}{\rho W_1 Tk}L_1+\rho g\right)-P_s=-y_{2f}\left(\frac{\mu V_2}{k}+\frac{F\mu(W_2+T)}{\rho W_2 Tk}y_{2f}+\rho g\right) \tag{J.12}$$

Therefore solving for *Ps*,

$$P_s=\left(\frac{\mu W_2}{kW_1}L_1V_2+\frac{F\mu(W_1+T)}{\rho W_1 Tk}L_1{}^2+\rho gL_1\right)+\left(\frac{\mu}{k}y_{2f}V_2+\frac{F\mu(W_2+T)}{\rho W_2 Tk}y_{2f}{}^2+\rho gy_{2f}\right) \tag{J.13}$$

Multiplying both sides by *k/μ* and substituting the interstitial velocity,

$$\begin{gathered}\frac{kP_s}{\mu}=\left(\frac{W_2}{W_1}L_1\phi\frac{dy_{2f}}{dt}+\frac{F(W_1+T)}{\rho W_1 T}L_1{}^2+\frac{k\rho gL_1}{\mu}\right)+\\ \left(\frac{\mu}{k}y_{2f}\phi\frac{dy_{2f}}{dt}+\frac{F(W_2+T)}{\rho W_2 T}y_{2f}{}^2+\frac{k\rho gy_{2f}}{\mu}\right)\end{gathered} \tag{J.14}$$

Dividing by the porosity,

$$\frac{kP_s}{\phi\mu} = \left(\frac{W_2}{W_1} L_1 \frac{dy_{2f}}{dt} + \frac{F(W_1+T)}{\rho\phi W_1 T} L_1^{\;2} + \frac{k\rho g L_1}{\phi\mu}\right) + \left(y_{2f}\frac{dy_{2f}}{dt} + \frac{F(W_2+T)}{\rho\phi W_2 T} y_{2f}^{\;2} + \frac{k\rho g y_{2f}}{\phi\mu}\right) \qquad \text{(J.15)}$$

With $\frac{k}{\phi} = \frac{D_e^{\;2}}{32}$ and letting,

$$a = \frac{kP_s}{\phi\mu} = \frac{D_e^{\;2} P_s}{32\mu} \quad \text{Where, } P_s = \frac{4\gamma\cos\theta}{D_e}$$

$$b = \frac{W_2}{W_1} L_1$$

$$c = \frac{F(W_1+T)}{\rho\phi W_1 T} L_1^{\;2}$$

$$d = \frac{k\rho g L_1}{\phi\mu} = \frac{D_e^{\;2}\rho g L_1}{32\mu}$$

$$e = \frac{F(W_2+T)}{\rho\phi W_2 T}$$

$$f = \frac{k\rho g}{\phi\mu} = \frac{D_e^{\;2}\rho g}{32\mu}$$

Eq. J.15 becomes,

$$a = b\frac{dy_{2f}}{dt_2} + c + d + y_{2f}\frac{dy_{2f}}{dt} + e y_{2f}^{\;2} + f y_{2f} \qquad \text{(J.16)}$$

The differential equation can be solved by rearranging and integrating both sides,

$$\int \frac{b + y_{2f}}{a - c - d - e{y_{2f}}^2 - fy_{2f}} dy_{2f} = \int dt_2 \tag{J.17}$$

Note: From Handbook of Mathematics, Bronstein, 5th edition pg. 1025

$$X = ax^2 + bx + c$$
$$\Lambda = 4ac - b^2$$
$$\int \frac{x}{X} dx = \frac{1}{2a} \ln X - \frac{b}{2a} \int \frac{1}{X} dx$$
$$\int \frac{1}{X} dx = \frac{1}{\sqrt{-\Lambda}} \ln \left(\frac{2ax + b - \sqrt{-\Lambda}}{2ax + b + \sqrt{-\Lambda}} \right)$$

Therefore,

$$\begin{aligned} t_2 &= \int \frac{y_{2f}}{(-e){y_{2f}}^2 + (-f)y_{2f} + (a - c - d)} dy_{2f} + \\ &\int \frac{b}{(-e){y_{2f}}^2 + (-f)y_{2f} + (a - c - d)} dy_{2f} \end{aligned} \tag{J.18}$$

Letting

$$Y = (-e){y_{2f}}^2 + (-f)y_{2f} + (a - c - d)$$
$$\Lambda = -4e(a - c - d) - f^2$$

Eq. J.18 becomes,

$$\begin{aligned} t_2 &= \frac{1}{2(-e)} \ln Y - \frac{(-f)}{2(-e)} \frac{1}{\sqrt{-\Lambda}} \ln \left(\frac{2(-e)y_{2f} + (-f) - \sqrt{-\Lambda}}{2(-e)y_{2f} + (-f) + \sqrt{-\Lambda}} \right) \\ &+ \frac{b}{\sqrt{-\Lambda}} \ln \left(\frac{2(-e)y_{2f} + (-f) - \sqrt{-\Lambda}}{2(-e)y_{2f} + (-f) + \sqrt{-\Lambda}} \right) + C \end{aligned} \tag{J.19}$$

Or

$$t_2 = \frac{1}{2e}\ln\left(\frac{1}{Y}\right) + \left(\frac{b}{\sqrt{-\Lambda}} - \frac{f}{2e\sqrt{-\Lambda}}\right)\ln\left(\frac{2ey_{2f} + f + \sqrt{-\Lambda}}{2ey_{2f} + f - \sqrt{-\Lambda}}\right) + C \qquad \text{(J.20)}$$

Initial condition of $y_{2f} = 0$ @ $t_2 = 0$ gives C as,

$$C = \frac{1}{2e}\ln\left(a - c - d\right) - \left(\frac{b}{\sqrt{-\Lambda}} - \frac{f}{2e\sqrt{-\Lambda}}\right)\ln\left(\frac{f + \sqrt{-\Lambda}}{f - \sqrt{-\Lambda}}\right) \qquad \text{(J.21)}$$

Substituting back into Eq. J.20,

$$\begin{aligned} t_2 = {} & \frac{1}{2e}\ln\left(\frac{-a + c + d}{ey_{2f}^{\,2} + fy_{2f} - a + c + d)}\right) + \\ & \left(\frac{b}{\sqrt{-\Lambda}} - \frac{f}{2e\sqrt{-\Lambda}}\right)\ln\left(\frac{\left(2ey_{2f} + f + \sqrt{-\Lambda}\right)\left(f - \sqrt{-\Lambda}\right)}{\left(2ey_{2f} + f - \sqrt{-\Lambda}\right)\left(f + \sqrt{-\Lambda}\right)}\right) \end{aligned} \qquad \text{(J.22)}$$

Next we switch to global coordinates (l,t) by substituting $y_{2f} = L\text{-}L_1$ and $t_2 = t\text{-}t_1$ into Eq. J.22. First we need to manipulate t_1. Taking take t_1 from that of the constant width channel, where $y_f = L_1$.

$$t_1 = \frac{1}{2b_1}\ln\left(\frac{a_1}{-b_1L_1^{\,2} - c_1L_1 + a_1}\right) - \frac{c_1}{2b_1\sqrt{-\Delta_1}}\ln\left(\frac{\left(-2b_1L_1 - c_1 - \sqrt{-\Delta_1}\right)\left(-c_1 + \sqrt{-\Delta_1}\right)}{\left(-2b_1L_1 - c_1 + \sqrt{-\Delta_1}\right)\left(-c_1 - \sqrt{-\Delta_1}\right)}\right)$$

$$a_1 = \frac{kP_s}{\phi\mu} = a$$

$$b_1 = \frac{F\left(W_1 + T\right)}{\rho W_1 T\phi} = \frac{c}{L_1^{\;2}}$$

$$c_1 = \frac{k\rho g}{\phi\mu} = \frac{d}{L_1} = f$$

$$\Delta_1 = -\left(4a_1 b_1 - c_1^{\;2}\right) = -\left(4a\frac{c}{L_1^{\;2}} - f^{\,2}\right) = -\left(4a\frac{c}{L_1^{\;2}} - \frac{d^{\,2}}{L_1^{\;2}}\right) = -\frac{1}{L_1^{\;2}}\left(4ac - d^{\,2}\right)$$

Substituting out the *a₁*, *b₁*, *c₁*,

$$t_1 = \frac{L_1^{\;2}}{2c}\ln\left(\frac{a}{-\frac{c}{L_1^{\;2}}L_1^{\;2} - \frac{d}{L_1}L_1 + a}\right) - \frac{\frac{d}{L_1}}{2\frac{c}{L_1^{\;2}}\sqrt{-\Delta_1}}\ln\left(\frac{\left(-2\frac{c}{L_1^{\;2}}L_1 - \frac{d}{L_1} - \sqrt{-\Delta_1}\right)\left(-\frac{d}{L_1} + \sqrt{-\Delta_1}\right)}{\left(-2\frac{c}{L_1^{\;2}}L_1 - \frac{d}{L_1} + \sqrt{-\Delta_1}\right)\left(-\frac{d}{L_1} - \sqrt{-\Delta_1}\right)}\right)$$

Taking $\sqrt{-\Delta_1} = \frac{1}{L_1}\sqrt{4ac - d^{\,2}}$

$$t_1 = \frac{L_1^{\;2}}{2c}\ln\left(\frac{a}{-\frac{c}{L_1^{\;2}}L_1^{\;2} - \frac{d}{L_1}L_1 + a}\right) -$$

$$\frac{\frac{d}{L_1}}{2\frac{c}{L_1^{\;2}}\frac{1}{L_1}\sqrt{4ac - d^{\,2}}}\ln\left(\frac{\left(-2\frac{c}{L_1^{\;2}}L_1 - \frac{d}{L_1} - \frac{1}{L_1}\sqrt{4ac - d^{\,2}}\right)\left(-\frac{d}{L_1} + \frac{1}{L_1}\sqrt{4ac - d^{\,2}}\right)}{\left(-2\frac{c}{L_1^{\;2}}L_1 - \frac{d}{L_1} + \frac{1}{L_1}\sqrt{4ac - d^{\,2}}\right)\left(-\frac{d}{L_1} - \frac{1}{L_1}\sqrt{4ac - d^{\,2}}\right)}\right)$$

Cancelling terms,

$$t_1 = \frac{L_1^{\ 2}}{2c}\ln\left(\frac{a}{-c-d+a}\right) -$$

$$\frac{L_1^{\ 2}d}{2c\sqrt{4ac-d^2}}\ln\left(\frac{\left(-2\frac{c}{L_1}-\frac{d}{L_1}-\frac{1}{L_1}\sqrt{4ac-d^2}\right)\left(-\frac{d}{L_1}+\frac{1}{L_1}\sqrt{4ac-d^2}\right)}{\left(-2\frac{c}{L_1}-\frac{d}{L_1}+\frac{1}{L_1}\sqrt{4ac-d^2}\right)\left(-\frac{d}{L_1}-\frac{1}{L_1}\sqrt{4ac-d^2}\right)}\right)$$

Multiplying the inside of the second logarithm term by $\left(\frac{L_1}{L_1}\right)^2$ and letting

$\sqrt{4ac-d^2} = \sqrt{\delta}$,

$$t_1 = \frac{L_1^{\ 2}}{2c}\ln\left(\frac{a}{-c-d+a}\right) - \frac{L_1^{\ 2}d}{2c\sqrt{\delta}}\ln\left(\frac{\left(2c+d+\sqrt{\delta}\right)\left(d-\sqrt{\delta}\right)}{\left(2c+d-\sqrt{\delta}\right)\left(d+\sqrt{\delta}\right)}\right) \qquad \text{(J.23)}$$

Now switching to global coordinates (l,t) by substituting $y_{2f} = L-L_1$ and $t_2 = t-t_1$ into Eq. J.23.

$$
t - \frac{L_1{}^2}{2c}\ln\left(\frac{a}{-c-d+a}\right) + \frac{L_1{}^2 d}{2c\sqrt{\delta}}\ln\left(\frac{\left(2c+d+\sqrt{\delta}\right)\left(d-\sqrt{\delta}\right)}{\left(2c+d-\sqrt{\delta}\right)\left(d+\sqrt{\delta}\right)}\right) =
$$

$$
\frac{1}{2e}\ln\left(\frac{-a+c+d}{e(L-L_1)^2 + f(L-L_1) - a + c + d)}\right)
$$

$$
+\left(\frac{b}{\sqrt{-\Lambda}} - \frac{f}{2e\sqrt{-\Lambda}}\right)\ln\left(\frac{\left(2e(L-L_1) + f + \sqrt{-\Lambda}\right)\left(f - \sqrt{-\Lambda}\right)}{\left(2e(L-L_1) + f - \sqrt{-\Lambda}\right)\left(f + \sqrt{-\Lambda}\right)}\right)
$$

$$
\sqrt{\delta} = \sqrt{4ac - d^2}
$$

$$
\Lambda = -4e(a-c-d) - f^2
$$

(J.24)

If the effect of gravity is neglected, *d = f =0*, Eq. J.24 becomes,

$$
t + \frac{L_1{}^2}{2c}\ln\left(\frac{-c+a}{a}\right) = \frac{1}{2e}\ln\left(\frac{-a+c}{e(L-L_1)^2 - a + c)}\right) +
$$

$$
\left(\frac{b}{\sqrt{-\Lambda_0}}\right)\ln\left(\frac{\left(2e(L-L_1) + \sqrt{-\Lambda_0}\right)\left(-\sqrt{-\Lambda_0}\right)}{\left(2e(L-L_1) - \sqrt{-\Lambda_0}\right)\left(\sqrt{-\Lambda_0}\right)}\right) \tag{J.25}
$$

$$
\Lambda_0 = -4e(a-c)
$$

If the effect of evaporation is neglected, *c = e =0*, Eq. J.18 becomes,

$$
t_2 = \int \frac{y_{2f}}{(-f)y_{2f} + (a-d)} dy_{2f} + \int \frac{b}{(-f)y_{2f} + (a-d)} dy_{2f} \tag{J.26}
$$

Integrating,

$$
t_2 = \frac{-y_{2f}}{f} - \frac{a-d}{f}\ln\left(-fy_{2f} + a - d\right) + \frac{b}{-f}\ln\left(-fy_{2f} + a - d\right) + C \tag{J.27}
$$

Initial condition of $y_{2f} = 0$ @ $t_2 = 0$ gives C as,

$$C = \frac{a-d+b}{f}\ln\left(a-d\right)$$

Substituting back into Eq. J.27,

$$t_2 = \frac{-y_{2f}}{f} - \frac{a+d+b}{f}\ln\left(\left(-fy_{2f} + a - d\right)\left(a-d\right)\right) \tag{J.28}$$

Switching to global coordinates (l,t) by substituting $y_{2f} = L\text{-}L_1$ and $t_2 = t\text{-}t_1$ into Eq. J.28. Taking t_1 from that of the constant width channel when evaporation is neglected,

$$\begin{aligned} & t - \left[\frac{-L_1}{f} - \frac{a}{f^2}\ln\left(1 - \frac{cL_1}{a}\right)\right] = \\ & \frac{-\left(L-L_1\right)}{f} - \frac{a+d+b}{f}\ln\left(\left(-f\left(L-L_1\right) + a - d\right)\left(a-d\right)\right) \end{aligned} \tag{J.29}$$

If the effect of evaporation and gravity are neglected Eq. J.18 becomes,

$$t_2 = \int \frac{b + y_{2f}}{a} dy_{2f} \tag{J.30}$$

Integrating,

$$at_2 = by_{2f} + \frac{1}{2}y_{2f}^{\ 2} + C$$

Initial condition of $y_{2f} = 0$ @ $t_2 = 0$ gives C as,

$C = 0$

Rearranging,

$$y_{2f}{}^{2} + 2by_{2f} + -2at_2 = 0 \tag{J.31}$$

Which is,

$$y_{2f} = -b \pm \sqrt{b^2 + 2at_2}$$

Because $y_{2f} > 0$,

$$y_{2f} = -b + \sqrt{b^2 + 2at_2} \tag{J.32}$$

Switching to global coordinates (l,t) by substituting $y_{2f} = L\text{-}L_1$ and $t_2 = t\text{-}t_1$ into Eq. J.32. Taking t_1 from that of the constant width channel when both evaporation and gravity are neglected,

$$L - L_1 = -b + \sqrt{b^2 + 2a\left(t - \frac{L_1{}^2}{2a}\right)} \tag{J.33}$$

Rearranging,

$$L = L_1 - b + \sqrt{b^2 + 2at - L_1{}^2} \tag{J.34}$$

It is important to note that when $W_1 = W_2$, Eq. J.34 reduces to constant-width flow,

$$L = \sqrt{2at} \tag{J.35}$$